SHOCK AND DETONATION DYNAMICS IN NON-IDEAL GASES

A Dissertation

Submitted to the Graduate School
of the University of Notre Dame
in Partial Fulfillment of the Requirements
for the Degree of

Doctor of Philosophy

by

Katherine R. Pielemeier

Joseph M. Powers, Director

Graduate Program in Aerospace and Mechanical Engineering
Notre Dame, Indiana
September 2023

SHOCK AND DETONATION DYNAMICS IN NON-IDEAL GASES

Abstract

by

Katherine R. Pielemeier

Shock and detonation dynamics in a non-ideal van der Waals gas are studied in the presence of classical and anomalous waves. Anomalous waves are admissible in a single gas phase material when isentropes are non-convex, rendering the sound speed to have the unusual feature of decreasing with increasing temperature. The second law-satisfying anomalous waves considered include rarefaction shock waves, continuous compression fans, and composite waves. To study detonations behind anomalous waves, a foundational understanding of anomalous wave dynamics in inert flows must be established. Analysis of steady wave dynamics in an inert van der Waals gas reveals that the viscous shock solution is required to discern which among multiple second law-satisfying anomalous waves are achieved in an initial value problem. Shock tube solutions are used for verification of numerical simulations. Highly resolved viscous solutions are obtained with a simple explicit Euler time advancement scheme coupled with a second order central spatial discretization. Inviscid simulations are done with a third order Runge-Kutta method in time and a fifth order Mapped Weighted Essentially Non-Oscillatory (WENO5M) discretization. The WENO5M method is supplemented with a novel use of global Lax-Friedrichs flux-splitting in space, as local flux-splitting methods fail when changes in the sound speed are non-monotonic. New analysis is done of steady detonation dynamics in a van der Waals gas for classical and anomalous behavior. Understanding of anomalous steady wave

dynamics in inert flows is used to identify potential complications with Chapman-Jouguet and ZND analysis in and around the anomalous region. Non-convexities of Hugoniot curves in the anomalous region are found to render steady solutions predicted by CJ and ZND analysis inadmissible. Numerical predictions of stable unsteady detonations driven by an anomalous wave are presented, and the detonation dynamics are shown to be consistent with the structure of piston-driven detonations. The van der Waals model is shown to delay the transition to instability of detonations in the classical regime.

DEDICATION

This dissertation is dedicated to Owen, whose encouragement and support have made this journey possible.

CONTENTS

FIGURES

TABLES

SYMBOLS

Roman Letters

A	collision frequency factor, 1/s
a	van der Waals parameter, intermolecular forces, $\mathrm{Pa/m^6/kg^2}$
b	van der Waals parameter, excluded volume, $\mathrm{m^3/kg}$
c	frozen sound speed, m/s
$\lvert c_k \rvert$	magnitude of a Fourier mode
c_p	specific heat at constant pressure, J/kg/K
c_v	specific heat at constant volume, J/kg/K
$c_{v\infty}$	parameter for variable specific heat at constant volume, J/kg/K
D	shock speed, m/s
$\mathcal{D}$	mass diffusivity, $\mathrm{m^2/s}$
$\mathcal{E}$	relative error
e	specific internal energy, J/kg
f	overdrive factor
f	general flux function
$\hat{\mathsf{f}}$	numerical flux function
$\mathcal{G}$	dimensionless fundamental derivative
h	numerical flux function
$\dot{\mathcal{I}}$	irreversibility production rate, $\mathrm{W/m^3/K}$
k	thermal conductivity, W/m/K
L	length, m
$\mathcal{L}$	error norm

M	Mach number
M	molecular mass, kg/kmol
m	parameter for variable specific heat at constant volume
N	molecular active degrees of freedom
N	total number of discretization points
p	pressure, Pa
Pr	Prandtl number
q	heat flux, $\mathrm{W/m^2}$
q	heat release per unit mass, J/kg
R	particular gas constant, J/kg/K
$\bar{R}$	universal gas constant, J/mol/K
r, s	Riemann invariants
r	reaction rate, 1/s
s	specific entropy, J/kg/K
T	temperature, K
t	time, s
Δt	time step size, s
u	general conserved variable
u	particle velocity in the lab frame, m/s
$\hat{u}$	particle velocity in the wave frame, m/s
$\bar{u}$	particle velocity in the piston frame, m/s
v	specific volume, $\mathrm{m^3/kg}$
v_p	piston velocity, m/s
x	Cartesian coordinate, m
Δx	spatial step size, m

Greek Letters

α	thermal diffusivity, $\mathrm{m^2/s}$

α_m	flux splitting weight
α_k^*	WENO5M weight parameter
δ	value of R/c_v
ϵ	WENO parameter
Θ	activation energy, J/kg
$\bar{\Theta}$	dimensionless activation energy, $\Theta\rho_o/p_o$
γ	ratio of specific heats
λ	reaction progress
$\bar{\lambda}$	wavelength, m
ρ	density, kg/m^3
τ	viscous stress, Pa
μ	dynamic viscosity, Pa s
ν	kinematic viscosity, m^2/s
$\bar{\nu}$	frequency, MHz
ξ	piston frame spatial coordinate, m
$\omega_k^{(M)}$	WENO5M scheme weights
$\omega_k^{(JS)}$	unmodified WENO5 scheme weights
$\bar{\omega}$	ideal WENO5 weights

Subscripts

c	critical value
CJ	Chapman-Jouguet value
$grid$	value related to a grid size
max	maximum value
min	minimum value
o	reference value

ACKNOWLEDGMENTS

I would like to thank my adviser, Dr. Joseph M. Powers for his valuable support, insight, and expertise. I am grateful for his guidance, and for allowing me the space in which to grow as a researcher and as a writer.

I would also like to acknowledge, and thank, Mr. Alexander M. Davies for his contributions to this work, as his undergraduate research work on viscous anomalous waves plays a key part in this dissertation. It was a pleasure to work with him, and I am grateful for the opportunity to watch and aid in his growth as a person and a researcher. I wish him the best of luck in his own graduate studies and future career.

I am thankful to Dr. Tariq D. Aslam for introducing me to the ideas that led to this work. I would also like to acknowledge Los Alamos National Laboratory for its funding of this work and my time at Notre Dame.

Finally, I thank my parents for their support, guidance, and encouragement in every endeavor, and I thank my fianceé Owen for his never ending support.

CHAPTER 1

INTRODUCTION

This work will explore the relationship between shock and detonation dynamics in non-ideal gases. Fundamental detonation theories are built upon a foundational understanding of shock waves. Non-ideal gas equations of state induce physics that present challenges for mathematical studies of fluid flows and allow for unusual wave structures that are inadmissible in the ideal gas limit. Such anomalies include discontinuous rarefaction shocks, continuous homeoentropic compressions, and composite shock waves. These anomalous waves are in contrast to what will here be referred to as classical waves, including discontinuous compression shocks and continuous homeoentropic rarefaction fans. It is important for foundational thermodynamics to work in harmony with analyitical and numerical predictions when unusual behaviors are encountered in order to confidently determine relevant physical behavior. This is especially important for detonations behind such unusual shocks, for which foundational understandings are challenged by complicated wave structures.

1.1 Motivation

As described by Davis [38], the first major steps in detonation theory were made in the study of shock waves. Early studies of explosive gases, such as the work of Chapman [20] and Jouguet [72] determined that a detonation propagates as a wave, much like a shock wave. Chapman proposed that detonation waves could be considered as self-sustaining shock waves with the chemical reaction supplying the energy to drive the shock wave. Chapman's predictions of detonation velocities using

equations for a shock wave with the effects of heat release showed good agreement with experimental observations. Contemporaneously, Jouguet showed that the minimum detonation velocity corresponds to the velocity of a sound wave in the detonation products of a shocked explosive. This theory gave a physical explanation for why an unsupported detonation wave propagates at the minimum detonation velocity. Chapman-Jouguet (CJ) theory remains the foundation on which much of detonation theory is constructed. Although CJ theory lacks details of the structure of detonation waves, engineering applications still find use for its predictions of a detonation's final state. From this state, expansion of detonation products may be calculated, necessary for applications for which the energy transfer associated with this process is used to do work.

The first researchers to address the underlying structure of a detonation were Zel'dovich [128], von Neumann [122], and Döring [40]. They independently extended the CJ theory, maintaining that across the initial shock wave, no chemical reaction took place. Between the shock and the equilibrium state, they asserted that the reaction zone covered a continuous sequence of chemical states, each with its own pressure and particle velocity. Their work formed the Zel'dovich-von Neumann-Döring (ZND) model for detonations. The ZND model enables description of how a detonation proceeds as well as the structure of the reaction zone.

Both the CJ and ZND theories are based in the study of shock waves, and rely upon analysis of the Rankine-Hugoniot shock jump conditions, Rayleigh lines, and Hugoniot curves. Such shock wave analysis must include the equation of state for a gas, and often relies on the ideal gas model. The ideal gas model is qualitatively similar for different gases, admitting classical waves such as compression shocks and rarefaction fans. Contemporary to the development to of the ZND model, the possibility of non-classical behaviors associated with non-ideal equations of state was considered, first by Bethe [12] and Zel'dovich [127], and later by Thompson [119].

They were interested in what happened when isentropes behaved in such a way that classical compression shocks and rarefaction fans were no longer admissible. It was concluded that the waves that would form were anomalous compression fans and rarefaction shocks, wave types considered inadmissible or unstable in classical gas dynamics. They theorized that for some materials, a region of state space exists in the gas phase near the critical point where anomalous waves would form, now called the Bethe-Zel'dovich-Thompson (BZT) region. In this region, the equation of state does not behave as expected in classical gas dynamics, affecting the Rankine-Hugoniot jump conditions and Rayleigh line and Hugoniot curve analysis. For a reactive system, this anomalous behavior must necessarily affect the fundamental detonation theories of CJ and ZND.

Modern detonation research continues to address the need for greater understanding of detonation dynamics. Bdzil and Stewart [7] summarized advances in modeling and constitutive data for numerical and analytical studies of condensed-phase explosive detonation waves. They identified four major challenges in advancing the study of detonation dynamics: improving equation of state and rate law pairs in engineering models, advancing high-resolution hydrodynamic codes, understanding better hydrodynamic stability characteristics, and understanding basic meso-scale structures. Short and Quirk [110] summarized the need for understanding complex wave interactions in detonation-confiner systems, using oblique shock wave polar theory to aid in analysis of these interactions, noting in some cases that the interaction suggested by the polar analysis was inconsistent with observed flow patterns. They identified a need for improvements in various aspects of the understanding and modeling of detonation-confiner interactions, including in fluid mechanics, detonation propagation, and continuum modeling. Raman, Prakash, and Gamba [102] addressed the need for fundamental understanding of non-idealities in rotating detonation engines, including secondary combustion and secondary waves. Such non-idealities influence

the flow structure, affecting efficiency and operability. Although these works are concerned with larger engineering applications, they all return to the need for fundamental understanding of shock and detonation dynamics.

1.2 Literature Review

1.2.1 Convexity

A short review of convexity is presented, as it is the cornerstone for the admission of anomalous waves in a single-phase gas. Defined on an interval $[v_1, v_2]$, a real valued function is convex if the line segment connecting any two points on the curve lies entirely above the curve between the two points. This is equivalent to the epigraph of the function being a convex set, with the epigraph defined as the set of points on or above the graph of a function. If this condition is not met, the epigraph is not a convex set, and the function is non-convex. Example isentropes are shown in Fig. 1.1. The shaded areas represent the epigraphs; the epigraph in Fig. 1.1(a) forms a convex set, and in Fig. 1.1(b) a non-convex set. The convexity of a function can also be determined by the second derivative of the function, for which positive and negative values correspond to convex and non-convex functions, respectively; this will be the primary method of describing convexity in this work. If the second derivative of the function everywhere on the domain is positive semi-definite, then the function is convex. If the second derivative is everywhere negative on the domain, the function is non-convex. If the second derivative is both positive and negative within the domain, the function is referred to as having mixed convexity on the domain.

1.2.2 Anomalous Waves

One of the first studies on the admissibility of anomalous waves was done by Bethe [12]. In a detailed analysis of the second derivative of pressure p with respect

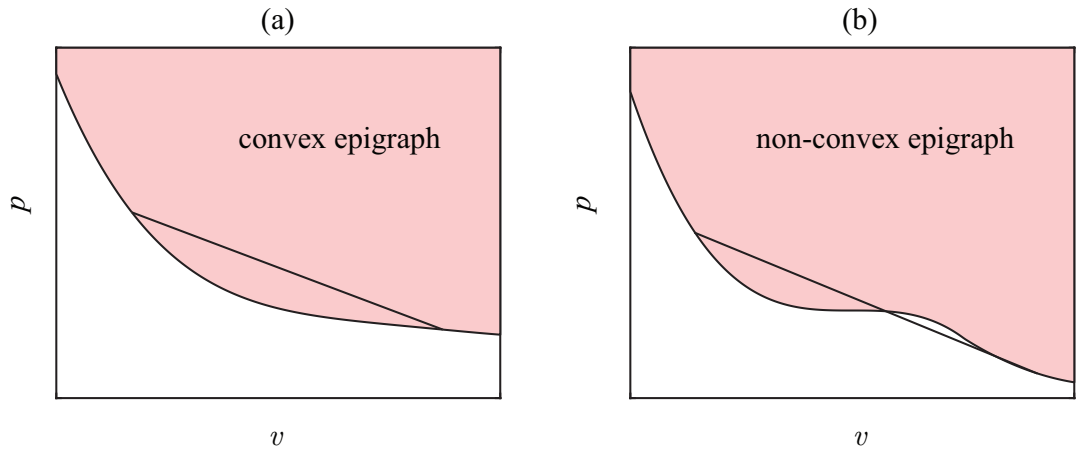

Figure 1.1. Example isentropes in the pressure - specific volume plane. The isentrope in (a) is convex over the domain, as its epigraph is a convex set, and the second derivative is positive at all points. The isentrope in (b) has an epigraph that does not form a convex set, and the function has points for which the second derivative is negative.

to specific volume v at constant entropy s, potential causes of $\partial^2 p/\partial v^2|_s < 0$ were sought. His main focus was on the case of anomalous behavior caused by phase transitions, ascertaining at the time that single-phase anomalous behavior was unlikely, or impossible, in a real fluid. Nonetheless, Bethe determined for the van der Waals equation of state that in order for $\partial^2 p/\partial v^2|_s < 0$ to occur in the gas phase, the relation $c_v/R > 17.5$ (or $\delta < 0.06$ where $\delta \equiv R/c_v$) must be satisfied, where c_v is the specific heat at constant volume and R is the gas constant of a particular molecule. Bethe argued that this value was likely higher than any real material would exhibit in the region of interest, a conclusion that was echoed by Kahl and Mylin [73]. Concurrently, Zel'dovich [127] theorized that there should, given a high enough value of c_v, be a region of state space where in a single-phase gas rarefactions propagate as discontinuous shocks and compressions propagate as smooth fans. He also connected the sign of $\partial^2 p/\partial v^2|_s$ to the existence of such non-classical waves.

Thompson [119] formally introduced a dimensionless formulation of $\partial^2 p/\partial v^2|_s$ for

a general material, called the fundamental derivative of gas dynamics and represented by $\mathcal{G}$. The fundamental derivative is an indicator of the convexity of isentropes in the $p-v$ plane. Positive values of the fundamental derivative indicate convex isentropes, and negative values indicate non-convex isentropes. Lambrakis and Thompson [79] investigated a number of real fluid classes, namely hydrocarbons and fluorocarbons, that were determined to meet the criteria to admit anomalous behavior in the gas phase region. Using tabular data and thermodynamic models, they found limited regions of state space where $\mathcal{G}$ is negative near the saturated vapor curve in the vicinity of the critical point. The identified region was roughly equivalent to the predictions of Zel'dovich and Raizer [129]. Further exploration of fluids with potential to admit anomalous waves in the gas phase has been done with hydrocarbons and fluorocarbons [31, 50, 51], and later studies included siloxanes [26, 27, 28]. Table 1.1 shows properties of several fluids, including the value of δ near the critical point.

While Bethe's condition for non-convexity in a van der Waals fluid ($\delta < 0.06$) is a useful tool to identify BZT fluids, this thermodynamic approach is connected to a molecular interpretation by Colonna and Guardone [25] and Harinck, et al. [63]. These studies indicated that the minimum value of $\mathcal{G}$ for a gas varies inversely with its molecular complexity, defined as the number of active degrees of freedom and given by the symbol N. This behavior holds for ideal gases, but only when non-idealities are accounted for in the equation of state is $\mathcal{G} < 0$ observed. The value of δ is related to the molecular complexity by using $c_v = N\bar{R}/(2\mathsf{M})$, where $\bar{R}$ is the universal gas constant and M is the molecular mas, to write δ as

$$\delta = \frac{2}{\mathsf{N}}. \tag{1.1}$$

A monatomic gas has three translational degrees of freedom, so $\mathsf{N} = 3$ and $\delta = 2/3 = 0.667$, and a diatomic gas has three translational and two rotational degrees of

TABLE 1.1

PHYSICAL PARAMETERS OF VARIOUS MATERIALS

Fluid	P_c (kPa)	T_c (K)	M (g/mol)	N	δ
H_2	1300	33.2	2.02	4.6	0.4329
CH_4	4610	190.6	16.04	6.0	0.3309
O_2	5040	154.6	32.00	4.9	0.4121
CO_2	7380	304.2	44.01	7.0	0.2855
Toluene	3990	591.8	92.14	44.3	0.0452
Octane	2430	568.8	114.2	73.3	0.0273
Dodecane	1770	658.2	170.34	121.6	0.0164
D4	1330	586.5	296.62	127.6	0.0157
PP5	1710	565.2	462.00	123.5	0.0156
PP10	1580	632.2	574.00	156.2	0.0128

freedom, so $\mathsf{N} = 5$ and $\delta = 2/5 = 0.40$; both values are much larger than the $\delta < 0.06$ condition for non-convex isentropes in a van der Waals gas. More complex molecules have more degrees of freedom; it is noted that N may have non-integer values due to the partial activation of vibrational degrees of freedom at a given temperature. Thus, it is not necessarily molecular mass M that δ depends on, but the number of active degrees of freedom of the molecules. It can be seen in Table 1.1 that within the same class molecular mass and complexity are directly related. Lighter molecules may be more complex if composed of more atoms. Take methane (CH_4) and molecular oxygen (O_2), which have molecular masses of $\mathsf{M} = 16.04$ g/mol and $\mathsf{M} = 32.00$ g/mol, respectively. Methane has more atoms, and its molecular degrees of freedom N is larger than oxygen. The same is observed with D_4 ($C_8H_{24}O_4Si_4$) and PP10

($C_{13}F_{22}$), both fluids from two different families of materials considered to exhibit BZT effects. D_4 is a siloxane, and PP10 is a fluorocarbon. Although the molecular mass of PP10 is nearly twice that of D_4, their molecular complexity is nearly the same, and thus their δ values are very close at 0.0128 and 0.0157, respectively.

With the theoretical existence of the BZT region established, and some real fluids that fulfill the requirements for anomalous behavior in the gas phase determined, many studies have sought to better understand the anomalous wave structures possible in such fluids. Cramer and Sen [35] investigated shock formation in an inviscid van der Waals gas from triangular and periodic wave pulses. They modeled an arbitrary fluid with large specific heat, demonstrating the formation of composite waves, with a new shock forming each time the pulse crossed $\mathcal{G} = 0$. Cramer and Crickenberger [34] studied the structure of expansion shocks. They confirmed that where $\mathcal{G}$ changes sign, the Mach number has a maximum or minimum, no longer increasing monotonically. Cramer [32] presented detailed descriptions of the conditions under which shock splitting occurs. When shock adiabats cross into and out of $\mathcal{G} < 0$ regions, they exhibit mixed convexity, and as a result Rayleigh lines may intersect at more than two points. Additionally, the Rankine-Hugoniot jump conditions have more than two solutions, but only between neighboring roots are solutions valid. Cramer concluded that split shock structures evolve dynamically from inadmissible initial configurations, analogous to the disintegration of expansion shocks to form centered expansion fans in perfect gases.

More recently, Guardone, et al. [61] and Zamfiresue, et al. [126] investigated the maximum intensity and admissibility region for rarefaction shock waves. It was determined that the region where rarefaction shocks are admissible is slightly larger than the BZT region, as they may occur between two states where $\mathcal{G} > 0$ if the shock adiabat enters the $\mathcal{G} < 0$ region. The size and shape of this region for a van der Waals equation of state is influenced by the molecular complexity of the material,

but the maximum pressure difference in these rarefaction shocks is capped around 1/3 of the critical pressure. Kluwick and Meyer [75] investigated shock/boundary layer interactions in transonic flows for narrow channels with BZT fluids. They determined that for a rarefaction shock, the boundary layer flow remained attached to the wall of the channel, potentially avoiding a source of losses in technical applications. Both of these studies are of significant interest for industrial applications where a wider operating range including BZT effects is advantageous.

The primary engineering application with interest in BZT fluids is organic Rankine cycles (ORCs), Rankine cycles which use organic high molecular mass fluids. ORCs are used for electricity generation in low-power applications, often relying upon sources such as geothermal, solar, and industrial waste heat. ORCs typically utilize a single expansion stage operating in the transonic/supersonic regime, where a major loss mechanism is the generation of shock waves [29]. BZT fluids are often high molecular mass, and the anomalous behavior of these materials may provide advantages in efficiency [19]. Multiple authors [22, 23, 29, 36] have investigated the effects of the BZT region on the aerodynamic performance of turbine blades, including lift, drag, and lift-to-drag ratio, as a preliminary step in the design of a Rankine cycle in a BZT fluid. Studies have focused on variations in turbine blade shape and location of the flow relative to the BZT region, including flows with mixed convexity. Adjustments to these parameters have been attempted in order to balance losses caused by wave drag and shock/boundary layer interactions with achieving the larger temperature jumps needed for adequate power output from the cycle. Because nonconvexity mainly influences inviscid flow behavior, analysis is often restricted to the Euler equations with the van der Waals equation of state to capture the BZT effects. Aldo and Argrow [1] studied potential complications of anomalous behavior of dense gases in supersonic nozzle design. Cinnella and Congedo's [23] results suggested that the flow field need not be entirely within the BZT region in order to benefit from

the effects of this region, increasing turbine performance by reducing losses caused by drag and shock/boundary-layer interactions.

Some work has been done on the theory and construction of an experimental shock tube for dense gas flows with the goal of producing experimental evidence of anomalous waves [48, 49, 50, 51]. A number of problems prevented the observation of a rarefaction shock, including imperfect bursting of the diaphragm in the shock tube and thermal decomposition of the working fluid, PP10. At this time the author is unaware of any experimental evidence of anomalous waves. Early attempts by Borisof, et al. [15] did report experimental evidence of expansion shocks in Freon-13. However, other authors later determined that this was likely to be a result of the affects of the critical point and phase transitions [25, 35, 51, 61].

Studies have been done exploring the application of a variety of numerical methods to flows with anomalous behavior. Rider and Bates [104] introduced a Godunov method suited for modeling anomalous behavior. By making adjustments to a previous Godunov scheme, they ensured that the method would produce the expected anomalous behavior when the fundamental derivative became negative. This method was tested on both a fully non-convex as well as a mixed convexity shock tube, producing the expected results in these cases. Bates and Montgomery [6] utilized a flux-corrected transport method in order to predict potential anomalous behavior in inertial confinement fusion schemes. Numerous studies have employed total variation diminishing (TVD) schemes in the study of anomalous waves. Argrow [4] used a TVD-MacCormack predictor-corrector scheme with reflective end wall boundary conditions to calculate shock tube solutions in classical and anomalous regimes. Brown and Argrow [17, 18] modeled two-dimensional dense gas flows in shock tubes and over obstacles with a predictor-corrector TVD scheme. These models predicted the total and partial disintegration of compression shocks. They used the van der Waals equation of state with constant isochoric specific heat, an assumption which is ad-

vantageous for modeling qualitative gas structures.

Analytical solution methods have been developed for shock waves with a wide array of non-ideal equations of state. Sirignano [113] presented a comprehensive comparison of shock solutions with the ideal gas and Soave-Redlich-Kwong equations of state. The work addresses many of the ways in which shock solutions are affected by accounting for real gas effects. Wand and Hickey [123] similarly compared shock solutions with the ideal gas, Redlich-Kwong, Soave-Redlich-Kwong, and Peng-Robinson equations of state. They proposed a simplification of the Rankine-Hugoniot jump conditions that results in improved behavior of the Jacobian and Hessian expressions, which are then utilized in their solution procedure. They addressed rarefaction waves by implementing a domain mapping to derive the flow variables. Quartapelle, et al. [100] provided a general solution of the Riemann problem, with specific solutions presented for a van der Waals and Martin-Hou equations of state. The van der Waals equation was presented with and without the assumption of constant specific heats, both at constant pressure and constant specific volume. The work compared the exact solutions with numerical simulations for the Riemann problem in the classical gas dynamics regime.

1.2.3 Detonation

Detonations in gaseous mixtures were first recognized by Berthelot and Vielle [10, 11] and Mallard and Le Chatelier [82], who studied flame propagation. Early studies of detonations were done to understand the minimum conditions under which they occur. Chapman and Wheeler's early work [21] on detonation formation measured the speed of flame propagation in a methane-air mixture. Oppenheim, et al. [90] suggested a theory for a subsonic flame leading to a detonation, and first reported such a transition [91], where a laminar flame coalesced to form a shock wave, which perturbed the trailing laminar flame, leading to a detonation. Independent

work by Chapman [20] and Jouguet [72] predicted the minimum velocity of a detonation with the inviscid steady one-dimensional jump conditions. At the CJ speed, a unique solution exists for which the wave is self-propagating, supported only by the energy supplied by the reaction. It is possible for the detonation speed to be higher when the wave is supported by additional energy from a piston. Such piston supported detonations are called overdriven, and the overdrive factor is defined as $f = (D/D_{CJ})^2$, where D is the wave speed of the leading shock and D_{CJ} the CJ speed.

In the ZND model, the dominating physical mechanisms driving the detonation are piston-driven waves and reaction; typically non-equilibrium effects such as viscosity, radiation, and heat conduction are neglected. The governing equations reduce to the one-dimensional reactive Euler equations. Traditionally the thermodynamic model is the calorically perfect ideal gas equation of state. These assumptions result in solutions that present the basic structure of the reaction zone in one dimension. Discontinuous jumps in density, pressure, particle velocity, and temperature are induced by the shock, while the reaction's progress does not change across the shock discontinuity. The reaction initiates suddenly at the shock, and after an induction time, the reaction rate dramatically increases, and a large thermal energy release occurs. At the same time, kinetic energy, pressure, and density decrease. For detonations traveling at the CJ speed, the reaction ends at a sonic point, and the particle velocity in the wave frame is equal to the local sound speed.

The ZND model is a strictly steady-state approximation. Experimental evidence shows that many detonations are in fact unstable, with evidence of instability present in soot tracks lining the interior of a tube in which a detonation has occurred [77]. Detonation stability has been studied utilizing linear stability analysis as well as numerical simulations of full non-linear systems. Several types of instabilities of detonation waves have been observed, and the type of instability is determined by the

way the detonation is initiated, the geometry of the configuration, and the intrinsic thermodynamic properties of the reactive mixture [62]. The type of instability this work will be concerned with is longitudinal instabilities, which develop in small diameter tubes which hinder multidimensional instabilities. Also called galloping instabilities, they occur in the direction that the detonation wave propagates. The wave front accelerates and decelerates in a periodic or irregular pattern [116]. Additionally, experimental evidence was observed by Lehr [78] of longitudinal oscillations in shock-induced combustion flow around spherical projectiles.

Fickett and Davis [52] presented a comprehensive review of linear analytical stability results, drawing heavily from the work of Erpenbeck [46, 47]. They presented stability analysis when parameters were varied, including the activation energy in the chemical reaction model, the heat release of the chemical reaction, the wave number of the transverse disturbance, and the overdrive factor of the detonation. One of the general trends established that at low overdrive values and finite heat release, increasing the activation energy decreased the threshold for transition to instability; sufficiently high overdrive values resulted in stability, and for zero activation energy, all values of heat release and overdrive resulted in stability. Lee and Stewart [76], with more modern techniques, supported the results of previous studies and expanded upon them by extending the range of the parameters (activation energy, heat release, wave number) studied.

Numerical studies of ZND detonations are necessary to determine the nonlinear behavior of the detonation, and have been used to verify the linear stability analyses. Fickett and Wood [53] found solutions of pulsating detonations with the method of characteristics. Unstable detonations were found to oscillate about the steady solution of the linear analysis. Bourlioux, Majda, and Roytburd [13] compared unstable detonation simulations to the linear stability results of [76]. They demonstrated through asymptotic analysis that their numerical method predicted the correct un-

stable behavior. Sharpe and Falle [109] studied requirements on grid resolution to achieve converged solutions, as unstable detonations introduce several length scales to a numerical simulation .

The simple inviscid model with one-step kinetics in ideal gases is well understood. The following review touches on some aspects of this. Erpenbeck [46, 47] studied stability of the ZND profile for one-step irreversible kinetics. Kasimov and Stewart [74] used first-order shock fitting to analyze the linear stability of the ZND profile. Borlioux, et al. [13] studied the manner in which instabilities developed. This work was continued by He and Lee [64], who used the Euler equations to identify activation energies at which transitions to instability occur. Bifurcation points based on overdrive factor were studied by Daimon and Matsuo [37]. Ng, et al. [88] presented a bifurcation diagram demonstrating increasing complexity of oscillations with increasing activation energy. A more detailed bifurcation diagram was presented by Henrick, et al. [66]. A true fifth order shock fitting method was used, and instabilities were represented by oscillations in the shock speed.

Predictions of detonation stability with numerical simulations must take into account complex interactions of chemistry and fluid mechanics, making it a challenging endeavor. Many length scales must be accounted for, and can span from devices on the order of meters to chemical reaction scales estimated on the order of the mean free path [99]. Assumptions are often made to reduce computational requirements, including neglecting diffusion, reduced kinetic models, and limiting to one dimension. The simplest kinetic model, composed of a single reaction, is useful in exploring the relation between chemical kinetics and transport phenomenon. One-dimensional models limit the types of instabilities that are observed, but provide valuable insights into detonation structures and the evolution of instabilities. This also allows for high resolution simulations with moderate computational costs, as multiple dimensions can easily become computationally prohibitive [101, 108, 124].

Although the simplest model is useful for tractable analysis of detonation dynamics, extending the model to account for additional non-equilibrium effects is also important so as to understand when an assumption may preclude important physical effects. Early work studying one-dimensional detonations with one-step kinetics focused on finding a steady diffusive detonation. Friedrichs [54] included viscous and thermal dissipation while treating the reaction as a discontinuity. ZND theory with one-step kinetics was expanded to include diffusion by Hirschfelder and Curtiss [68]. They found that they had to restrict the Lewis and Prandtl numbers, as well as including viscous and thermal dissipation in the shock zone. A steady diffusive strong detonation was shown to exist when limited to weak diffusion by Gasser and Szmolyan [55]. In the limit of weak diffusion, Texier and Zumbrun [118] demonstrated a bifurcation point in a one-step detonation as the overdrive was lowered. More recently, work has been done by Romick, et al. [105, 106] describing the dynamics of one-dimensional piston-driven detonations with mass, momentum, and energy diffusion. Using numerical simulations, stable and unstable detonations were predicted and compared with the inviscid limit, and it was found that the inclusion of physical diffusion delays the transition to instability. Additionally, significant reduction in the magnitude of instabilities was predicted in some cases.

As discussed previously, CJ, ZND, and unstable detonation analysis is traditionally done with the ideal gas equation of state. However, non-ideal gas effects can influence the predicted behavior of gas flows in a number of ways. Although the ideal gas assumption is often a valid and practical choice, factors such as high pressure or density may render it an inappropriate choice. Schmitt and Butler [107] performed a comprehensive investigation of predicted detonation properties at high initial pressures, computing results of equilibrium CJ solutions with ideal gas, van der Waals, Redlich-Kwong, Soave, and Peng-Robinson equations of state for various materials, including hydrogen, methane, ethylene, ethane, and propane. By comparing these

predictions with experimental results, they concluded that the ideal gas equation of state was inadequate at pressures over 10 bars, incorrectly predicting the thermodynamic states in this regime. The other equations of state provided a more accurate prediction of the corresponding thermodynamic states, while suffering minimal effects related to uncertainty in the respective equation of state constants. Dumazer, et al. [42] presented a study of steady wave fronts in a van der Waals fluid with a Fisher-Kolmogorov-Petrovsky-Piskunov (F-KPP) type exothermic, autocatalytic reaction. Propagating waves initiated by nonuniform reactant concentrations were considered. They found that the stationary wave front speeds were decreased at low densities and increased at high densities.

1.3 Novelty

The novel contributions of the work in this dissertation are summarized here. In order to study detonations associated with anomalous waves, a foundational understanding of anomalous wave dynamics in inert flows must be established. Analysis of steady wave dynamics in an inert van der Waals gas reveals that the viscous shock solution is required to discern which among multiple second law-satisfying anomalous waves are achieved in an initial value problem. Investigation of the second law of thermodynamics and irreversibility generation for viscous shocks in non-ideal gases shows that the entropy and irreversibility production rate across anomalous waves is consistent with expected behavior. An existing solution for homeoentropic waves in an inert van der Waals gas is shown to apply to anomalous compression fans. Numerical methods for shock tubes with inert inviscid flows containing anomalous waves are verified. The WENO5M method is shown to require implementation of a global flux splitting approach in order to obtain numerically stable solutions for anomalous waves.

New analysis is done of steady detonation dynamics in an inviscid van der Waals

gas for classical and anomalous behavior. Understanding of anomalous steady wave dynamics in inert flows is used to identify potential complications with CJ and ZND analysis in and around the anomalous region. Non-convexities of Hugoniot curves in the anomalous region are found to render steady solutions predicted by CJ and ZND analysis inadmissible. Stable unsteady detonations driven by an anomalous wave are presented. It is found that when an anomalous composite compression wave is driven into a reactive medium, the resulting detonation structure behind the trailing discontinuous shock is qualitatively consistent with traditional detonation dynamics. The leading wave remains a composite compression wave with a continuous compression fan immediately followed by a compression shock; the fan is not overtaken by the detonation. Unsteady detonation dynamics in a van der Waals gas are verified with analysis of Discrete Fourier Transformations for varying grid sizes. Analysis is done on the van der Waals model's effect on stability limits and unstable unsteady detonations in the classical regime. The intermolecular forces captured in the van der Waals model are found to delay the transition to instability with increasing activation energy.

1.4 Outline of the Dissertation

The plan of this dissertation is as follows: In Chapter 2 the mathematical model is presented; it encompasses inviscid and viscous inert models and the inviscid reactive model. Useful forms of the governing equations are included, and the inviscid reactive system is transformed to a piston-attached coordinate system. The primary thermodynamic model used is the van der Waals equation of state. Chapter 3 presents the numerical methods used. Various useful algebraic numerical methods are discussed. For the viscous case, a first-order Euler in time and second-order central difference scheme in space is used. The inviscid case is performed with a third-order Runge-Kutta in time and a fifth order Weighted Essentially Non-Oscillatory method

with modified weights (WENO5M), originally presented by Henrick, et al. [65]. The choice of flux splitting scheme required for WENO5M is discussed in the context of anomalous waves.

Steady wave dynamics in inert gases are analyzed in Chapter 4. The second law of thermodynamics is discussed, along with the irreverisibility production rate for the viscous case. The fundamental derivative of gas dynamics is introduced as an important quantity in the study of anomalous waves. Rayleigh line and Hugoniot curve analysis is presented in classical and anomalous regions, demonstrating non-convex regions of the Hugoniot curve in the anomalous region. Rankine-Hugoniot jump analysis reveals the need to account for the viscous shock solutions to discern which among multiple second law-satisfying anomalous waves are achieved in an initial value problem. Chapter 5 considers unsteady inert wave dynamics. First, exact solutions of inviscid continuous waves are presented for classical and anomalous waves. These solutions are combined with shock jump analysis to calculate analytical solutions of classical and anomalous shock tubes with inviscid van der Waals gases, which are compared with numerical simulations of shock tubes with viscous van der Waals gases. This chapter concludes with verification of the numerical methods.

Chapter 6 changes focus to the inviscid reactive system. In this chapter, the ideal gas and van der Waals models are compared in the classical regime, and the effect of anomalous behavior is explored with the van der Waals model. Rayleigh line and Hugoniot curve analysis is repeated for the reactive system. CJ solutions are discussed, and potential complications due to the nature of the anomalous region are explored. Without accounting for anomalous wave behavior, CJ analysis may predict solutions that are inadmissible. The same is true for predictions of the steady reaction zone with ZND analysis, which is intended to solve for the structure of the reaction zone behind a discontinuous compression shock. In the anomalous region it is possible for there to be no admissible compression shock, but instead an anomalous

composite shock wave consisting of a continuous compression fan followed by a shock discontinuity.

Unsteady detonation dynamics are explored in Chapter 7. First, numerical simulations of stable unsteady detonations are presented with initial conditions in the anomalous region. The first case presented is a shock of sufficient strength to drive the flow out of the anomalous region entirely to achieve a classical compression shock. The shock in the second case is an anomalous composite compression; the inert shock structure is compared with the structure in the reactive system. Next, unstable detonations in ideal and van der Waals gases are compared. Unsteady detonation dynamics are verified with analysis of DFTs, and the length scale requirements introduced by unsteady dynamics are discussed. Finally, the effect of the van der Waals model on the stability limit in the classical region is compared relative to the ideal gas. The overall work is summarized in Chapter 8, and suggestions for continuation of this work are given.

CHAPTER 2

MATHEMATICAL MODEL

In this chapter the mathematical model is presented. In the continuum limit, gaseous, compressible, viscous, reactive flows can be described by a system of partial differential equations (PDEs). Constitutive relations must be specified for the caloric and thermal equations of state, as well as the viscous stress and diffusive heat transfer. The van der Waals model has been chosen for this work, and is described here. The reaction rate model is chosen as simple one-step Arrhenius kinetics. Initial and boundary conditions must also be specified, and are described for two model problems, the Sod shock tube and a piston-driven wave.

2.1 System of Equations

2.1.1 Reactive Navier-Stokes

The governing equations are the one-dimensional reactive Navier-Stokes equation for a van der Waals gas with one-step irreversible Arrhenius kinetics are:

$$\frac{\partial \rho}{\partial t} + \frac{\partial}{\partial x}(\rho u) = 0, \tag{2.1}$$

$$\frac{\partial}{\partial t}(\rho u) + \frac{\partial}{\partial x}(\rho u^2 + p - \tau) = 0, \tag{2.2}$$

$$\frac{\partial}{\partial t}\left(\rho\left(e + \frac{1}{2}u^2\right)\right) + \frac{\partial}{\partial x}\left(\rho u\left(e + \frac{1}{2}u^2 + \frac{p}{\rho}\right) + \mathsf{q} - \tau u\right) = 0, \tag{2.3}$$

$$\frac{\partial}{\partial t}(\rho\lambda) + \frac{\partial}{\partial x}(\rho u\lambda) + \frac{\partial j}{\partial x} = \rho r, \tag{2.4}$$

$$
\begin{aligned}
r(T,\lambda) &= A(1-\lambda)\exp\left(-\frac{\Theta}{RT}\right), && (2.5)\\
p(T,v) &= \frac{RT}{v-b}-\frac{a}{v^2}, && (2.6)\\
e(T,v,\lambda) &= c_v T-\frac{a}{v}-\lambda q, && (2.7)\\
\tau &= \frac{4}{3}\mu\frac{\partial u}{\partial x}, && (2.8)\\
\mathsf{q} &= -k\frac{\partial T}{\partial x}+\rho\mathcal{D}q\frac{\partial \lambda}{\partial x}, && (2.9)\\
j &= -\rho\mathcal{D}\frac{\partial \lambda}{\partial x} && (2.10)
\end{aligned}
$$

where the independent variables are the Cartesian coordinate x and time t. The dependent variables are density ρ, particle velocity in the lab frame u, pressure p, specific internal energy e, reaction progress λ, reaction rate r, temperature T, viscous stress τ, and diffusive heat flux q. Constant parameters are collision frequency factor A, activation energy Θ, gas constant for a particular gas R, heat release per unit mass q, van der Waals constants a and b, specific heat at constant volume c_v, dynamic viscosity μ and thermal conductivity k, and mass diffusivity $\mathcal{D}$. Equations (2.1-2.3) describe the conservation of mass, momentum, and energy. Equation (2.4) describes the evolution of the reaction progress. Equation (2.5) is the reaction rate model for one-step irreversible Arrhenius kinetics [5]. Equations (2.6) and (2.7) are the constitutive relations, the thermal and caloric equations of state for the van der Waals model; additional details on the van der Waals model are given in the next section. Equations (2.8) and (2.9) define the viscous stress and heat flux for a Newtonian fluid satisfying Stokes' assumption and Fourier's law. Equation 2.10 is Fick's law for mass diffusion.

The reaction rate model that has been chosen is one-step irreversible kinetics. For this model, a single reaction occurs where

$$
\mathcal{A}\rightarrow\mathcal{B}, \qquad (2.11)
$$

and it is assumed that both $\mathcal{A}$ and $\mathcal{B}$ have identical properties, including molecular mass, specific heats, gas constant, and van der Waals parameters. The reaction progress variable λ ranges from 0 to 1, with $\lambda = 0$ indicates unreacted and $\lambda = 1$ fully reacted. This simple kinetics model has been chosen to enable qualitative analysis of reactive flows in non-ideal gases.

Initial and boundary conditions are required for the two model problems that will be used throughout this work: shock tubes and piston-driven shocks. The shock tube requires a no-penetration boundary condition at both ends, and a particle velocity of $u = 0$ is enforced at the end points. The initial conditions are those of the Riemann problem; a contact discontinuity separates distinct constant states on the right and left of the shock tube, as shown in Fig. 2.1(a). The initial velocity is zero everywhere. In the piston-driven system, particle velocity at the piston face must be equal to the velocity of the piston v_p . For our purposes, the opposite end of the domain is treated as infinite, and only limits the system in so far as the time must not be allowed to run long enough for the wave to reach the end of the domain. Initial conditions are an ambient state at rest everywhere, as shown in Fig. 2.1(b).

2.1.2 van der Waals Equation of State

Many non-ideal equations of state exist for which anomalous behavior is admissible in the gas phase, and while a variety are often used [60], a common choice is the van der Waals equation of state. The van der Waals model is likewise utilized here, as it admits anomalous behavior as well as is useful in illustrating the challenges of non-ideal state equations. The van der Waals correction is often most important near the vapor dome. Much of this work will utilize states near the vapor dome, but will not enter the vapor dome and is confined to the gas phase. The thermal and caloric equations of state are given in Eqs. 2.6 and 2.7, respectively. The van der Waals equation of state is a correction to the ideal gas model with two parameters a and b

a) initial conditions: shock tube

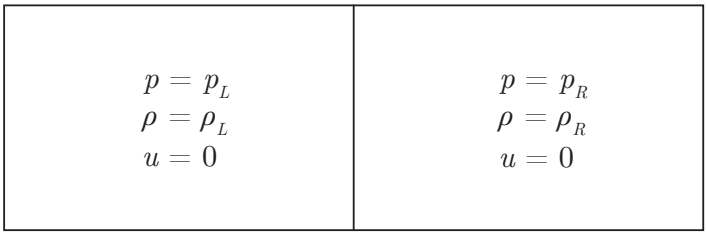

b) initial conditions: piston

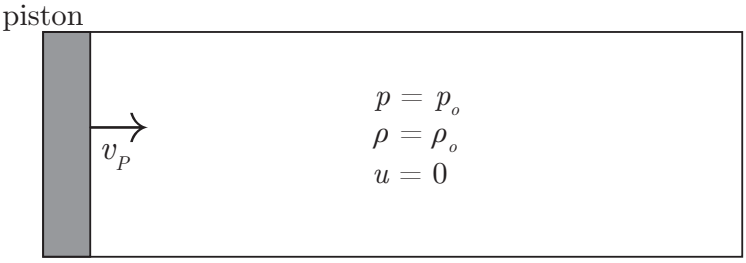

Figure 2.1. Initial conditions for two model problems. (a) The shock tube, with initial velocity of zero everywhere and two distinct constant states on the left and right separated by a contact discontinuity. (b) The piston-driven shock, with initial velocity of zero everywhere and a constant initial ambient state.

defined by

$$a = \frac{27}{64}\frac{R^2 T_c^2}{P_c}, \tag{2.12}$$

and

$$b = \frac{1}{8}\frac{RT_c}{P_c}. \tag{2.13}$$

These parameters are based on the fluid properties, including the critical temperature and pressure T_c and P_c. The critical density is then predicted by the van der Waals model. Setting both a and b to zero reduces the van der Waals model to the ideal gas model.

The van der Waals model makes corrections on the ideal gas model by accounting for real gas effects resulting from physical interactions of molecules. The ideal gas

model assumes that molecules are point masses in space with no volume. The van der Waals model attempts to approximate the volume that the molecules occupy; this effect is captured by the quantity b. Thus, the volume that molecules occupy in the van der Waals model is equal to the volume occupied in the ideal gas model, plus the volume of the molecules themselves. The second parameter a accounts for inter-molecular attraction. Even in the gas phase, the inter-molecular attraction leads to clumping of molecules tending to reduce the volume occupied by those molecules. However, when the volume of the gas is dictated by its container, this tendency towards attraction is expressed as a decrease in the pressure relative to the ideal gas. In the region of state space near the vapor dome, intermolecular forces become stronger as the gas nears a phase transition.

For this work, the specific heat at constant volume c_v is assumed to be constant. However, the anomalous region in the gas phase is very near the critical point, and the choice of a constant or variable specific heat at constant volume is briefly addressed for reference here. Assuming a constant specific heat at constant volume is a useful assumption, and has been done in the study of anomalous waves as in ([6],[25], [104],[113]). As detailed in [59], in the neighborhood of the critical point $c_v(T)$ can be approximated by the power law

$$c_v(T) = c^c_{v\infty} \left(\frac{T}{T_c} \right)^m . \tag{2.14}$$

The parameters m and $c^c_{v\infty}$ are dependent upon the fluid, and can be found for many BZT fluids in [79]. For the cases presented in this work, the difference in major results between constant and variable c_v is very small, and the choice was made to assume a constant value of c_v for tractability of analysis; thus, we take $m = 0$. Additional detail on the van der Waals equation of state with variable specific heat is given in Appendix A.

An additional useful expression is the frozen sound speed

$$c^2 = v^2 \left(p + \left.\frac{\partial e}{\partial v}\right|_{p,\lambda} \right) \Big/ \left.\frac{\partial e}{\partial p}\right|_{v,\lambda} = \frac{RT}{(1-b/v)^2}\left(1 + \frac{R}{c_v}\right) - \frac{2a}{v}, \tag{2.15}$$

where the specific volume v has been substituted for density with $v = 1/\rho$. This definition of the frozen sound speed is better defined for reactive systems, but is equivalent to $\partial p/\partial\rho|_{s,\lambda}$.

2.1.3 Reactive Euler Equations

In the inviscid limit, μ, k, and $\mathcal{D}$ go to zero, and the reactive Euler equations are recovered:

$$\frac{\partial \rho}{\partial t} + \frac{\partial}{\partial x}(\rho u) = 0, \tag{2.16}$$

$$\frac{\partial}{\partial t}(\rho u) + \frac{\partial}{\partial x}(\rho u^2 + p) = 0, \tag{2.17}$$

$$\frac{\partial}{\partial t}\left(\rho\left(e + \frac{1}{2}u^2\right)\right) + \frac{\partial}{\partial x}\left(\rho u\left(e + \frac{1}{2}u^2 + \frac{p}{\rho}\right)\right) = 0, \tag{2.18}$$

$$\frac{\partial}{\partial t}(\rho\lambda) + \frac{\partial}{\partial x}(\rho u\lambda) = \rho r, \tag{2.19}$$

$$r(T,\lambda) = A(1-\lambda)\exp\left(\frac{-\Theta}{RT}\right), \tag{2.20}$$

$$p(T,v) = \frac{RT}{v-b} - \frac{a}{v^2}, \tag{2.21}$$

$$e(T,v,\lambda) = c_v T - \frac{a}{v} - \lambda q. \tag{2.22}$$

Equations (2.16-2.18) are mass, momentum, and energy conservation, respectively, Eq. (2.19) is the reaction evolution, and Eqs. (2.20-2.22) are the reaction rate, pressure, and energy equations, respectively. To account for possible discontinuities, the Euler equations must be supplemented by the well known Rankine-Hugoniot jump

equations, [69, 103]:

$$\rho_2 \hat{u}_2 = \rho_1 \hat{u}_1, \tag{2.23}$$

$$\rho_2 \hat{u}_2^2 + p_2 = \rho_1 \hat{u}_1^2 + p_1, \tag{2.24}$$

$$e_2 + \frac{1}{2}\hat{u}_2^2 + \frac{p_2}{\rho_2} = e_1 + \frac{1}{2}\hat{u}_1^2 + \frac{p_1}{\rho_1}, \tag{2.25}$$

$$\lambda_2 = \lambda_1. \tag{2.26}$$

Subscripts 1 and 2 correspond to the unshocked and shocked states, respectively. These are written in the steady frame traveling at shock speed D, and the term $\hat{u}$ denotes the particle velocity in the wave frame: $\hat{u} = u - D$. The reaction progress does not change across the shock. This system is completed with the equations of state.

2.1.4 Non-Conservative Form

The non-conservative form of the reactive Navier-Stokes equations is given here:

$$\frac{\partial \rho}{\partial t} + u\frac{\partial \rho}{\partial x} = -\rho\frac{\partial u}{\partial x}, \tag{2.27}$$

$$\rho\left(\frac{\partial u}{\partial t} + u\frac{\partial u}{\partial x}\right) = -\frac{\partial p}{\partial x} + \frac{\partial \tau}{\partial x}, \tag{2.28}$$

$$\rho\left(\frac{\partial e}{\partial t} + u\frac{\partial e}{\partial x}\right) = -p\frac{\partial u}{\partial x} - \frac{\partial q}{\partial x} + \tau\frac{\partial u}{\partial x}, \tag{2.29}$$

$$\frac{\partial \lambda}{\partial t} + u\frac{\partial \lambda}{\partial x} + \frac{\partial j}{\partial x} = r, \tag{2.30}$$

$$r(T,\lambda) = A(1-\lambda)\exp\left(\frac{-\Theta}{RT}\right), \tag{2.31}$$

$$p(T,v) = \frac{RT}{v-b} - \frac{a}{v^2}, \tag{2.32}$$

$$e(T,v,\lambda) = c_v T - \frac{a}{v} - \lambda q, \tag{2.33}$$

$$\tau = \frac{4}{3}\mu\frac{\partial u}{\partial x}, \tag{2.34}$$

$$q = -k\frac{\partial T}{\partial x} + \rho\mathcal{D}q\frac{\partial \lambda}{\partial x}, \tag{2.35}$$

$$j = -\rho\mathcal{D}\frac{\partial \lambda}{\partial x} \tag{2.36}$$

The inviscid equations can be recovered by setting μ, k, and $\mathcal{D}$ to zero, and the inert equations by decoupling the reaction from the mass, momentum, and energy equations through the constitutive relations. The non-conservative forms of the governing equations are used for characteristic analysis, and provide an advantageous formulation for the application of numerical methods to the viscous model.

2.2 Transformation to the Piston-Attached Coordinate System

When modeling one-dimensional piston-driven shocks and detonations, it is convenient to transform the governing equations to a coordinate system attached to the piston face. For a general transformation of the independent variables $(x,t) \rightarrow (\xi,\hat{\tau})$

is expressed by

$$\xi = \xi(x,t), \qquad \hat{\tau} = \hat{\tau}(x,t). \tag{2.37}$$

The differential operators that result from this transformation are:

$$\left.\frac{\partial}{\partial t}\right|_x = \left.\frac{\partial \xi}{\partial t}\right|_x \left.\frac{\partial}{\partial \xi}\right|_{\hat{\tau}} + \left.\frac{\partial \hat{\tau}}{\partial t}\right|_x \left.\frac{\partial}{\partial \hat{\tau}}\right|_{\xi}, \tag{2.38}$$

$$\left.\frac{\partial}{\partial x}\right|_t = \left.\frac{\partial \xi}{\partial x}\right|_t \left.\frac{\partial}{\partial \xi}\right|_{\hat{\tau}} + \left.\frac{\partial \hat{\tau}}{\partial x}\right|_t \left.\frac{\partial}{\partial \hat{\tau}}\right|_{\xi}. \tag{2.39}$$

The piston position can be prescribed as a function of time, $x_p(t)$, and its velocity is then given by

$$v_p(t) = \frac{\mathrm{d}x_p(t)}{\mathrm{d}t}. \tag{2.40}$$

For the desired transformation from the laboratory frame to the piston frame, Eq. (2.37) becomes:

$$\xi = x - x_p(t), \qquad \hat{\tau} = t. \tag{2.41}$$

From here, we will now return to using t in place of $\hat{\tau}$. The transformed differential operators in Eqs. (2.38) and (2.39) now reduce to:

$$\left.\frac{\partial}{\partial t}\right|_x = -v_p(t) \left.\frac{\partial}{\partial \xi}\right|_t + \left.\frac{\partial}{\partial t}\right|_{\xi}, \tag{2.42}$$

$$\left.\frac{\partial}{\partial x}\right|_t = \left.\frac{\partial}{\partial \xi}\right|_t. \tag{2.43}$$

The particle velocity relative to the piston-attached coordinate system can be obtained by differentiating the first expression in Eq. (2.41):

$$\bar{u} = u - v_p(t). \tag{2.44}$$

Here $\bar{u} = \mathrm{d}\xi/\mathrm{d}t$ is the particle velocity in the piston-attached coordinate system, $u = \mathrm{d}x/\mathrm{d}t$ is the particle velocity in the laboratory frame, and $v_p(t)$ is the piston velocity function. Reducing Eqs. (2.1-2.4) to the inviscid reactive Euler equations, the transformations in Eqs. (2.42) and (2.43) are used to render the inviscid equations into the piston-attached coordinate frame:

$$\begin{aligned}
\frac{\partial \rho}{\partial t} + \frac{\partial}{\partial \xi}(\rho \bar{u}) &= 0, & (2.45)\\
\frac{\partial}{\partial t}(\rho \bar{u}) + \frac{\partial}{\partial \xi}(\rho \bar{u}^2 + p) &= -\rho \frac{\mathrm{d}v_p}{\mathrm{d}t}, & (2.46)\\
\frac{\partial}{\partial t}\left(\rho\left(e + \frac{1}{2}\bar{u}^2\right)\right) + \frac{\partial}{\partial \xi}\left(\rho \bar{u}\left(e + \frac{1}{2}\bar{u}^2 + \frac{p}{\rho}\right)\right) &= -\rho \bar{u} \frac{\mathrm{d}v_p}{\mathrm{d}t}, & (2.47)\\
\frac{\partial}{\partial t}(\rho \lambda) + \frac{\partial}{\partial \xi}(\rho \bar{u} \lambda) &= \rho r. & (2.48)
\end{aligned}$$

Equations (2.46) and (2.47), the linear momentum and energy equations, respectively, contain an extra term on the right hand side when transformed into the piston-attached coordinate system. These terms account for the acceleration of the coordinate frame as the piston itself accelerates. When the piston is at a steady velocity, these terms go to zero, and the system is invariant from that of the laboratory frame under what amounts to a Galilean transformation.

The boundary condition at the piston surface can be satisfied by requiring the velocity of the gas at the piston face to vanish in the piston-attached coordinates because it travels at the same speed as the piston: $\bar{u}(0,t) = 0$. This is equivalent to a no-penetration boundary condition at the piston surface. This is the only condition that can be explicitly enforced at the piston face.

CHAPTER 3

NUMERICAL METHODS

This chapter will address numerical methods used throughout this work. It begins with a short description of various methods used for algebraic systems and ordinary differential equations. The numerical methods chosen for parabolic and hyperbolic partial differential equations (PDEs) are introduced.

3.1 Algebraic Systems and Numerical Quadrature

There will be occasion to use many numerical algorithms for calculus, such as numerical integration, as well as solving algebraic systems. Many of these algorithms were utilized through applicable `Mathematica` commands [125]. Some integrals may require numerical integration with methods such as adaptive integration, exponential quadrature, or Monte Carlo integration, utilized by `NIntegrate`. Solutions with this command can be confirmed by specifying multiple methods and comparing results for consistency. Root-finding methods can be used to approximate solutions to nonlinear algebraic systems that cannot be solved exactly. Such methods include the Newton method when one initial guess is specified and the secant method when two initial guesses are specified, utilized by `FindRoot`. Systems of algebraic equations, such as the Rankine-Hugoniot jump equations, can be solved either symbolically or for specific initial values using the `Solve` command. A Discrete Fourier Transformation (DFT) is a useful tool for analysis of unstable detonations, as it provides details on the frequencies of the instability; DFTs can be computed using the `Fourier` command.

These commands allow for the specification of the desired precision for the final output as well as during the calculations. In general, these default to a working precision of 16 digits. This is often sufficient precision for our purposes, but occasionally requires adjustment. It is also possible to achieve arbitrary precision by expressing all numerical values as exact rational numbers using ratios of integers instead of finite precision decimal approximations, for example, inputting 1/4 instead of 0.25. This is sometimes necessary when working with algebraic systems involving the van der Waals equation of state, as it is possible for computational error to appear as small imaginary numbers on the order of machine precision. Expressing values with arbitrary precision enables distinction between true imaginary results and those with small numerical errors.

3.2 Ordinary Differential Equations

We often require numerical methods to generate approximate solutions to systems of nonlinear ordinary differential equations. For this we often use `Mathematica`'s `NDSolve`, which is an algorithm that selects appropriate numerical methods based on the equations given, including Adams, explicit and implicit Runge-Kutta, backwards difference, explicit and implicit Euler, and central difference schemes of various orders. This function requires the appropriate boundary or initial conditions be specified, and can be used on a single differential equation or on systems of differential equations. The precision goal can also be set for `NDSolve`.

3.3 Parabolic Systems of Partial Differential Equations

For the inert viscous problem, the modeling of fully resolved momentum and energy diffusion allows the use of simple discretizations for the parabolic system of equations. A first-order explicit Euler method in time and second-order centered spatial scheme were used for the numerical solution of the viscous model. The resulting

discretization of the inert one-dimensional Navier-Stokes equations are:

$$\rho_j^{n+1} = \rho_j^n + \Delta t \left(-\rho_j^n \frac{u_{j+1}^n - u_{j-1}^n}{2\Delta x} - u_j^n \left(\frac{\rho_{j+1}^n - \rho_{j-1}^n}{2\Delta x} \right) \right), \tag{3.1}$$

$$u_j^{n+1} = u_j^n + \Delta t \left(-\frac{1}{\rho_j^n} \left(\frac{p_{j+1}^n - p_{j-1}^n}{2\Delta x} \right) + \frac{4}{3} \frac{\mu}{\rho_j^n} \left(\frac{u_{j+1}^n - 2u_j^n + u_{j-1}^n}{\Delta x^2} \right) - u_j^n \left(\frac{u_{j+1}^n - u_{j-1}^n}{2\Delta x} \right) \right), \tag{3.2}$$

$$e_j^{n+1} = e_j^n + \Delta t \left(-\frac{p_j^n}{\rho_j^n} \left(\frac{u_{j+1}^n - u_{j-1}^n}{2\Delta x} \right) + \frac{k}{\rho_j^n} \left(\frac{T_{j+1}^n - 2T_j^n + T_{j-1}^n}{\Delta x^2} \right) + \frac{4}{3} \frac{\mu}{\rho_j^n} \left(\frac{u_{j+1}^n - u_{j-1}^n}{2\Delta x} \right)^2 - u_j^n \left(\frac{e_{j+1}^n - e_{j-1}^n}{2\Delta x} \right) \right), \tag{3.3}$$

$$T_j^{n+1} = \frac{1}{c_v} \left(e_j^{n+1} + a\rho_j^{n+1} \right), \tag{3.4}$$

$$p_j^{n+1} = \frac{RT_j^{n+1}}{\frac{1}{\rho_j^{n+1}} - b} - a \left(\rho_j^{n+1} \right)^2. \tag{3.5}$$

This simple time-explicit discretization enables a straightforward numerical solution via the method of lines. When the spatial discretization is sufficiently fine to capture the diffusion in the thin viscous shock structures, the time step is restricted by diffusion, not advection. This was done by satisfying the diffusion-based stability requirement of the explicit Euler method on the Navier-Stokes equations, specifically the von Neumann number with a factor of safety of 1/4, so Δt is calculated by $\Delta t = \Delta x^2/4/\max(\alpha, \nu)$. The denominator is determined by the maximum between the thermal diffusivity $\alpha = k/\rho/c_p$, where c_p is specific heat at constant pressure, and the maximum kinematic viscosity, $\nu = \mu/\rho$ across the domain. For simulations for which the Prandtl number equals 1, α and ν are equivalent for a given value of ρ. One-sided, second-order differences were employed at the boundaries for pressure and density with Dirichlet conditions on the velocity. Other state variables such as the temperature and specific internal energy can be computed using the equation of state. For viscous analysis, adiabatic, zero-velocity boundary conditions were employed on a closed domain.

3.4 Hyperbolic Systems of Partial Differential Equations

In the inviscid limit the governing equations are hyperbolic and admit discontinuities, and the inert case is strictly hyperbolic. The numerical scheme that has been chosen is a third order Runge-Kutta method in time and a fifth order Weighted Essentially Non-Oscillatory scheme with mapped weights, henceforth referred to as WENO5M, in space, first introduced by Henrick, et al. [65]. A variety of works have performed numerical stability analysis with various combinations of WENO schemes and time discretizations [67, 86], including fifth order WENO with third order Runge-Kutta. The WENO5M method is summarized in one dimension with uniform grid spacing, where nodes $j = 0, 1, \ldots, N_x$ have positions x_j, the flux values are given by f_j, and half indices are denoted by subscripts of $i \pm 1/2$. The full details of the WENO5M scheme and its derivation can be found in [65]. It is noted that although WENO5M is a fifth order scheme for smooth problems, the presence of discontinuities dictates that the highest order convergence that can be achieved for a shock capturing scheme is first order.

Consider a model problem given by

$$\frac{\partial \mathsf{u}}{\partial t} + \frac{\partial \mathsf{f}}{\partial x} = 0, \tag{3.6}$$

where t and x are the independent variables time and space, $\mathsf{u}(t, x)$ is a conserved variable, and $\mathsf{f}(\mathsf{u}(t, x))$ is the flux of u. This partial differential equation can then be approximated by a system of ordinary differential equations:

$$\frac{d\mathsf{u}_j}{dt} = -\frac{\mathsf{f}_{j+1/2} - \mathsf{f}_{j-1/2}}{\Delta x}. \tag{3.7}$$

The value of $\mathsf{f}_{j+1/2}$ describes the flux of the conserved variable u between two cells at j and $j + 1/2$. It is desired that the divided difference in Eq. (3.7) is an exact

derivative at x_j, and such a function is typically referred to as the numerical flux function, called $h(x)$. This numerical flux is related to the flux derivative by

$$\left.\frac{\partial \mathsf{f}}{\partial x}\right|_{x=x_j} = \frac{h_{j+1/2} - h_{j-1/2}}{\Delta x}. \tag{3.8}$$

The numerical flux is defined by Shu and Osher [112] as

$$\mathsf{f}(x) = \frac{1}{\Delta x}\int_{x-\Delta x/2}^{x+\Delta x/2} h(\xi)\ \mathrm{d}\xi. \tag{3.9}$$

Differentiating Eq. (3.9) returns Eq. (3.8), and is chosen as the replacement for the flux in Eq. (3.7). However, the flux described by Eq. (3.9) is not the exact flux function for a finite Δx [65].

Numerical schemes can be formulated by approximating the numerical flux function $h(x)$ using polynomial forms with undetermined coefficients. The resulting functions are denoted as $\hat{\mathsf{f}}(x)$, and after substituting into Eq. (3.9), the spatial derivative is now approximated by

$$\left.\frac{\mathrm{d}\mathsf{f}}{\mathrm{d}x}\right|_{x=x_j} \approx \frac{\hat{\mathsf{f}}_{j+1/2} - \hat{\mathsf{f}}_{j-1/2}}{\Delta x}. \tag{3.10}$$

A method has been devised to avoid spurious oscillations caused by discontinuous solutions affecting each of the nodes on the solution stencil. This involves using weighted linear combinations of three stencils, arranged as shown in Fig. 3.1. For WENO5M the numerical flux is calculated by

$$h_{j+1/2} \approx \hat{\mathsf{f}}_{j+1/2} = \sum_{k=0}^{2} \omega_k^{(M)} \hat{\mathsf{f}}_{j+1/2}^{k}. \tag{3.11}$$

where $\omega_k^{(M)}$ are the mapped weights of the kth stencil, and the $\hat{\mathsf{f}}^k$ are approximations of $h(x)$ for each of three stencils $k = [0, 1, 2]$.

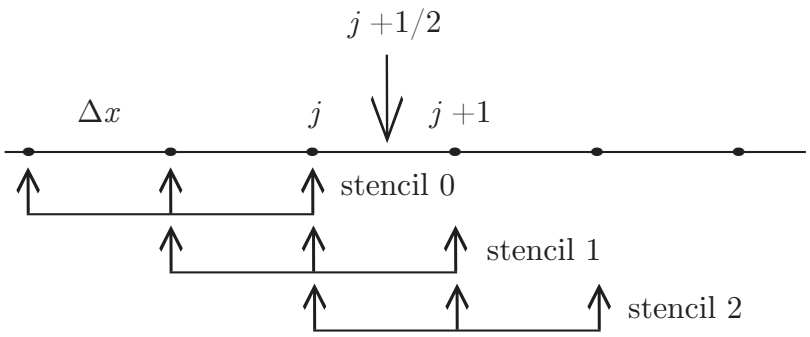

Figure 3.1. Stencils used for the numerical flux in fifth order WENO schemes.

The numerical flux for each stencil is derived in full in [65], and the final form is given by

$$\hat{\mathsf{f}}^0_{j+1/2} = \frac{1}{6}\left(2\mathsf{f}_{j-2} - 7\mathsf{f}_{j-1} + 11\mathsf{f}_j\right), \tag{3.12}$$

$$\hat{\mathsf{f}}^1_{j+1/2} = \frac{1}{6}\left(-\mathsf{f}_{j-1} + 5\mathsf{f}_j + 2\mathsf{f}_{j+1}\right), \tag{3.13}$$

$$\hat{\mathsf{f}}^2_{j+1/2} = \frac{1}{6}\left(2\mathsf{f}_j + 5\mathsf{f}_{j+1} - \mathsf{f}_{j+2}\right). \tag{3.14}$$

The mapped weights $\omega_k^{(M)}$, first presented by Henrick et al. [65], are an adjustment on the weights as they were originally formulated by Jiang and Shu [71]. The mapped weights, $w_k^{(M)}$, are defined as:

$$\omega_k^{(M)} = \frac{\alpha_k^*}{\Sigma_{i=0}^2 \alpha_i^*}, \tag{3.15}$$

with the α_k^* determined by:

$$\alpha_k^* = g_k(\omega_k^{(JS)}) = \frac{\omega\left(\bar{\omega_k} + \bar{\omega}_k^2 - 3\bar{\omega}_k\omega + \omega^2\right)}{\bar{\omega}_k^2 + \omega(1 - 2\bar{\omega}_k)}. \tag{3.16}$$

Equations (3.15) and (3.16) define the modified weights, which use the ideal weights of regions with smooth flow, $\bar{\omega}_{k=0,1,2} = [1/10, 6/10, 3/10]$, and the weights as developed

in [71], $\omega_k^{(JS)}$:

$$\omega_k^{(JS)} = \frac{\alpha_k}{\Sigma_{i=0}^{2}\alpha_i}, \tag{3.17}$$

where

$$\alpha_k = \frac{\bar{\omega}_k}{(\epsilon + \beta_k)^p}. \tag{3.18}$$

The indicator of smoothness β_k is calculated for each stencil. The parameters p and ϵ are adjustable parameters of the WENO method. For our purposes, $p = 2$ is used. The value of ϵ serves to prevent the denominator in Eq. (3.18) from going to zero, and can be adjusted on a case-by-case basis. Both the machine being used, along with the properties of the flow, can affect the choice of ϵ. In smooth flows, the predictions of the WENO5M scheme approach a central difference scheme as ϵ begins to dominate, so choosing too large of an ϵ value can mitigate the expected behavior of a WENO method. The results presented here are concerned with shocks, and the choice of ϵ is not so consequential; all calculations in this work have been done with $\epsilon = 1 \times 10^{-6}$. Henrick, et al. [65] show for smooth oscillatory solutions that this choice of ϵ can degrade the order of accuracy from fifth to third order. For our problems with shocks, all WENO methods converge at less than first order, however, so the value of ϵ is not particularly important.

The β_k values, called the indicators of smoothness, provide a measurement of the smoothness of the flux function for each stencil. It is through these β values that the WENO scheme weights the stencils by smoothness. For the three stencils, these β values are calculated with:

$$\beta_0 = \frac{13}{12}\left(\mathsf{f}_{j-2} - 2\mathsf{f}_{j-1} + \mathsf{f}_j\right)^2 + \frac{1}{4}\left(\mathsf{f}_{j-2} - 4\mathsf{f}_{j-1} + 3\mathsf{f}_j\right)^2, \tag{3.19}$$

$$\beta_1 = \frac{13}{12}\left(\mathsf{f}_{j-1} - 2\mathsf{f}_j + \mathsf{f}_{j+1}\right)^2 + \frac{1}{4}\left(\mathsf{f}_{j+1} - \mathsf{f}_{j-1}\right)^2, \tag{3.20}$$

$$\beta_2 = \frac{13}{12}\left(\mathsf{f}_j - 2\mathsf{f}_{j+1} + \mathsf{f}_{j+2}\right)^2 + \frac{1}{4}\left(3\mathsf{f}_j - 4\mathsf{f}_{j+1} + \mathsf{f}_{j+2}\right)^2. \tag{3.21}$$

The WENO5M scheme as it has been described forces information to propagate from left to right, as a result of the stencil bias. The scheme can be reversed to propagate information from right to left, and is thus constructed by reflecting indices across the $(j+1/2)$ interface:

$$\hat{h}[\mathsf{f}]_{j+1/2} = \begin{cases} \mathcal{F}(\mathsf{f}_{j-2}, \mathsf{f}_{j-1}, \ldots, \mathsf{f}_{j+2}), \\ \mathcal{F}(\mathsf{f}_{j+3}, \mathsf{f}_{j+2}, \ldots, \mathsf{f}_{j-1}), \end{cases} \tag{3.22}$$

where $\mathcal{F}$ represents the functional form of the WENO method, Eq. (3.11) for WENO5M. However, a scheme is required that allows for propagation of information in both directions, left to right and right to left. To achieve this, a flux splitting scheme is necessary, as the split fluxes account for the information propagating to the left and the right. The introduction of non-convexity complicates the selection of the flux splitting scheme.

The details of a general Lax-Friedrichs flux splitting scheme will first be presented. The spatial derivative is rewritten as:

$$\frac{\partial \mathsf{f}}{\partial x} = \frac{\partial}{\partial x}(\mathsf{f}(\mathsf{u}(x))) = \frac{\partial \mathsf{f}}{\partial \mathsf{u}} \frac{\partial \mathsf{u}}{\partial x}, \tag{3.23}$$

where $\partial \mathsf{f}/\partial \mathsf{u}$ is the Jacobian matrix of the system, the eigenvalues of which represent the wave speeds of the system [30, 121]. The sign of these eigenvalues corresponds to the direction in which the respective characteristics propagate. Taking the absolute value of these eigenvalues, the maximum is the largest wave speed of the system, a quantity that will here be referred to as α_m. Using this value, the flux vector can be rewritten, and the spatial derivative becomes:

$$\frac{\partial \mathsf{f}}{\partial x} = \frac{\partial}{\partial x}\left(\frac{1}{2}(\mathsf{f} + \alpha_m \mathsf{u} + \mathsf{f} - \alpha_m \mathsf{u})\right) = \frac{1}{2}\left(\frac{\partial \mathsf{f}^+}{\partial x} + \frac{\partial \mathsf{f}^-}{\partial x}\right). \tag{3.24}$$

Using the notation of the numerical flux, and its approximation, the spatial derivative is now discretized with the split fluxes:

$$\begin{aligned}\left.\frac{\partial \mathsf{f}}{\partial x}\right|_{x=x_j} &\approx \frac{1}{2}\left(\frac{h^+_{j+1/2}-h^+_{j-1/2}}{\Delta x}+\frac{h^-_{j+1/2}-h^-_{j-1/2}}{\Delta x}\right),\\ &\approx \frac{1}{\Delta x}\left(\frac{h^+_{j+1/2}+h^-_{j+1/2}}{2}-\frac{h^+_{j-1/2}+h^-_{j-1/2}}{2}\right),\\ &\approx \frac{\hat{\mathsf{f}}_{j+1/2}-\hat{\mathsf{f}}_{j-1/2}}{\Delta x}.\end{aligned} \tag{3.25}$$

As written in Eq. (3.25), the LF flux splitting has not been paired with a specific numerical scheme for the h values. In the case of the WENO5M scheme, the f^+ flux vector is used for the left-to-right biased implementation, and the f^- flux vector for the right-to-left biased implementation.

$$h[\mathsf{f}^\pm]_{j+1/2} = \begin{cases}\mathcal{F}(\mathsf{f}^+_{j-2},\mathsf{f}^+_{j-1},\ldots,\mathsf{f}^+_{j+2}),\\ \mathcal{F}(\mathsf{f}^-_{j+3},\mathsf{f}^-_{j+2},\ldots,\mathsf{f}^-_{j-1}).\end{cases} \tag{3.26}$$

As given in [65], one way to determine the value of α_m is to do so locally, utilizing the largest magnitude of the eigenvalues at each point on the stencil for point j. However, when the flow is split between the convex and non-convex regions and the sound speed is non-monotonic this method can result in instabilities. For example, referring to the grid in Fig. 3.1, if there is a local minimum in the sound speed at j, there are higher values of the sound speed on either side of this point, at $j-2$, $j-1$, $j+1$, and $j+2$. The eigenvalue with the largest magnitude may not correspond to the correct wave motion in this case, leading to oscillations or instabilities. These can be avoided using a global approach to the value of α_m. This entails scanning the entire grid to find the eigenvalue with the largest absolute value in the flow field, and using this single value for α_m at all points on the grid. It is important to select a flux splitting scheme that does not rely on monotonicity when working with BZT fluids

in and near the BZT region, as anomalous behavior is expected in these regions.

CHAPTER 4

STEADY INERT WAVE DYNAMICS

This chapter presents dynamics of steadily propagating waves in an inert van der Waals gas. It begins with a discussion of entropy and the second law of thermodynamics, followed by a review of weak solutions to partial differential equations, and a discussion of the fundamental derivative. Analysis is done of Rayleigh line and Hugoniot curves as well as Rankine-Hugoniot jump conditions for compression and rarefaction discontinuities. Examples of each are shown. Additional detail can be found in Menikoff and Plohr's extensive work on waves in real gases [83]. Numerical simulations of shocks in a viscous van der Waals gas are also computed, and are shown to be vital tool for determining correct shock solutions when anomalous waves are present. The examples in this chapter are computed with parameters for the material PP10.

4.1 Entropy and the Second Law of Thermodynamics

The second law of thermodynamics must always hold. In the inert limit, it can be written as:

$$\frac{\partial}{\partial t}(\rho s) + \frac{\partial}{\partial x}(\rho u s) = -\frac{\partial}{\partial x}\left(\frac{\mathsf{q}}{T}\right) + \dot{\mathcal{I}}, \quad \dot{\mathcal{I}} \geq 0, \tag{4.1}$$

where s is the specific entropy, and $\dot{\mathcal{I}}$ is the irreversibility production rate, a positive semi-definite scalar function. The specific entropy for an inert van der Waals gas with constant c_v can by found by integrating the Gibbs equation, $T\ \mathrm{d}s = \mathrm{d}e + p\ \mathrm{d}v$.

Some algebraic manipulation results in

$$s(T,v) = s_o + c_v \ln\left(\frac{T}{T_o}\right) + R\ln\left(\frac{v-b}{v_o-b}\right), \tag{4.2}$$

where s_o, T_o, and v_o are reference values of the entropy, temperature, and specific volume, respectively.

For an analysis of the second law of thermodynamics in the inert viscous case, an expression is desired for the irreversibility production rate, which as derived in [81] is:

$$\dot{\mathcal{I}} = \frac{k}{T^2}\left(\frac{\partial T}{\partial x}\right)^2 + \frac{4}{3}\frac{\mu}{T}\left(\frac{\partial u}{\partial x}\right)^2 \geq 0. \tag{4.3}$$

This is also known as the weak form of the Clausius-Duhem inequality in one dimension. One may consider a more general satisfaction of the second law through the strong form of the Clausius-Duhem inequality in which both terms in Eq. (4.3) are constrained to be positive semi-definite. As a result, under the strong form's more restrictive definition, $k \geq 0$ and $\mu \geq 0$ are required. In either case, to satisfy the second law, $\dot{\mathcal{I}}$ must always be non-negative. Note the units of $\dot{\mathcal{I}}$ are $\mathrm{W/m^3/K}$, not those of entropy.

4.2 Weak Solutions

It is possible for solutions of conservation laws to exist that are not themselves differentiable functions, typically referred to as weak solutions. As discussed by Dafermos [39], the existence of weak solutions is settled for scalar conservation laws, and at least partially for one-dimensional systems. The short discussion here of weak solutions is drawn from LeVeque [80], and a more detailed analysis can be found in [39].

It is natural to return to the integral form of a conservation law to define a solution that does not require differentiability, but by taking a slightly different approach a

more convenient integral formulation can be reached. This is done by multiplying the PDE by a smooth test function, integrating one or more times, and rearranging with integration by parts to move derivatives from the conserved variable to the smooth test function. Let us consider a general conservation law for a conserved variable u with flux $\mathsf{f}(\mathsf{u})$

$$\frac{\partial \mathsf{u}}{\partial t} + \frac{\partial \mathsf{f}(\mathsf{u})}{\partial x} = 0, \tag{4.4}$$

and its integral form

$$\int_{x_1}^{x_2} \mathsf{u}(x, t_2)\, \mathrm{d}x = \int_{x_1}^{x_2} \mathsf{u}(x, t_1)\, \mathrm{d}x + \int_{t_1}^{t_2} \mathsf{f}(\mathsf{u}(x_1, t))\, \mathrm{d}t - \int_{t_1}^{t_2} \mathsf{f}(\mathsf{u}(x_2, t))\, \mathrm{d}t, \tag{4.5}$$

with a smooth test function $\phi(x, t)$. The test functions are defined on $\phi \in C_0^1(\mathbb{R} \times \mathbb{R})$, where C_0^1 is the space of functions that are continuously differentiable with compact support. A function's support is the subset of the function domain for which the elements are not mapped to zero, and a function with compact support has a support that is a closed and bounded subset. The requirement for compact support indicates that $\phi(x, t)$ is zero outside of a bounded set, so the function's support lies in a compact set [39]. Multiplying the conservation law by $\phi(x, t)$ and integrating over space and time, we obtain

$$\int_0^\infty \int_{-\infty}^\infty \left(\phi \frac{\partial \mathsf{u}}{\partial t} + \phi \frac{\partial \mathsf{f}(\mathsf{u})}{\partial x} \right) \mathrm{d}x\, \mathrm{d}t = 0. \tag{4.6}$$

Integration by parts over the time integral yields

$$\begin{aligned} &\int_0^\infty \int_{-\infty}^\infty \left(\frac{\partial \phi}{\partial t} \mathsf{u} + \frac{\partial \phi}{\partial x} \mathsf{f}(\mathsf{u}) \right) \mathrm{d}x\, \mathrm{d}t = \\ &\int_{-\infty}^\infty [\phi(x, \infty)\mathsf{u}(x, \infty) - \phi(x, 0)\mathsf{u}(x, 0) + \phi(x, \infty)\mathsf{f}(\mathsf{u})(x, \infty) - \phi(x, 0)\mathsf{f}(x, 0)]\, \mathrm{d}x. \end{aligned} \tag{4.7}$$

Because ϕ is required to have compact support, it vanishes at infinity; thus, the terms on the right hand side containing $\phi(x, \infty)$ drop out. Additionally, the flux at $t = 0$ is

also 0, so the term containing $f(x,0)$ also drops out. The only boundary term that remains includes the initial conditions of the PDE, which must still be accounted for by the weak solution. The resulting equation is

$$\int_0^\infty \int_{-\infty}^\infty \left(\frac{\partial \phi}{\partial t} \mathsf{u} + \frac{\partial \phi}{\partial x} \mathsf{f}(\mathsf{u}) \right) \mathrm{d}x \, \mathrm{d}t = - \int_{-\infty}^\infty \phi(x,0) \mathsf{u}(x,0) \, \mathrm{d}x. \tag{4.8}$$

Written in this form, it can be seen that the solution $\mathsf{u}(x,t)$ need not be a continuous function, as differentiation has been shifted to the smooth test function.

Considering special test functions that follow

$$\phi(x,t) = \begin{cases} 1 & \text{for} \quad (x,t) \in [x_1, x_2] \times [t_1, t_2] \,, \\ 0 & \text{for} \quad (x,t) \notin [x_1 - \epsilon_x, x_2 + \epsilon_x] \times [t_1 - \epsilon_t, t_2 + \epsilon_t] \,, \end{cases} \tag{4.9}$$

with smooth ϕ in the intermediate regions of width (ϵ_x, ϵ_t). This results in $\partial\phi/\partial x = \partial\phi/\partial t = 0$ everywhere other than the intermediate region, and Eq. 4.8 reduces to an integral in x and t over the strip of width ϵ_x and ϵ_t respectively. As $\epsilon_x \to 0$ and $\epsilon_t \to 0$, the derivatives of the test function approach delta functions, and Eq. 4.8 approaches the integral form in Eq. 4.5.

Weak solutions may not be unique if discontinuities are present. For the inviscid Euler equations, discontinuous weak solutions represent shock waves: discontinuous jumps in the state variables that satisfy the governing differential equations. There may be multiple such weak solutions, and conditions imposed by physics must be used to determine which, if any, of these solutions are physical. Satisfaction of the second law of thermodynamics is typically the first condition considered to determine the the correct weak solution, but the second law alone may not be sufficient for this purpose. Other admissibility conditions must be considered, and for this work we will utilize viscous solutions to determine the correct shock solution.

When considering viscous solutions, it is expected that solutions of the parabolic

system

$$\frac{\partial \mathsf{u}}{\partial t} + \frac{\partial \mathsf{f}(\mathsf{u})}{\partial x} = \epsilon \frac{\partial^2 \mathsf{u}}{\partial x^2}, \tag{4.10}$$

coincide with solutions of the hyperbolic system in the limit as the viscosity coefficient $\epsilon \to 0$. Because Eq. 4.10 is parabolic, even if the initial conditions are discontinuous, there will always be a smooth unique solution for $t > 0$ [39]. Thus, if a unique weak solution cannot be determined by the second law of thermodynamics alone, the vanishing viscosity limit should single out the correct physical weak solution.

4.3 Fundamental Derivative

Not all equations of state admit anomalous waves, and determining constitutive relations that are valid for studies of anomalous behavior can be done using the dimensionless fundamental derivative of gas dynamics $\mathcal{G}$, introduced by Thompson [119] and defined by:

$$\mathcal{G}(s,v) \equiv -\frac{\frac{v}{2}\left.\frac{\partial^2 p}{\partial v^2}\right|_s}{\left.\frac{\partial p}{\partial v}\right|_s} = \frac{v^3}{2c^2}\left.\frac{\partial^2 p}{\partial v^2}\right|_s. \tag{4.11}$$

Because $v^3/2/c^2$ is always positive, the sign of $\mathcal{G}$ is determined by $\partial^2 p/\partial v^2|_s$. The fundamental derivative gives a measure of the convexity of isentropes in the p-v plane, and determines how the sound speed varies across simple waves [83]. It can be shown that if $\mathcal{G} > 0$, the isentropes are convex, and if $\mathcal{G} < 0$ isentropes are non-convex. The convexity of the isentropes, indicated by the sign of $\mathcal{G}$, determines the types of waves that are admissible: when $\mathcal{G} > 0$, only classical discontinuous compressions and continuous rarefactions will form, and when $\mathcal{G} < 0$, only anomalous discontinuous rarefaction and continuous compression waves will form. Flows for which the fundamental derivative undergoes a transition between positive and negative allow for composite waves to form. For some equations of state, including the ideal gas equa-

tion (for which $\mathcal{G} = (\gamma + 1)/2$, γ being the ratio of specific heats), the fundamental derivative is always positive, prohibiting the formation of anomalous waves.

Using Eqs. (2.6, 2.15, 4.2, 4.11), the fundamental derivative for a van der Waals gas can be written as

$$\mathcal{G}(v,s) = \frac{v^3}{2c^2}\left(-\frac{6a}{v^4} + \frac{RT_o}{c_v}\left(\frac{R}{c_v}+2\right)\frac{R+c_v}{(v-b)^3}\left(\exp\left(\frac{s-s_o}{c_v}\right)\right)\left(\frac{v-b}{v_o-b}\right)^{-R/c_v}\right). \tag{4.12}$$

In this form, it is difficult to determine what in Eq. (4.12) induces negative values of the fundamental derivative for a van der Waals gas. Taylor series expansion of $\mathcal{G}(v,T)$ in the limit of small a and b yields a linear approximation as

$$\mathcal{G}(v,T) = \frac{2c_v + R}{2c_v} + \frac{(2c_v+R)b}{2c_v v} - \frac{(c_v - R)a}{R(c_v+R)Tv} + \ldots. \tag{4.13}$$

The first term is the value of $\mathcal{G}$ for an ideal gas, and is always positive because c_v and R are always positive. The second term is likewise positive because in addition to the previous terms, b and v are always a positive quantities. The third term, expansion around small a, will always be a negative contribution if $c_v > R$. While this simple expansion is limited, it agrees with the detailed analysis in [25], concluding that it is the intermolecular attraction, corrected for in the van der Waals equation with the parameter a, that introduces the possibility of $\mathcal{G} < 0$.

The region of negative fundamental derivative in the gas phase, where anomalous waves are admitted, is typically found in the neighborhood of the critical point. The anomalous, or BZT, region is often limited to a small portion of thermodynamic state space. The upper boundary on this region is the curve $\mathcal{G} = 0$, below which $\mathcal{G}$ is negative. This can be found by converting $\mathcal{G}(s,v)$ to $\mathcal{G}(p,v)$, setting this equal to zero, and solving for pressure as a function of specific volume. For a van der Waals

gas the resulting function is

$$p(v) = \frac{6c_v a}{v^4} \frac{(v-b)^2}{(R+c_v)(R/c_v+2)} - \frac{a}{v^2}. \tag{4.14}$$

The lower limit of this region is the saturation curve, below which equations of state are no longer valid, although the fundamental derivative may still appear to be negative.

4.4 Material Parameters

For this study of anomalous waves in an inert van der Waals gas, example calculations have been done for the fluorocarbon PP10 ($C_{13}F_{22}$), and necessary parameters are given in Table 4.1 [25]. The values of k and μ for PP10 are difficult to identify; thus, μ was estimated by approximation to the gaseous fluorocarbon family [43], and k was calculated from an estimated Prandtl number of 1, where the Prandtl number is $Pr = \nu/\alpha$. As a consequence, it is seen that the thermal diffusivity, $\alpha = k/\rho/c_p$, and the kinematic viscosity, $\nu = \mu/\rho$, are equal for a given value of ρ and T. In Table 4.1, α_o and ν_o are the thermal and momentum diffusivities evaluated at the reference state with $\rho_o = 285$ kg/m^3 and $c_{po} = 1150$ J/kg/K. For a van der Waals gas, the specific heat at constant pressure c_p is not constant. It is noted for PP10 in and around the anomalous region, temperature and specific volume variations, and thus variations in c_p, are small.

Some features of PP10 in the $p-v$ plane, modeled with the van der Waals equation of state are shown in Fig. 4.1, including a fully convex shock adiabat, the $\mathcal{G} = 0$ curve, the critical isotherm and the shock adiabat passing through the critical point, both with non-convex sections, and the critical point. Consistent with the van der Waals model, the critical point lies at an inflection point on the critical isotherm. The anomalous region is bounded on the top by the $\mathcal{G} = 0$ curve. For our purposes, the

TABLE 4.1

PARAMETERS FOR PP10

R, J/kg/K	c_v J/kg/K	a, m^5/kg/s^2	b, m^3/kg	μ, Pa s
14.484	1131.588	22.389	7.244×10^{-4}	1.100×10^{-5}
k, W/m/K	α_o, m^2/s	ν_o m^2/s	P_c, Pa	T_c, K
1.261×10^{-2}	3.860×10^{-8}	3.860×10^{-8}	1.580×10^{6}	632.2

lower bound is set as the critical isotherm; doing so ensures the flow remain outside of the vapor dome. In the anomalous region, $\mathcal{G} < 0$, indicating that the convexity of isentropes is negative, and the types of waves that can form are rarefaction shocks and continuous homeoentropic compression fans.

The viscous solutions presented in this chapter were calculated using the numerical method in Section 3.3, as an exact solution was not available for a viscous shock in a van der Waals gas. As a starting point for ensuring the viscous shock is captured, the exact solution for a viscous ideal gas has been used to estimate the shock thickness for the material parameters in Table 4.1. Introduced by Taylor [117] and revisited by Becker [8], Morduchow and Libby [85], von Mises [120], Gilbarg and Paolucci [57], Ianelli [70], Myong [87], Bird, et al. [14], and many others, the solution is cast in our own nomenclature as

$$\hat{x}(\hat{u}) = \hat{x}_{in} - \frac{8\gamma\mu}{3(\gamma+1)\rho_1(\hat{u}_1 - \hat{u}_2)} \ln\left(\frac{\left(\frac{\hat{u}-\hat{u}_2}{\hat{u}_{in}-\hat{u}_2}\right)^{\frac{\hat{u}_2}{\hat{u}_1}}}{\left(\frac{\hat{u}_1-\hat{u}}{\hat{u}_1-\hat{u}_{in}}\right)} \right), \tag{4.15}$$

where $\hat{x}_{in}$ and $\hat{u}_{in}$ serve as spatial and velocity coordinates required to fix the solution in space at a given velocity, and $\hat{u}_1$ and $\hat{u}_2$ are the far-field upstream and downstream particle velocities in the wave frame. A detailed derivation is provided in Appendix B,

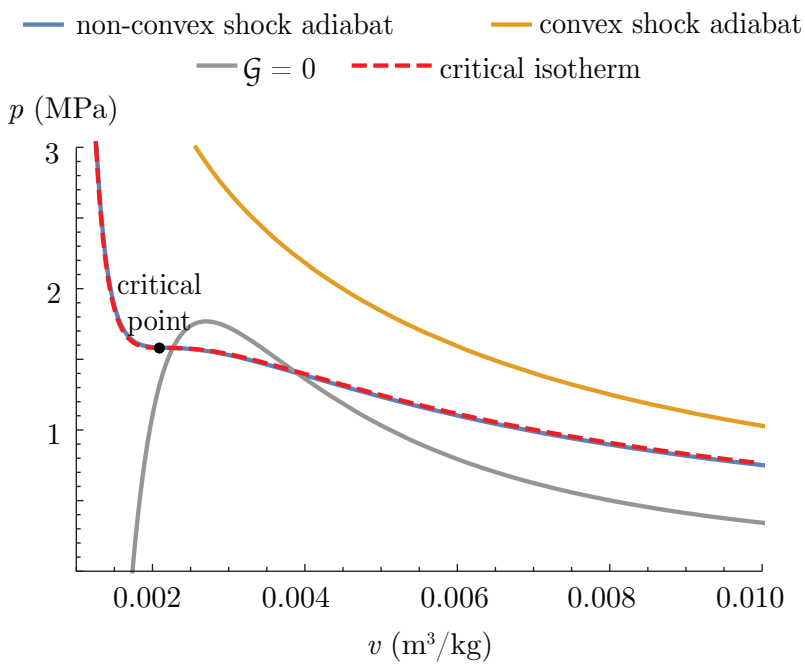

Figure 4.1. Features of the $p - v$ plane for PP10, including the critical isotherm, along with convex and non-convex shock adiabats, the $\mathcal{G} = 0$ curve, and the critical point.

which draws significantly from the presentation of Ghia, et al. [56]. The analytical solution exists in the steady frame, and the thickness of the shock wave is determined by:

$$L_{shock} = \frac{8\gamma\mu}{3(\gamma+1)\rho_1(\hat{u}_1 - \hat{u}_2)}. \tag{4.16}$$

To capture the physical structure of the viscous shock wave in numerical simulations, the spatial grid must be sufficiently small to capture L_{shock}. The physical time scale is diffusion-driven and well estimated by $t_{shock} = L_{shock}^2/\alpha$, and the time steps must be sufficiently small in order to capture the physical effects. For PP10 with the parameters given in Table 4.1, L_{shock} and t_{shock} are on the order of 10^{-9} m and 10^{-11} s, respectively. The small length scales used in this chapter are dictated by the viscous shock thickness, as the inviscid solutions are scale invariant. In addition to stability requirements, all numerical simulations for the viscous case require that the

time steps Δt and spatial steps Δx be less than the t_{shock} and L_{shock} values for the material parameters being used.

4.5 Rayleigh Line and Hugoniot Curve Analysis

Manipulation of the Rankine-Hugoniot jump conditions for the inert case, given in Eqs. (2.23-2.25), yields two useful equations, the Rayleigh line and Hugoniot curve. First, considering the jumps in mass and linear momentum, Eqs. (2.23) and (2.24), and substituting $v = 1/\rho$, an expression for the Rayleigh line is written as

$$p = p_o - \frac{D^2}{v_o}\left(\frac{v}{v_o} - 1\right). \tag{4.17}$$

The Rayleigh line is independent of the equation of state, and is a consequence of mass and linear momentum conservation only. Its slope is strictly negative, and is proportional to the square of the wave speed.

The jump in energy is now considered, Eq. (2.25). Using the mass and momentum jumps (2.23-2.24), along with the Rayleigh line (4.17), the energy jump can be rewritten independent of the velocities and the wave speed as

$$e - e_o = -\frac{p + p_o}{2}\left(v - v_o\right). \tag{4.18}$$

In this form, this is the Hugoniot equation for a general material, and does not depend on the state equation, the wave speed, or the particle velocity. Specifying the equation of state, the Hugoniot curve can be expressed as $p(v)$. For the van der Waals equation of state this yields

$$p = \frac{p_o\left(\frac{c_v}{R}\left(v_o - b\right) + \frac{v_o - v}{2}\right) - a\frac{c_v}{R}\left(\frac{b}{v_o^2} - \frac{b}{v^2} - \frac{1}{v_o} + \frac{1}{v}\right) - a\left(\frac{1}{v_o} + \frac{1}{v}\right)}{\frac{c_v}{R}\left(v - b\right) - \frac{1}{2}\left(v_o - v\right)}. \tag{4.19}$$

We are interested in intersection points between the Rayleigh line and the Hugoniot

curve. Algebraic manipulation leads to a single quartic equation for the shocked state specific volume v_2. There are four possible solutions for v_2 from this equation, and these roots may have real or imaginary values. With β_j the coefficient for v_2^j, this equation can be written as:

$$\beta_4 v_2^4 + \beta_3 v_2^3 - \beta_2 v_2^2 - \beta_1 v_2^1 - \beta_0 = 0, \tag{4.20}$$

$$\beta_4 = -\frac{D^2}{v_1^2}\left(\frac{1}{2} + \frac{c_v}{R}\right), \tag{4.21}$$

$$\beta_3 = p_1\left(1 + \frac{c_v}{R}\right) + \frac{D^2}{v_1}\left(\frac{3}{2} + \frac{c_v}{R}\left(1 + \frac{b}{v_1}\right)\right), \tag{4.22}$$

$$\beta_2 = v_1 p_1\left(1 + \frac{c_v}{R}\right) - \frac{ab}{v_1^2}\frac{c_v}{R} + \frac{1}{v_1}\left(\frac{c_v}{R}\left(D^2 b - a\right) + a\right) + \frac{D^2}{2} - q\lambda, \tag{4.23}$$

$$\beta_1 = a\left(1 - \frac{c_v}{R}\right), \tag{4.24}$$

$$\beta_0 = ab\frac{c_v}{R}. \tag{4.25}$$

It will be shown that in the classical case there are only two real intersection points of the Rayleigh line and the Hugoniot curve. As a result, solving Eqs. (4.20-4.25) returns two real roots and two imaginary roots. However, in the anomalous case, there may be up to four intersection points of the Rayleigh line and the Hugoniot curve corresponding to up to four real roots.

A plot of the Hugoniot curve and two Rayleigh lines with initial conditions $p_o = 2.0 \times 10^6$ Pa and $v_o = 0.0035$ m^3/kg is shown in Fig. 4.2. The Hugoniot curve is entirely within the region of state space where isentropes are convex, and classical behavior is expected. The Hugoniot curve is everywhere convex, and the Rayleigh lines have at most two intersection points, corresponding to two real roots of the Rankine-Hugoniot jump equations; the other two roots are complex. The shock speeds chosen were $D = 100$ m/s, and $D = 69.366$ m/s; the first choice allows for a clear illustration of the intersection points, and the second choice corresponds to a shock that will be a part of the shock tube solutions in a later section. The

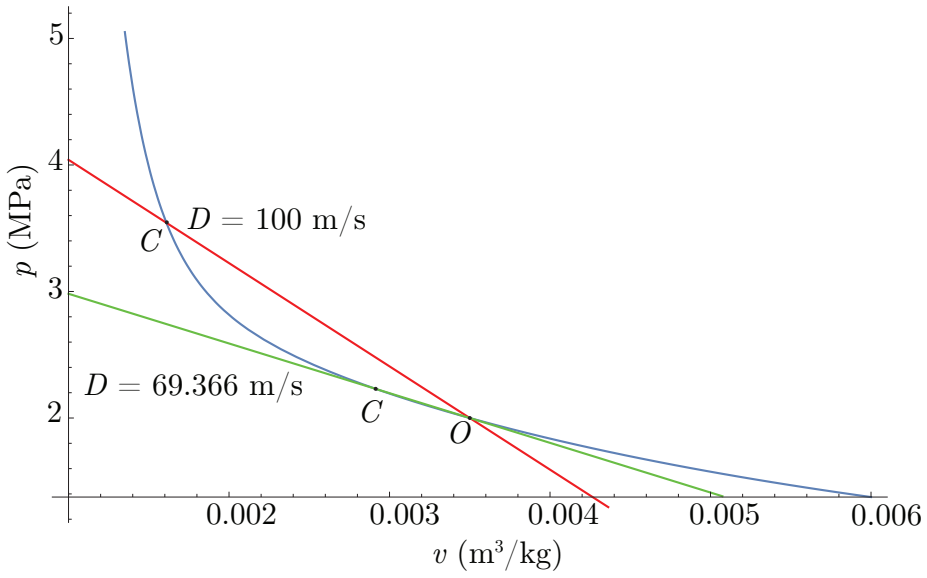

Figure 4.2. Rayleigh lines and Hugoniot curve in the convex region of state space for PP10 modeled as a van der Waals gas. The two intersection points correspond to two real roots of the Rankine-Hugoniot jump equations; the remaining two roots are complex.

initial condition is labeled O, and the ambient state is one solution. The second intersection, indicated by C, is the shock solution. In this case, pressure increases and specific volume decreases (corresponding to an increase in density), and the shock is a compression shock. Two Rayleigh lines are shown; the higher shock speed leads to a greater increase in the pressure and decrease in the specific volume. The minimum wave speed occurs when the Rayleigh line is tangent to the Hugoniot curve at the point O, and indicates the formation of a sonic wave; for this case, the corresponding value is $D = 69.695$ m/s. Wave speeds lower than this correspond to pressure decreases, typically accompanied by entropy decreases, which are non-physical.

When passing through the anomalous region, Hugoniot curves, like isentropes, also have regions of non-convexity corresponding to anomalous shock behavior. For the initial state $p_o = 1.74 \times 10^6$ Pa, $v_o = 0.0027$ m^3/kg, and shock speed $D = 37.813$ m/s the corresponding Rayleigh line and Hugoniot curve are shown in Fig. 4.3;

a sketch of all intersections is shown in Fig. 4.3(a). In this case, there are four intersection of the Rayleigh line and Hugoniot curve, which is only possible because the Hugoniot curve is non-convex. The first is the initial condition O, the unshocked ambient solution, which is on the non-convex part of the Hugoniot curve. The second intersection at C corresponds to an increase in pressure and density, as for a classical compression shock, and lies on the convex section of the Hugontiot curve. The third intersection at R also lies on the non-convex portion of the Hugoniot curve, and corresponds to a decrease in pressure and density and increase in specific volume as for a rarefaction shock. The fourth intersection is far to the right of the initial state at A. Classical interpretation tells us that the rarefaction shocks are non-physical, and the entropy would be expected to decrease. This is not necessarily true though, and one must rely upon additional methods to determine admissible shocks for this case.

4.6 Rankine-Hugoniot Jump Analysis

This section extends the Rayleigh line and Hugoniot curve analysis in order to determine admissible shock solutions, particularly when there are more than two intersections of the Rayleigh line with the Hugoniot curve. For shock discontinuities in the inviscid limit, the inert Rankine-Hugoniot jump conditions in Eqs. (2.23-2.25), along with the van der Waals equation of state, form a system of equations that when solved give the possible shocked states corresponding to a given initial state and shock speed. Solving this system of equations leads to four possible solutions. Not all of these roots are admissible shock solutions, and one root is the trivial unshocked solution. The first admissibility condition employed is satisfaction of the second law of thermodynamics. Solutions for which the change in entropy of a fluid particle is negative or imaginary are inadmissible. It will also be useful to determine the Mach number in the shock frame, as a consequence of the second law requires

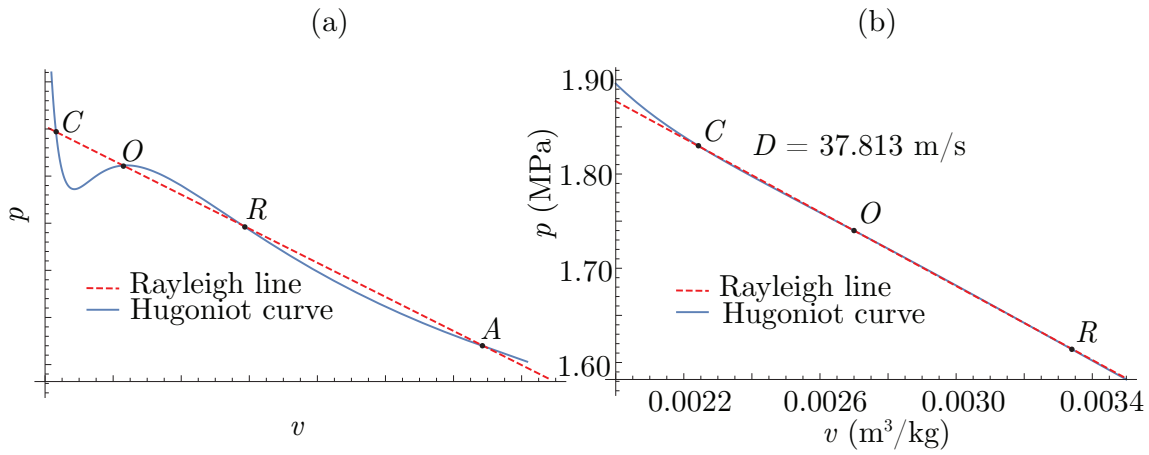

Figure 4.3. Rayleigh line and Hugoniot curve in the non-convex region of state space for PP10 modeled as a van der Waals gas. (a) A sketch with all four intersection points present; features of the curve have been exaggerated for clarity. (b) The region of the points of interest on the analytical curves; A is outside the domain shown.

that an admissible shock induces a transition from supersonic to subsonic regimes. In some cases, multiple roots will satisfy the second law requirements, and to determine if a root is an admissible solution it must be confirmed that the viscous shock profile exists.

First, a discontinuous shock solution in the classical region with convex isentropes is presented, for which the resulting wave is a conventional compression shock. The unshocked state is given by $p_1 = 2.0 \times 10^6$ Pa, $v_1 = 0.0035$ m^3/kg, $T_1 = 733.4885$ K, and $\hat{u}_1 = 69.367$ m/s. Solving Eqs. (2.6, 2.23-2.25) results in four roots, given in Table 4.2. These solutions correspond to the Rayleigh line and Hugoniot curve in Fig. 4.2. Roots I^- and I^+ are imaginary, and root O is the trivial unshocked solution. Root C is the only valid shock jump. This solution is a compression shock, as expected because the flow is in the convex region with fundamental derivative $\mathcal{G} > 0$. The pressure ratio is $p_2/p_1 = 1.115$, and the square of the upstream and downstream Mach numbers are $M_1^2 = 1.115$ and $M_2^2 = 0.889$, respectively. The entropy change is

TABLE 4.2

RANKINE-HUGONIOT JUMP EQUATION SOLUTIONS,

COMPRESSION SHOCK

Root	I^-	I^+	C	O
p_1 (MPa)	2.000	2.000	2.000	2.000
p_2 (MPa)	$2.795 - 0.533i$	$2.795 + 0.533i$	2.230	2.000
v_1 (m^3/kg)	0.00350	0.00350	0.00350	0.00350
v_2 (m^3/kg)	$0.00148 - 0.0014i$	$0.00148 + 0.0014i$	0.00291	0.00350
T_1 (K)	733.488	733.488	733.488	733.488
T_2 (K)	$739.06 - 10.03i$	$739.06 + 10.03i$	735.722	733.488
ρ_1 (kg/m^3)	285.714	285.714	285.714	285.714
ρ_2 (kg/m^3)	$366.937 - 337.53i$	$366.937 + 337.53i$	343.196	285.714
$\hat{u}_2$ (m/s)	$29.257 + 26.912i$	$29.257 - 26.912i$	57.749	69.367
c_2 (m/s)	$35.209 + 57.684i$	$35.209 - 57.684i$	61.227	65.695
$\Delta s/c_v$	$0.00022 + 0.000061i$	$0.00022 - 0.000061i$	3.036×10^{-6}	0

positive, satisfying the second law of thermodynamics. The density profile is given in Fig. 4.4, and the inviscid exact solution is accompanied by the numerical solution for the viscous profile. The end state of the inviscid exact solution was computed using the Rankine-Hugoniot jump equations with the van der Waals equation of state, and the location of the jump was determined using the shock speed and the final time to which the viscous simulation was computed.

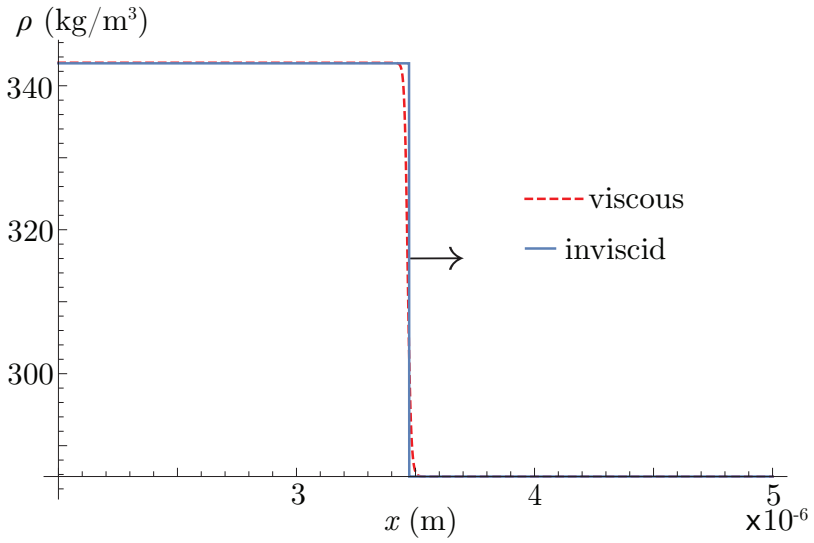

Figure 4.4. Classical compression shock traveling to the right in PP10 modeled as a van der Waals gas. The solid line is the inviscid exact solution, and the dashed line is the viscous numerical solution.

A shock jump solution in the non-convex region is now presented, for which it is expected that the jump be a rarefaction shock, as the fundamental derivative $\mathcal{G}$ is negative. The unshocked state is given by $p_1 = 1.74 \times 10^6$ Pa, $v_1 = 0.0027$ m^3/kg, $T_1 = 656.2255$ K, and $\hat{u}_1 = 37.8129$ m/s. The Rankine-Hugoniot jump analysis yields four roots, given in Table 4.3. These solutions correspond to the Rayleigh line

and Hugoniot curve in Fig. 4.3. Root O is the trivial unshocked solution, and the root A is inadmissible because $\Delta s < 0$. However, both roots C and R have positive entropy jumps. These solutions correspond to a compression and rarefaction shock, respectively, and the correct weak solution cannot be determined by the second law of thermodynamics alone. As detailed by Menikoff and Plohr [83], the second law is not always sufficient to define admissible shock waves, and a more stringent condition dictates that realizable jump solutions must admit viscous profiles.

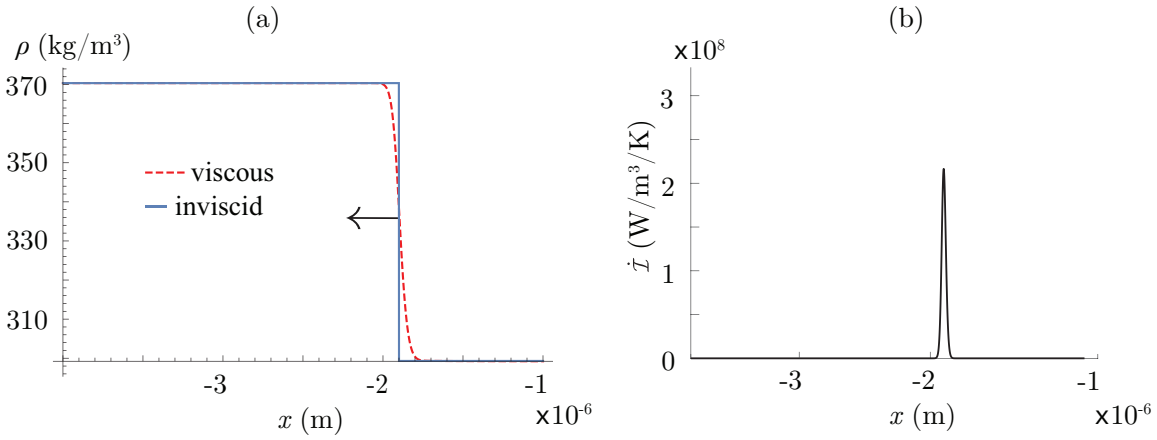

Figure 4.5. Anomalous discontinuous rarefaction shock traveling to the left in PP10 modeled as a van der Waals gas. The solid line is the inviscid exact solution, and the dashed line is the viscous numerical solution. For this case, the viscous profile is necessary to determine that the rarefaction shock is the correct solution, as two roots given in Table 4.3 have increases in entropy that satisfy the second law of thermodynamics.

Because the jump is within the anomalous region, the rarefaction shock described

by the third root is expected to be the correct solution. Using the numerical predictions, the viscous profile corresponding to these initial conditions is confirmed to relax to the solution corresponding to root R. For the corresponding rarefaction shock, the pressure ratio is $p_2/p_1 = 0.927$, and the square of the upstream and downstream Mach numbers are $M_1^2 = 1.038$ and $M_2^2 = 0.984$, respectively. Figure 4.5 shows both the inviscid shock discontinuity predicted by the Rankine-Hugoniot jump conditions, and the corresponding viscous profile, computed with the numerical simulation, that confirms the rarefaction as an admissible shock solution. The anomalous rarefaction shock is expected in this case because the fundamental derivative is negative at the initial state. As the density decreases, the sound speed increases; thus, the characteristic speed at the lower density is faster, driving the wave and forming a shock discontinuity.

TABLE 4.3

RANKINE-HUGONIOT JUMP EQUATION SOLUTIONS,
RAREFACTION SHOCK

Root	C	O	R	A
p_1 (MPa)	1.740	1.740	1.740	1.740
p_2 (MPa)	1.830	1.740	1.614	1.475
v_1 (m^3/kg)	0.0027	0.0027	0.0027	0.0027
v_2 (m^3/kg)	0.00224	0.0027	0.00334	0.00404
T_1 (K)	656.226	656.226	656.226	656.226
T_2 (K)	658.440	656.226	653.867	651.883
ρ_1 (kg/m^3)	370.370	370.370	370.370	370.370
ρ_2 (kg/m^3)	445.847	370.370	299.231	247.330
$\hat{u}_2$ (m/s)	31.476	37.811	46.900	56.742
c_2 (m/s)	33.263	37.107	47.266	55.755
$\Delta s/c_v$	5.694×10^{-7}	0	4.398×10^{-7}	-1.049×10^{-7}

It is expected that the predictions of the unsteady codes should agree with the determination that the rarefaction shock predicted by root R is stable, while the compression shock predicted by root C is unstable. This is tested by initiating the viscous and inviscid codes with the shock jump in the shock frame and allowing time to advance. The rarefaction shock corresponding to root R is stable, and develops in the viscous code as seen in Fig. 4.5. The compression shock predicted by root C however is not stable, and decomposes into a compression fan (as expected of a rarefaction shock in the classical regime). The resulting waves are shown in Fig. 4.6.

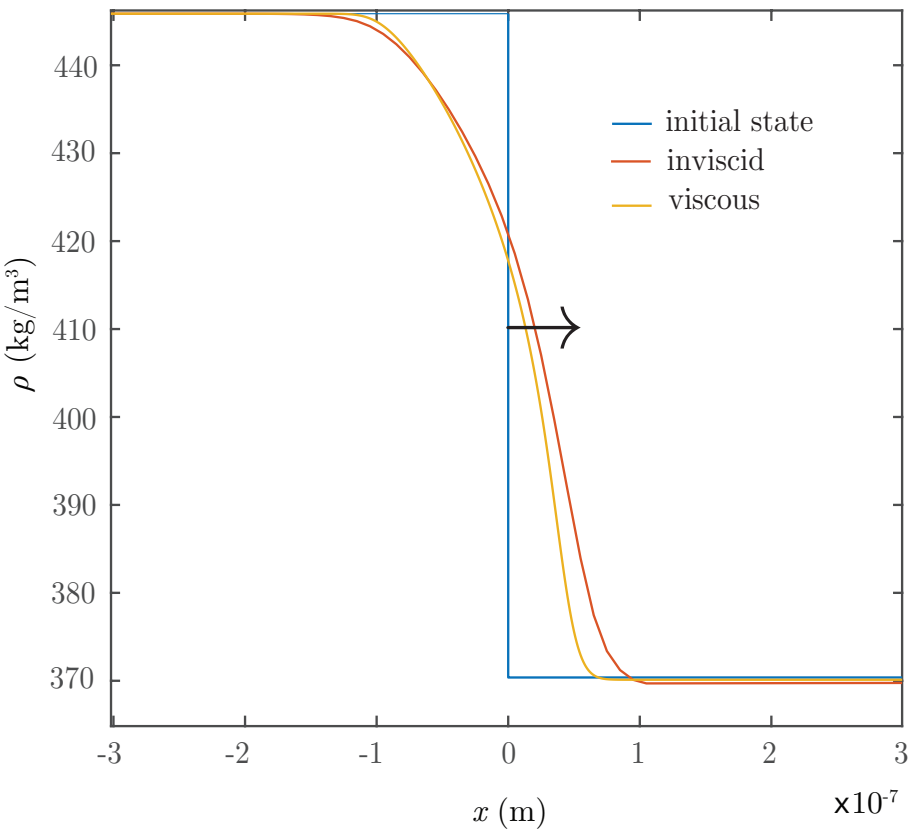

Figure 4.6. When initiated with the compression shock represented by root C in Table 4.3, the unsteady numerical solutions show that this shock is not stable, and instead decomposes into a continuous compression.

CHAPTER 5

UNSTEADY INERT WAVE DYNAMICS

In this chapter analysis of unsteady inert anomalous wave dynamics is presented. An exact solution for homeoentropic waves is applied to both classical and anomalous cases. A similar solution procedure was first presented by Quartapelle, et al. [100] for classical homeoentropic rarefaction fans. This is followed by shock tube solutions with initial conditions in fully convex, non-convex, and mixed convexity regions. In the mixed convexity shock tube, a composite compression wave is present, an unusual type of anomalous wave for which a homeoentropic fan and a discontinuity travel together. Jump discontinuity analysis and homeoentropic analysis are combined for analysis of composite waves, as described by Cramer [32]. This chapter is concluded with solution verification of the numerical methods with the shock tube solutions. All examples in this chapter use the parameters for PP10 given in Table 4.1.

5.1 Continuous Waves

Exact solutions for isentropic waves in a van der Waals gas were first presented by Quartapelle, et al. [100], who calculated solutions for classical isentropic rarefaction fans. The exact solution used here is similar, and is presented as a specialization of the general method presented by von Mises [121] and Courant and Friedrichs [30], both of whom only provided specific solutions for the ideal gas equation of state. It has been formulated in such a way that it is valid for classical rarefaction fans as well as anomalous compression fans.

The solution is obtained by beginning with the non-conservative form of the inert inviscid governing equations, given in Eqs. (2.27-2.29). Reducing the system to the inert equations and rewriting the energy equation in terms of entropy yields:

$$\begin{aligned} \frac{\partial \rho}{\partial t} + u\frac{\partial \rho}{\partial x} + \rho\frac{\partial u}{\partial x} &= 0, & (5.1)\\ \rho\frac{\partial u}{\partial t} + \rho u\frac{\partial u}{\partial x} + \frac{\partial p}{\partial x} &= 0, & (5.2)\\ \frac{\partial s}{\partial t} + u\frac{\partial s}{\partial x} &= 0, & (5.3)\\ p = p(\rho, s). & & (5.4) \end{aligned}$$

Additionally, we will require the flow to satisfy the homeoentropic assumption. Under this assumption, entropy is constant throughout the flow, including across continuous waves, both compressions and rarefactions. This assumption reduces the system to three equations, mass conservation, momentum conservation, and the equation of state, because s is a known constant. Additionally, the equation of state is now $p = p(\rho)$, and the sound speed can be taken to be a function of one thermodynamic varialbe: $c = c(\rho)$.

We next seek the characteristic form of the differential equations. Details of employing the method of characteristics on Eqs. (5.1-5.2) can be found in [30], [96], and [121]. This analysis yields two characteristic equations with two characteristic speeds, given here as:

$$c^2\frac{\mathrm{d}\rho}{\mathrm{d}t} \pm \rho c\frac{\mathrm{d}u}{\mathrm{d}t} = 0, \quad \text{on} \quad \frac{\mathrm{d}x}{\mathrm{d}t} = u \pm c. \tag{5.5}$$

Rearranging and integrating, the characteristic equations are now written in the form

of Courant and Friedrichs [30] as:

$$u + \ell(\rho) = 2\mathsf{r}(\hat{B}), \quad \text{on} \quad \frac{\mathrm{d}x}{\mathrm{d}t} = u + c, \tag{5.6}$$

$$u - \ell(\rho) = -2\mathsf{s}(\hat{A}), \quad \text{on} \quad \frac{\mathrm{d}x}{\mathrm{d}t} = u - c. \tag{5.7}$$

In Eqs. (5.6) and (5.7), $\mathsf{r}(\hat{B})$ and $\mathsf{s}(\hat{A})$ are arbitrary functions called Riemann invariants. The quantity $\ell(\rho)$ is given by

$$\ell(\rho) = \int_{\rho'}^{\rho} \frac{c(\hat{\rho})}{\hat{\rho}} \, \mathrm{d}\hat{\rho}, \tag{5.8}$$

where the lower bound of integration, ρ', is an arbitrary constant. Equations (5.6) and (5.7) are the acoustic characteristics of the system.

For a simple homeoentropic wave, either $\mathsf{r}(\hat{B})$ (backward facing, $u+c$ characteristics are straight lines) or $\mathsf{s}(\hat{A})$ (forward facing, $u-c$ characteristics are straight lines) is constant in all of $x-t$ space. Equations (5.6) and (5.7) then become

$$u + \ell(\rho) = 2\mathsf{r}_o, \qquad u - \ell(\rho) = -2\mathsf{s}(\hat{A}), \tag{5.9a,b}$$

for a backward facing wave, or

$$u + \ell(\rho) = 2\mathsf{r}(\hat{B}), \qquad u - \ell(\rho) = -2\mathsf{s}_o, \tag{5.10a,b}$$

for a forward facing wave. The subscript o now appears with the Riemann invariant that is constant for all x and t, as its value can be evaluated at the initial state because it will not change across the wave. As in [30], the constant Riemann invariants are given by $2\mathsf{r}_o = u_o + \ell(\rho_o)$ or $-2\mathsf{s}_o = u_o - \ell(\rho_o)$ for a backward and forward facing

wave, respectively. Combining these with Eqs. (5.9) and (5.10), we can now write

$$u \pm \ell(\rho) = u_o \pm \ell(\rho_o), \tag{5.11}$$

where the plus describes a backward facing wave, and the minus a forward facing wave.

Substituting the definition of ℓ, Eq. (5.8), into Eq. (5.11), and noting that the arbitrary lower bound ρ' is chosen to be the initial density ρ_o, this becomes

$$u = u_o \mp \int_{\rho_o}^{\rho} \frac{c(\hat{\rho})}{\hat{\rho}} \, \mathrm{d}\hat{\rho}, \tag{5.12}$$

for the backward and forward waves, respectively. Additionally, the initial particle velocity in the laboratory frame u_o is often zero, and if so, the term drops out. If the integral in $\ell(\rho)$ can be determined analytically (as is the case for the ideal gas), the solution procedure of Courant and Friedrichs [30] can be followed directly. However, for the van der Waals equation of state, the homeoentropic sound speed, calculated from $p = p(\rho)$, is given by

$$c(\rho) = \sqrt{-2a\rho + \frac{c_o(1 + R/c_v)(1/\rho - b)^{(-R/c_v - 2)}}{\rho^2}}, \tag{5.13}$$

where the constant $c_o = (p_o + a\rho_o^2)(1/\rho_o - b)^{R/c_v + 1}$ is determined by the initial state. Substituting Eq. (5.13) into (5.8), the integral cannot be computed analytically, and a numerical quadrature is required. Denoting the velocity change across the wave as u_p, varying from 0 to a maximum value u_{pmax}, a solution for $\rho(u_p)$ is available from numerical quadrature. The corresponding characteristic speeds can then be written as

$$\frac{\mathrm{d}x}{\mathrm{d}t} = u_p \pm c(\rho(u_p)). \tag{5.14}$$

Straightforward separation of variables and integration gives functional forms of the straight characteristics, which may then be used to plot wave profiles. The slope of the characteristics is determined by $u_p \pm c(\rho(u_p))$. Isentropic relations for the van der Waals equation of state can be used to find the solutions for other quantities, including the temperature

$$\frac{T_2}{T_1} = \left(\frac{v_2 - b}{v_1 - b}\right)^{-R/c_v}, \tag{5.15}$$

and pressure

$$p_2 = \left(p_1 + \frac{a}{v_1^2}\right)\left(\frac{v_2 - b}{v_1 - b}\right)^{-\frac{R}{c_v}-1} - \frac{a}{v_2^2}. \tag{5.16}$$

This solution procedure is now utilized for homeoentropic waves in an inviscid van der Waals gas, starting with the solution for a classical homeoentropic rarefaction fan. The initial conditions for the fan are $p_o = 2.23 \times 10^6$ Pa, $\rho_o = 370.11$ kg/m^3, and the final particle velocity is $u_{pmax} = 11.62$ m/s. These initial conditions are in the region of state space where the fundamental derivative $\mathcal{G}$ is positive, and classical variations of sound speed with density are expected. Figure 5.1(a) shows the solution for this wave in the density, and Fig. 5.1(b) gives the sound speed across the fan. As expected because the fundamental derivative is positive, isentropes are convex, and the sound speed decreases with decreasing density and pressure. The slopes of the corresponding characteristics diverge, and they spread to form a fan, and are shown in Fig. 5.2. Following from the solution presented, the characteristic speeds for a backward facing rarefaction fan are $u_p - c(\rho(u_p))$, and the characteristics shown are plotted with $t = x/(u_p - c(\rho(u_p)))$. The magnitude of $u_p - c(\rho(u_p))$ decreases and the slope of the characteristics increases; thus, the characteristics diverge.

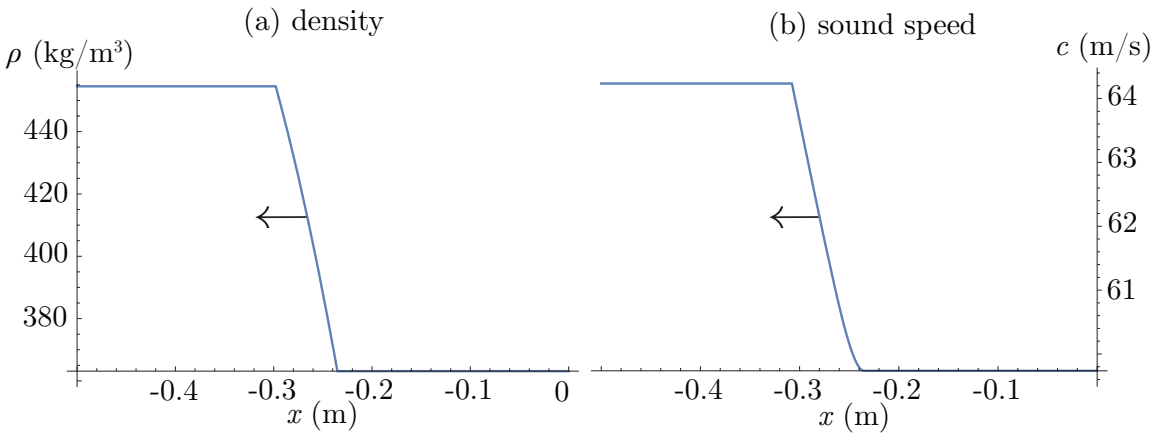

Figure 5.1. Classical homeoentropic rarefaction fan in PP10 modeled as a van der Waals gas, showing (a) the density profile and (b) the sound speed across the wave.

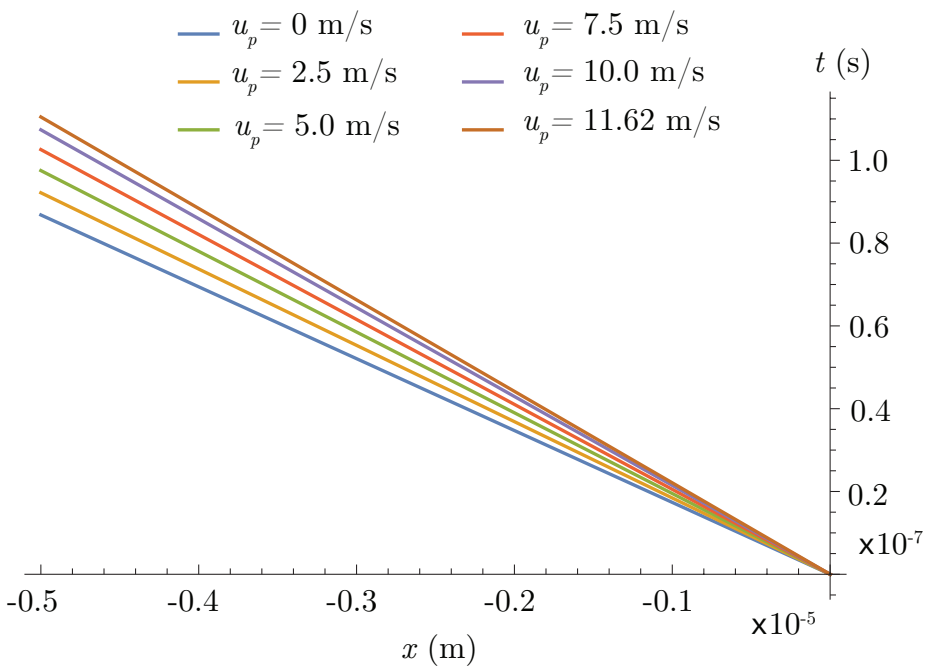

Figure 5.2. Characteristics of a classical backward facing homeoentropic rarefaction fan in PP10 modeled as a van der Waals gas.

The initial conditions for the homeoentropic wave are now placed within the anomalous region at $p_o = 1.614 \times 10^6$ Pa, $\rho_o = 359.543$ kg/m^3, and a final particle velocity of $\hat{u}_{pmax} = 9$ m/s. At the initial state, the fundamental derivative $\mathcal{G}$ is negative. Because the initial conditions are within the anomalous region, isentropes are non-convex, and compression waves are no longer expected to form as discontinuous shocks, but as continuous homeoentropic waves. The initial conditions correspond to the full solutions in Figs. 5.3(a) and (b) for the density and sound speed, respectively. As the density is increased by the compression, the sound speed is decreased, as expected for flow in the anomalous region. The resulting fan remains stable as the leading edge continues to travel faster than the trailing edge, instead of collapsing into a discontinuity if the sound speed were increasing. The characteristics are

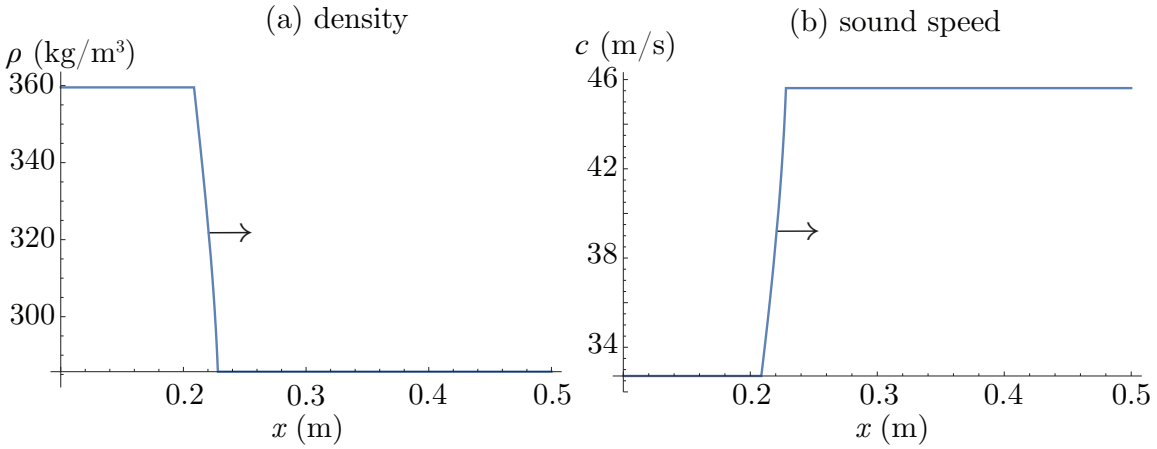

Figure 5.3. An anomalous homeoentropic compression fan in PP10 modeled as a van der Waals gas, where (a) is the density profile and (b) is the sound speed across the wave.

shown in Fig. 5.4. The characteristic speeds for a forward facing compression fan are $u_p + c(\rho(u_p))$, and the characteristics shown are plotted with $t = x/(u_p + c(\rho(u_p)))$. As the magnitude of $(u_p + c(\rho(u_p)))$ decreases with decreasing sound speed, the slope of the characteristics increases, and they diverge. If the sound speed were increasing, the slope would decrease and the characteristics would cross as for classical compression shock.

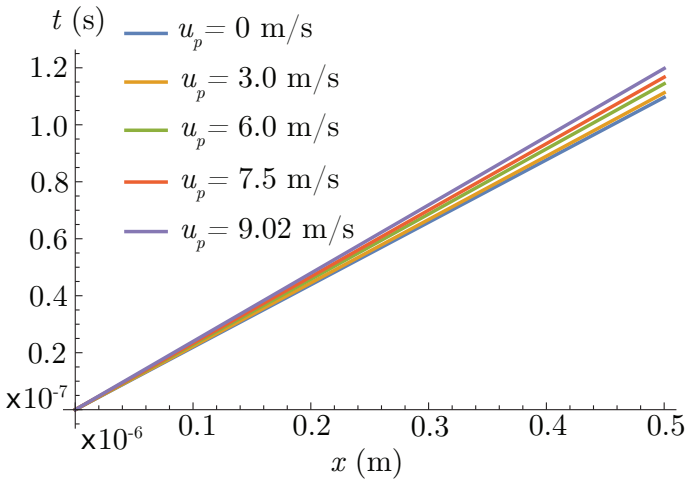

Figure 5.4. Characteristics of an anomalous forward facing homeoentropic compression fan in PP10 modeled as a van der Waals gas.

5.2 Shock Tubes

The Riemann problem of the Sod shock tube is a stringent test of numerical methods as it exercises performance with continuous waves, discontinuous shocks, and contact discontinuities [114]. As discussed in Chapter 2, the initial conditions of the shock tube entail left and right initial states separated by a contact discontinuity, illustrated in Fig. 2.1(a). When the initial contact discontinuity is released, three waves develop in the flow. Fig. 5.5 is a sketch of the $x - t$ diagrams for shock tubes in the convex region, 5.5a, and in the non-convex region, 5.5b. The classical shock tube exhibits a rarefaction fan, contact discontinuity, and compression shock, while the anomalous shock tube results in a rarefaction shock, contact discontinuity, and compression fan.

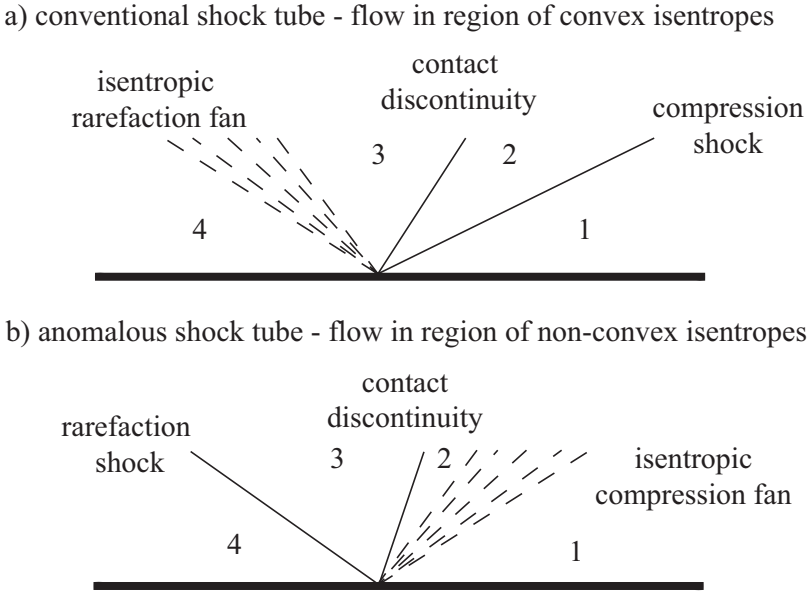

Figure 5.5. Sketch of $x - t$ diagrams for two Sod shock tube problems; a) Fully convex shock tube with conventional rarefaction fan and compression shock; b) Fully non-convex shock tube with anomalous rarefaction shock and compression fan.

Exact and numerical solutions for Sod shock tubes, in both the classical and anomalous regions, with inviscid and viscous van der Waals gases will be used in verification exercises. Analytic solutions of inviscid shock tubes are constructed by connecting discontinuous shock solutions, discussed in Section 4.6, and homeoentropic wave solutions from Section 5.1, with contact discontinuities. Contact discontinuities are the result of particles in two different states, in either the same or different materials, traveling at the same speed. Solutions for contact discontinuities are found by requiring that the particle velocity and pressure do not change across the wave, $u_1 = u_2$ and $p_1 = p_2$. Additionally, the wave speed of a contact discontinuity is equal to the particle velocity, so $D_{cd} = u_1 = u_2$. The density jump across the contact discontinuity is prescribed, and the temperature change is computed using the equation of state.

Table 5.1 gives the pressure and density in each of the four corresponding regions for the traditional convex and anomalous non-convex cases that have been used in example calculations. These values have been calculated using the material parameters for PP10 given in Table 4.1. The viscous shock tube solutions have been performed with the numerical method described in Section 3.3. For the inviscid shock tube, the already-discussed analytical solutions for discontinuous shocks and continuous homeoentropic fans are connected by a contact discontinuity. Table 5.1 gives the values for each of the four regions for both the shock tube with flow in the convex and non-convex regions; these values are the same for both the viscous and inviscid cases, and it is the wave structure that changes.

First, a shock tube with a van der Waals gas entirely within the classical region where isentropes are convex is examined. The initial conditions are given by regions 1 and 4 in Table 5.1 and shown in Fig. 5.6. The exact inviscid solution, along with the numerical viscous solution, were computed at $t = 5 \times 10^{-8}$ s. Figure 5.7 is a plot of the density for both the inviscid and viscous cases. A rarefaction fan moves to

TABLE 5.1

DENSITY AND PRESSURE VALUES, SOD SHOCK TUBES

Convexity	p_1 (MPa)	p_2 (MPa)	p_3 (MPa)	p_4 (MPa)
Convex	2.000	2.230	2.230	2.500
Non-Convex	1.500	1.614	1.614	1.740
Convexity	ρ_1 (kg/m^3)	ρ_2 (kg/m^3)	ρ_3 (kg/m^3)	ρ_4 (kg/m^3)
Convex	285.714	343.196	370.110	454.545
Non-Convex	285.714	359.543	299.231	370.37

the left, a contact discontinuity to the right, and a compression shock to the right as well, all classical waves that are expected to form if the fundamental derivative is positive. In addition to the density profile, the dimensionless entropy of the shock wave and irreversibility production rate for the viscous case are plotted in Fig. 5.8. The irreversibility production rate is positive throughout the flow, with the largest spike located at the shock front. Additionally, the irreversibility production rate has a larger spike at the compression shock than at the rarefaction fan. Entropy, which has been plotted for the viscous case to highlight the additional features in the viscous limit, increases overall across the shock wave with a local maximum attributed to reversible heat transfer. It is also seen in Fig. 5.8 that the magnitude of the dimensionless entropy increase across the shock is very small, as is typical of the relatively weak shocks in BZT fluids.

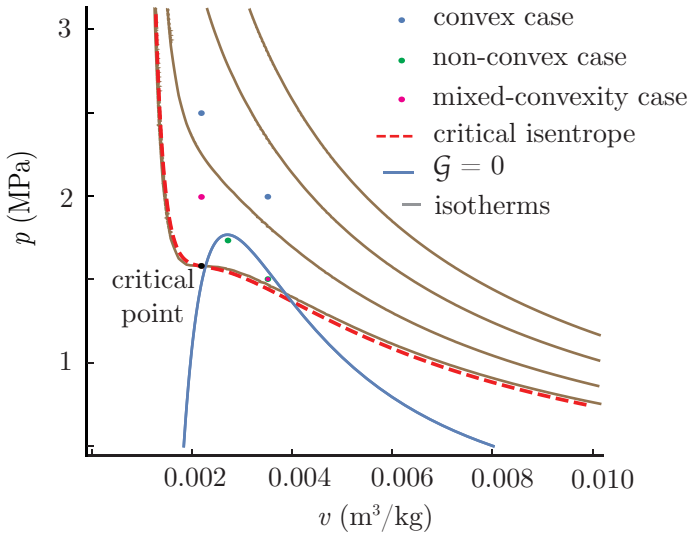

Figure 5.6. $p - v$ space for PP10 modeled as a van der Waals gas. Initial conditions for three shock tube cases are provided: fully-convex, non-convex, and mixed convexity.

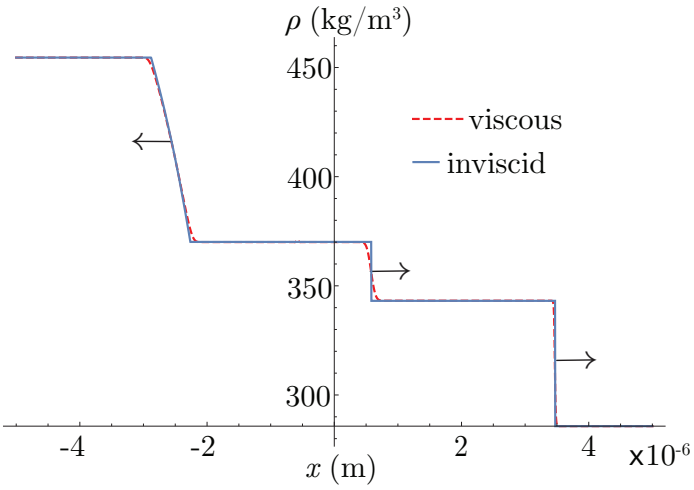

Figure 5.7. Classical shock tube solution with PP10 modeled as a van der Waals gas. The initial conditions have been placed entirely within the classical region of state space where isentropes are strictly convex. The resulting waves are a left traveling rarefaction fan, a right traveling contact discontinuity, and a right traveling discontinuous compression shock.

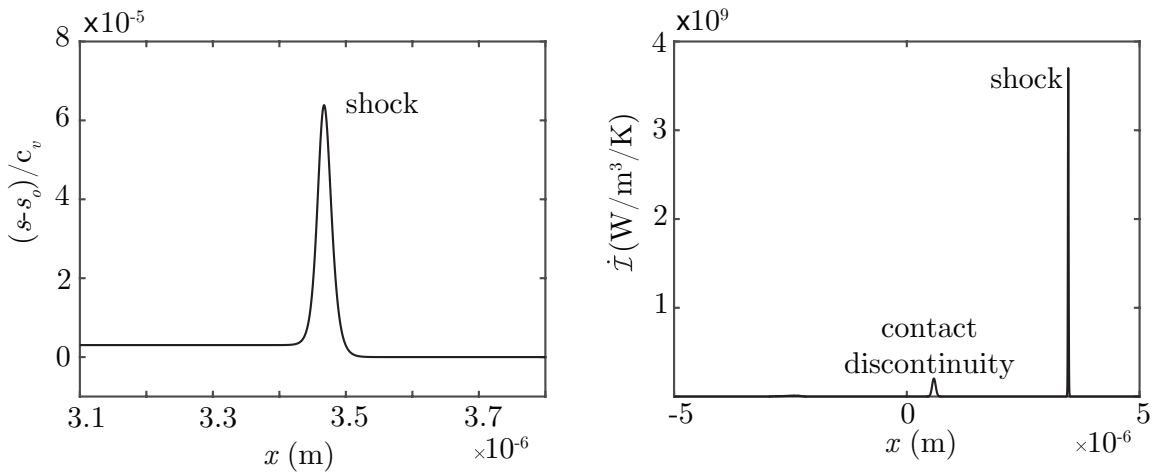

Figure 5.8. Viscous shock tube in the classical region with a van der Waals gas. Entropy across the viscous shock wave has a local maximum and an overall increase that satisfies the second law. The irreversibility production rate is largest across the shock.

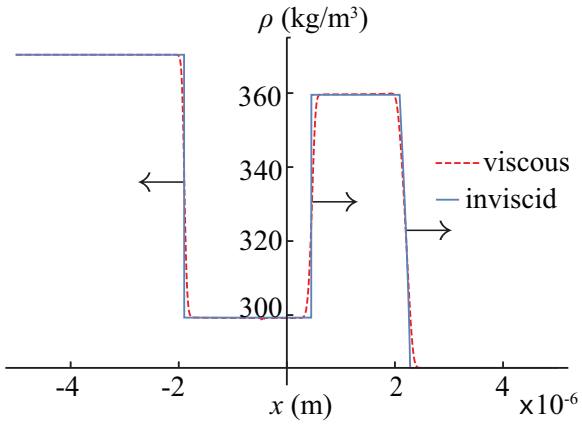

Figure 5.9. Anomalous shock tube with initial conditions in the anomalous region of PP10 modeled as a van der Waals gas. The resulting waves are a left traveling discontinuous rarefaction, a right traveling contact discontinuity, and a right traveling continuous compression fan.

The initial conditions for the shock tube with a van der Waals gas are now placed entirely within the anomalous region, where isentropes are non-convex. The density profile for the viscous numerical solution and inviscid exact solution are shown in Fig. 5.9. The waves that now form are a right moving contact discontinuity separating a left moving rarefaction shock and a right moving compression fan, anomalous waves that are expected because the fundamental derivative is negative throughout the flow. Correspondingly, the relationship between sound speed and density is reversed, and the anomalous waves form. Plots of the entropy and irreversibility production rate for the viscous solution are shown in Fig. 5.10 Across the rarefaction shock wave, the dimensionless entropy of the viscous wave possesses a local minimum, but overall, entropy increases across the shock wave, satisfying the second-law. The irreversibility production rate remains positive across the domain, with the largest spike present at the contact discontinuity, which has no predicted behavior difference from the

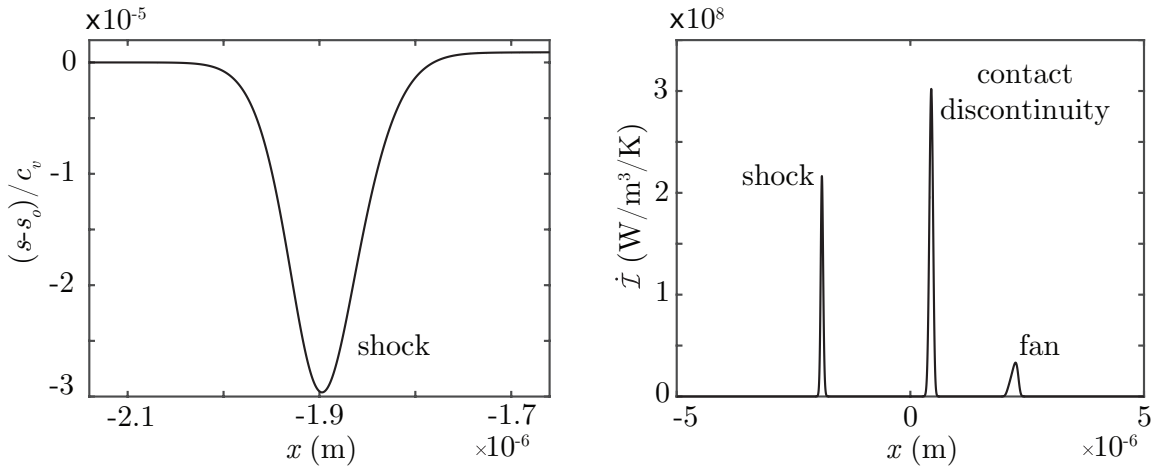

Figure 5.10. Viscous shock tube with initial conditions in the anomalous region of PP10 modeled as a van der Waals gas. The entropy across the shock has a local minimum but an overall increase. The largest spike in the irreversibility production rate is at the contact discontinuity.

classical case. Additionally, the spike in $\dot{\mathcal{I}}$ at the rarefaction shock is larger than at the compression fan, mirroring the behavior in the classical case.

Numerical simulations were utilized to compute solutions of the case when the initial flow field spans the convex and non-convex regions. The initial conditions for the mixed convexity case are shown in the $p - v$ plane in Fig. 5.6. In this case, the state variables of the flow cross the $\mathcal{G} = 0$ curve; thus, a combination of classical and anomalous behavior of the speed of sound as it relates to the state variables is expected. The solutions in the density, fundamental derivative, and speed of sound are given for both the viscous and inviscid cases in Figs. 5.11 and 5.12(a) and (b). Additionally, the dimensionless entropy of the shock wave and irreversibility production rate for the viscous case are shown in 5.12(c) and (d).

As with the classical and anomalous shock tube solutions, the mixed convexity case has a left traveling rarefaction and a right traveling compression separated by a contact discontinuity. The rarefaction, moving into the initial region of the flow with

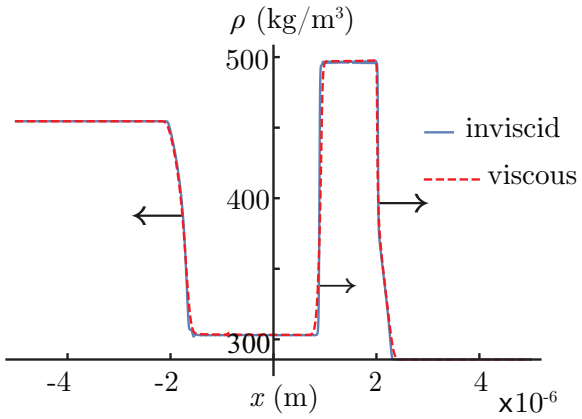

Figure 5.11. Shock tube with mixed convexity initial conditions in PP10 modeled as a van der Waals gas. A contact discontinuity separates a classical rarefaction fan traveling to the left and an anomalous composite compression traveling to the right.

convex isentropes, is a rarefaction fan, as in the classical shock tube. The compression however is moving into the anomalous region, and the fundamental derivative crosses $\mathcal{G} = 0$ within the shock structure. As a result, the speed of sound's relation to the state variables reverses at an intermediate point in the wave form. This causes a composite shock characterized by an anomalous compression fan followed by a compression shock. As this composite wave travels, the leading edge of the compression fan is the fastest, and the shock discontinuity travels with the same wave speed as the trailing edge of the fan. This is clear when focusing on the sound speed at the transition as in Fig 5.13, as the speed of sound's behavior is non-monotonic, demonstrating a decrease followed by an increase within the compression wave. The overall entropy of the viscous shock increases across the split-shock structure, and the irreversibility production rate consists of a small increase within the continuous structure followed by a larger spike at the shock. The largest irreversibility production rate spike occurs at the shock, followed by the contact discontinuity and the rarefaction fan.

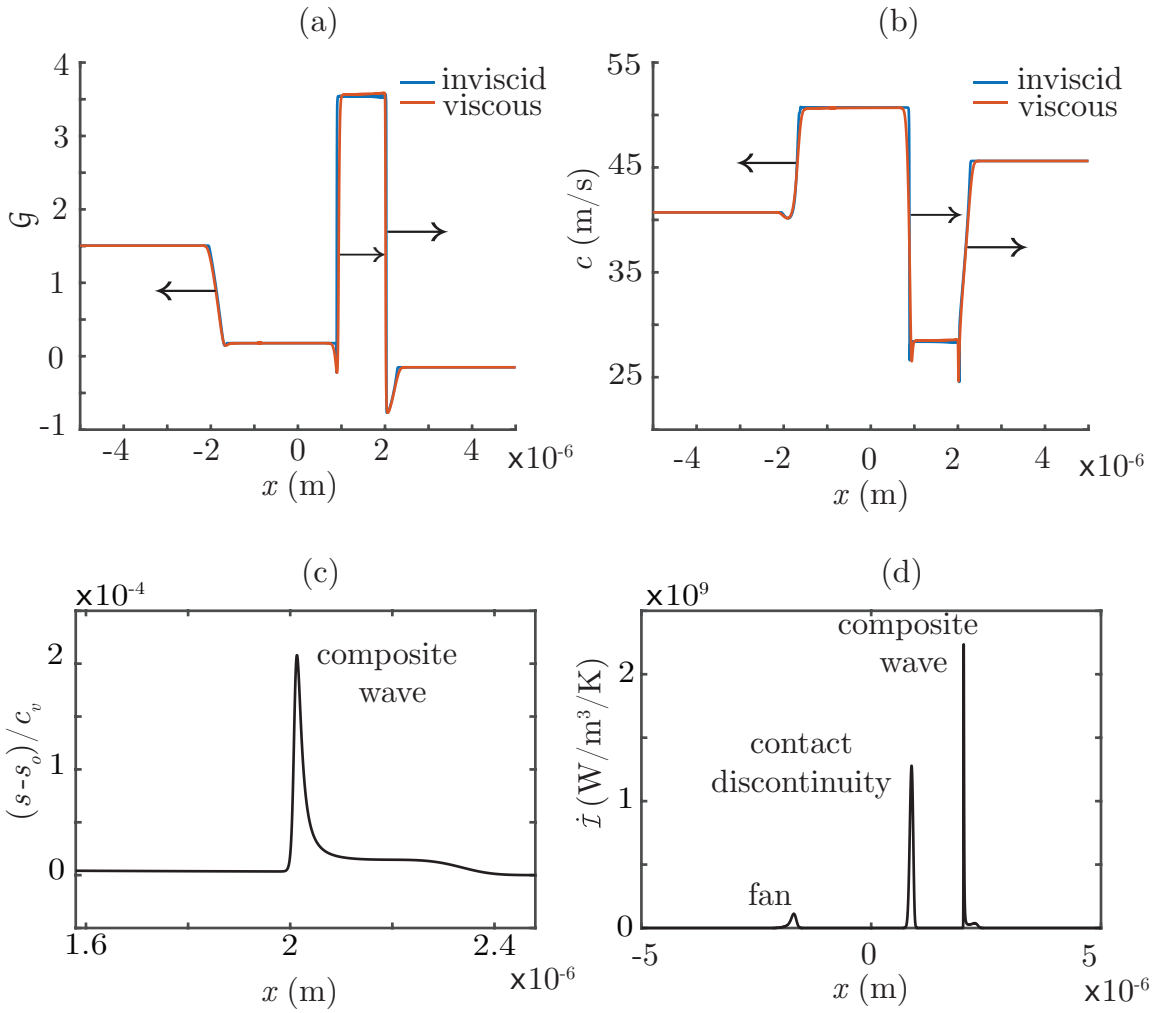

Figure 5.12. Shock tube with mixed convexity initial conditions in PP10 modeled as a van der Waals gas. (a) The fundamental derivative changes sign across the composite wave. (b) The sound speed is non-monotonic across the composite wave. (c) Total entropy across the composite compression increases. (d) The largest spike in the irreversibility production rate is at the composite wave.

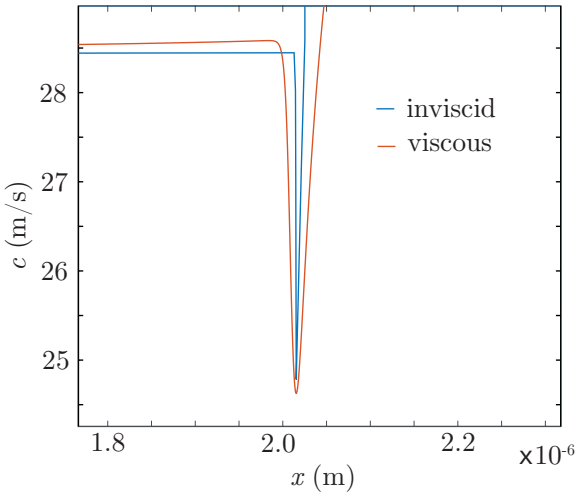

Figure 5.13. Transition from decreasing to increasing sound speed in an anomalous composite compression wave in PP10 modeled as a van der Waals gas.

5.3 Composite Shocks

The composite shock that arises from the mixed convexity shock tube fits neither the jump discontinuity analysis from Chapter 4 nor the homeoentropic solution of Section 5.1. Combination of these two solution procedures provides useful understanding of the composite wave structure. Much of this analysis is based on that of Cramer [32] and Menikoff and Plohr [83], and additional details can be found there.

This analysis starts with the Hugoniot curve originating at the initial state of the composite wave in Fig. 5.11, and the Rayleigh line that passes through the p-v state at which the composite wave undergoes a transition from continuous to discontinuous; this is shown in Fig. 5.14. There are four intersection points, and the corresponding Rankine-Hugoniot jump equation solutions are given in Table 5.2. The initial state is at O and corresponds to the unshocked solution. The root to the right at R represents a rarefaction shock, which in this case is not physical because the entropy jump is negative. The first root to the left of the initial state at point I is also nonphysical

due to a negative jump in the entropy. This leaves only the root at C with a positive jump in entropy to satisfy the second law. However, the final state at C is also not a valid solution, as Cramer [32] determined that if there are intermediate intersection points no dissipative structure exists. Therefore, a shock jump between O and C is not valid, as the intersection point at I indicates that there is no viscous solution for this jump.

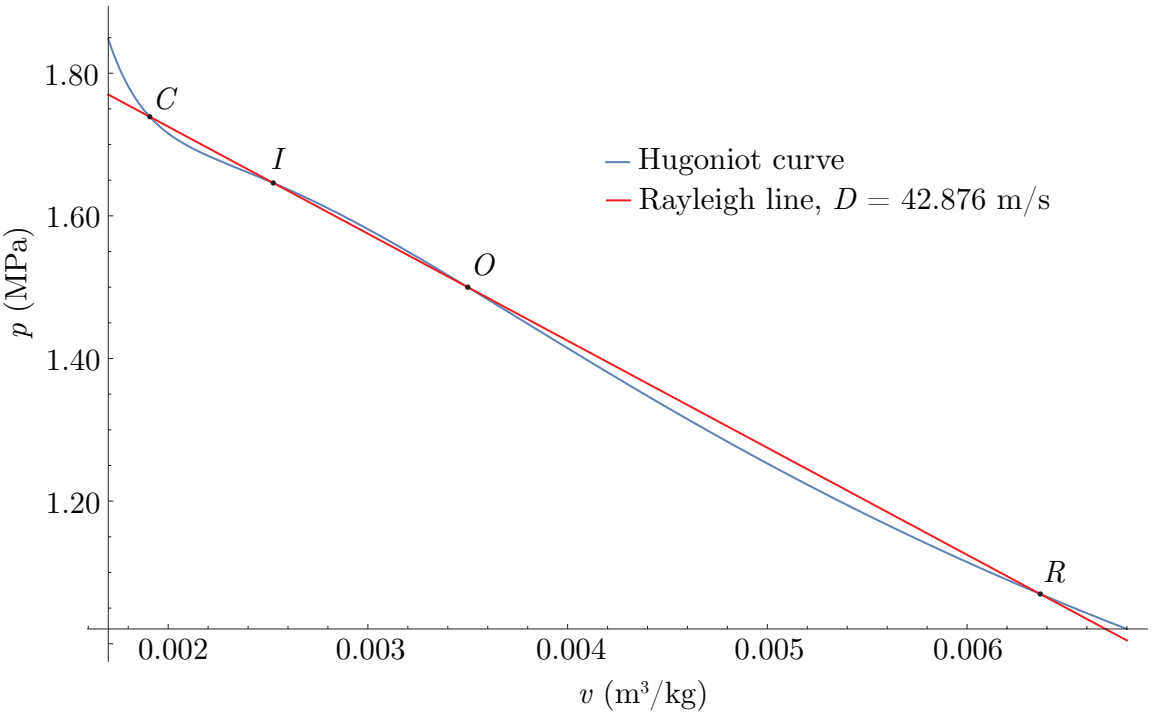

Figure 5.14. Hugoniot curve from the initial condition of the composite wave in the mixed convexity shock tube. The Rayleigh line intersects with the Hugoniot curve at four points.

A consequence of the second law of thermodynamics' requirement of increasing

TABLE 5.2

RANKINE-HUGONIOT JUMP EQUATION SOLUTIONS, MIXED CONVEXITY HUGONIOT CURVE

Root	R	O	I	C
p_1 (MPa)	1.500	1.500	1.500	1500
p_2 (MPa)	1.070	1.500	1.646	1.739
v_1 (m^3/kg)	0.00350	0.00350	0.00350	0.00350
v_2 (m^3/kg)	0.00636	0.00350	0.00252	0.00191
ρ_1 (kg/m^3)	285.000	285.000	285.000	285.000
ρ_2 (kg/m^3)	157.061	285.000	395.868	524.198
$\hat{u}_2$ (m/s)	77.997	42.876	30.946	23.369
c (m/s)	69.059	45.610	27.636	33.267
M	1.129	0.940	1.120	0.702
$\Delta s/c_v$	-5.674×10^{-5}	0	-5.525×10^{-6}	8.009×10^{-7}

entropy across a shock, the shock the shock must induce a transition from supersonic to subsonic flow, corresponding to the Mach number in the shock frame undergoing a transition from $M > 1$ to $M < 1$. The particle velocity, sound speed, and Mach number at each intersection point in Fig. 5.14 are given in Table 5.2. It is immediately apparent that for a wave speed of $D = 42.876$ m/s that no single shock discontinuity will undergo a transition from supersonic to subsonic regimes as the Mach number at the initial state O is subsonic at $M_O = 0.940$. The sound speed at this point is $c_O = 45.610$; therefore admissible shock solutions will not be achievable for shock speeds less than this value. Additionally, the sound speed speed at point O is greater than at C, which in turn is greater than the intermediate intersection point I. This non-monotonic behavior of the sound speed is characteristic of the anomalous region. This consideration of the Mach number is useful in identifying the potential for composite waves.

The structure of the composite wave is a continuous homeoentropic compression followed by a discontinuous compression shock. The wave that begins at the initial state is a homeoentropic compression, so the isentrope is expected to lead to the state at which the compression fan ends. This is illustrated in Fig. 5.15 by the isentrope connecting the initial state at O and the end state of the homeoentropic wave at I. The Hugoniot curve must be calculated from the state I, the initial state of the shock discontinuity. The wave speed of the discontinuity is equal to the speed of the tail end of the homeoentropic wave, and the corresponding Rayleigh line intersects with the Hugoniot curve at the point S. This point is the final state of the composite wave. The state variables at points O, I, and S are in Table 5.3, and agree with the numerical predictions shown in Fig. 5.11.

Returning to the discussion of the Mach number in the composite wave, this analysis is based on Menikoff and Plohr's [83] discussion of anomalous wave structures resulting from mixed-convexity Hugoniot curves. The change in sign of the funda-

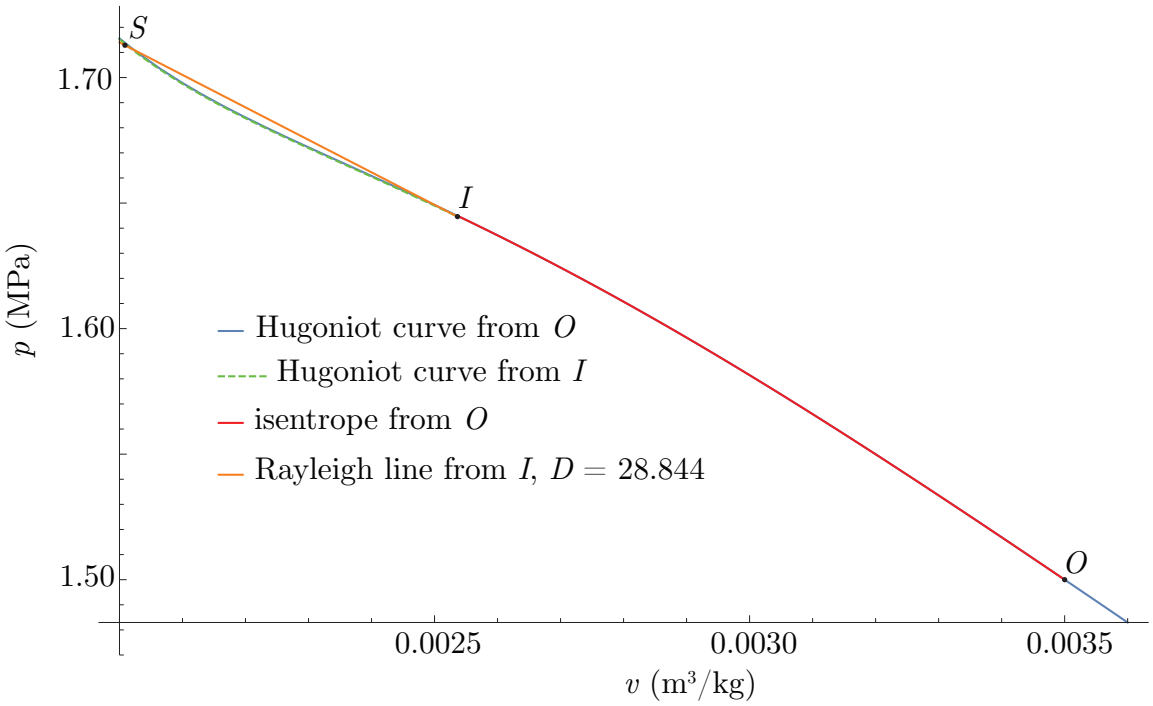

Figure 5.15. The path through p-v space for a composite wave in PP10 modeled as a van der Waals gas. From the initial state O, the compression follows the isentrope to I. The Hugoniot curve is calculated from I, and the Rayleigh line is calculated with the shock speed at the end of the compression fan.

mental derivative $\mathcal{G}$ dictates the transition point from continuous to discontinuous wave. For the composite wave in this example, the Mach number is found in the frame of the shock discontinuity and given in Table 5.3. At the initial state O the Mach number is subsonic, at the transition point where the fan ends the Mach number is supersonic, and behind the shock discontinuity it returns to subsonic. It is possible to have $\mathcal{G} = 0$ at a sonic point, in which case the Hugoniot curve is tangent to an isentrope, the Rayleigh line is tangent to the Hugoniot curve, and entropy is expected to have an inflection point.

TABLE 5.3

COMPOSITE WAVE

Root	O	I	S
p_2 (MPa)	1.500	1.644	1.712
v_2 (m^3/kg)	0.00350	0.00257	0.00191
ρ_2 (kg/m^3)	285.000	394.259	497.846
M	0.632	1.045	0.799

5.4 Verification of the Numerical Method

To test the inviscid exact solution as a tool for verification, it was used as the baseline for a convergence study with the WENO5M method. This was done with the convex shock tube solution for a van der Waals gas, supplemented with both the global and local Lax-Friedrichs flux-splitting schemes; the example material from previous sections, PP10, was used. The inviscid problem is scale invariant, having no maximum length scale requirements imposed by the physics of the problem, and so the domain length was chosen to be $L = 1$ m. A simple normalized $\mathcal{L}_1$ norm of the density error was computed using

$$\mathcal{L}_1 = \frac{1}{N_{grid}} \sum_{i=1}^{N_{\text{grid}}} \frac{|\rho_{x_i} - \rho_i|}{\rho_{x_i}}, \tag{5.17}$$

where the subscript i denotes the index in the numerical solution, x_i indicates the value of the exact solution at the value of x corresponding to index i, and N_{grid} is the total number of points on the grid. Here $\mathcal{L}_1$ represents the average relative error in density throughout the domain. A curve fit was done with the method of least squares. The resulting dimensionless plot of the error versus Δx is given in Fig. 5.16. For both cases, the slope of the convergence is given by the value of r, and is less than one, as is expected with shock-capturing even for a fifth order method due to the presence of discontinuities. Although both methods provide the expected convergence, the global Lax-Friedrichs flux-splitting method has a slight advantage over the local method. We also predict that the numerical solution converges to the exact while comparing plots of the density with decreasing values of Δx, as shown in Fig. 5.17. This figure was produced using the exact solution in the non-convex region and the WENO5M method with global Lax-Friedrichs flux-splitting. The visual convergence of the numerical simulation with the exact solution is apparent here.

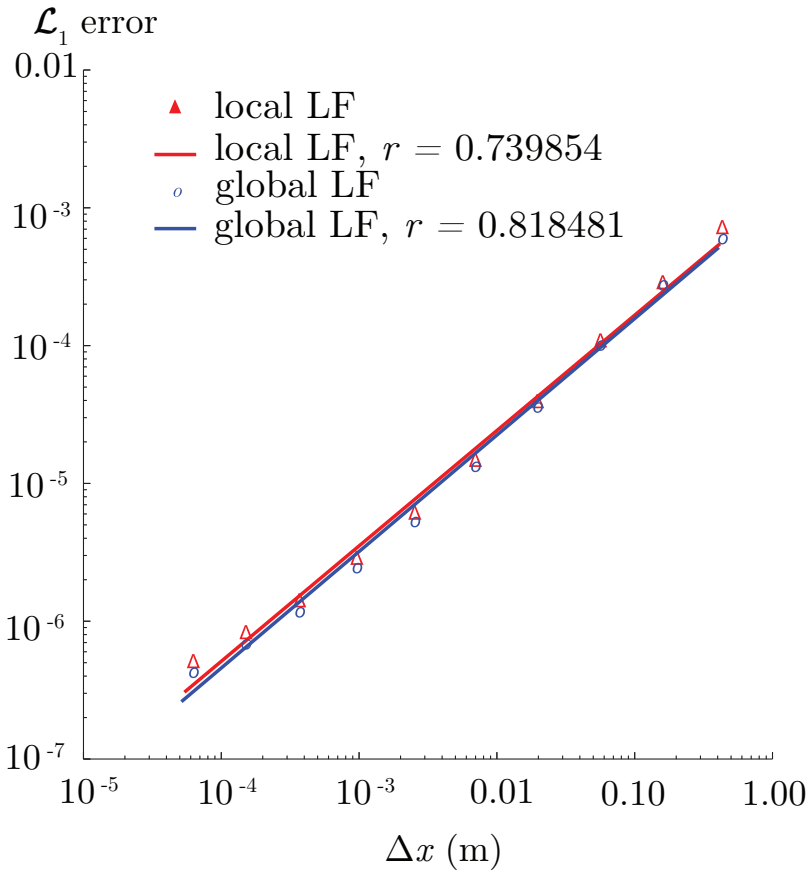

Figure 5.16. Convergence of the normalized $\mathcal{L}_1$ error of density compared to the exact solution of a convex region shock tube with a van der Waals gas. The curve fit was done with the method of least squares, and its slope is given by the value of r.

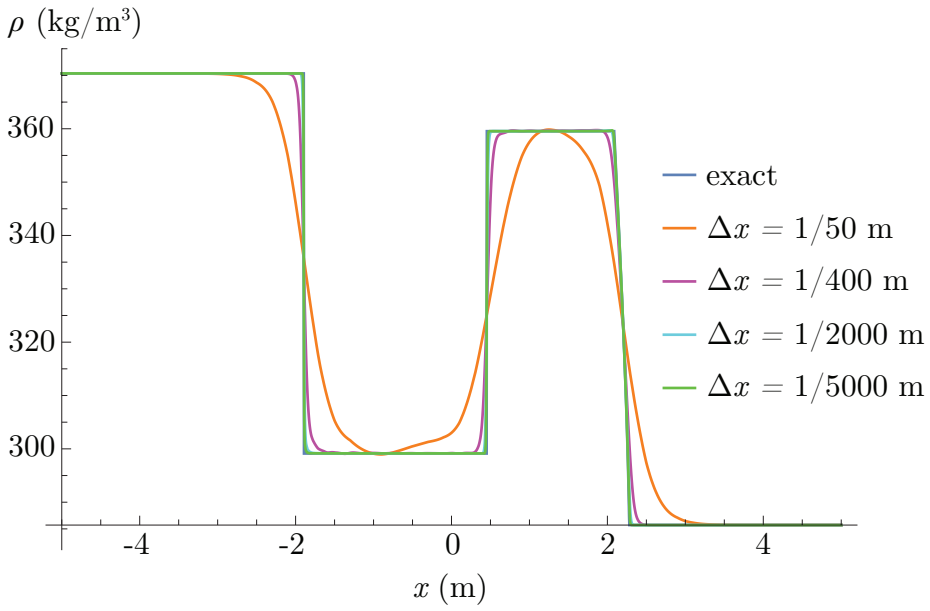

Figure 5.17. Visual convergence of WENO5M method with global Lax-Friedrichs flux-splitting to the inviscid exact solution for a shock tube with PP10 modeled as a van der Waals gas in the anomalous region.

CHAPTER 6

STEADY DETONATION DYNAMICS

In this chapter, inviscid, steady detonation dynamics with the van der Waals equation of state are studied. The aim is to understand how the van der Waals model and anomalous waves affect fundamental aspects of steady detonation theory. Throughout this chapter, comparison will be made between the ideal gas and van der Waals models. Steady detonation theory will also be applied to a van der Waals gas with initial conditions in the anomalous region. This chapter begins with Rayleigh line and Hugoniot curve analysis of the reactive system, and continues with steady ZND solutions. The understanding of anomalous wave dynamics established in the previous chapters will be used to assess steady detonation dynamics in the presence of anomalous waves resulting from non-convexities in Hugoniot curves. Although diffusion and viscosity are not considered here, detailed analysis of their effects in an ideal gas can be found in [105, 106]. The following analysis is guided by the text of Fickett and Davis [52] and Powers [95].

The system of equations presented in Chapter 2 are reduced to the inviscid reactive Euler equations. Characteristic analysis yields four real eigenvalues and four linearly independent left eigenvectors. This analysis is given in detail in [95]. The system is hyperbolic, and admits discontinuous solutions, described by the Rankine-Hugoniot jump conditions given in Eqs. (2.23 - 2.26). Parameters used for comparison between ideal gas and van der Waals models are given in Table 6.1, and are based on the parameters used in Henrick, et al. [66] and Romick, et al. [105]. The collision frequency factor A influences the half reaction length scale. The activation energy Θ

is given as a range, and the dimensionless activation energy, $\bar{\Theta} = \Theta/(p_o/\rho_o)$, is given for comparison to previous work. The heat release q was chosen for comparison with previous work in [66, 105]. The van der Waals parameters, a and b, are set to zero for all ideal gas calculations. Parameters given in Table 6.2 were chosen for a model material such that an anomalous region exists in the gas phase and time and length scales of the reaction allow for tractability of numerical solutions.

TABLE 6.1

PARAMETERS FOR DETONATION DYNAMICS, BASED ON THE PARAMETERS OF [105].

Parameter	Value	Units
R	166.613	J/kg/K
γ	1.2	
c_v	833.387	J/kg/K
A	1.0×10^9	1/s
Θ	$[2,533,125;\ 3,232,400]$	J/kg
$\bar{\Theta}$	[25; 32]	
q	5.06625×10^6	J/kg
$\bar{q}$	50	
p_o	101325	Pa
ρ_o	1	$\mathrm{kg/m^3}$
a	55.8621	$\mathrm{m^6Pa/kg^2}$
b	0.00126155	$\mathrm{m^3/kg}$

TABLE 6.2

PARAMETERS FOR DETONATION STABILITY ANALYSIS WITH AN ANOMALOUS REGION IN THE GAS PHASE

Parameter	Value	Units
R	14.484	J/kg/K
c_v	1131.588	J/kg/K
A	5.0×10^6	1/s
Θ	$[2.0 \times 10^4, 2.5 \times 10^4]$	J/kg
q	$[1.0 \times 10^4, 4.0 \times 10^4]$	J/kg
a	22.389	$\mathrm{m^6Pa/kg^2}$
b	7.244×10^{-4}	$\mathrm{m^3/kg}$

6.1 Rayleigh Line and Hugoniot Curve Analysis

The general Rayleigh line and Hugoniot curve in Eqs. (4.17) and (4.18) are valid for all stages of the reaction. The Rayleigh line does not change across the reaction, while the Hugoniot curve shifts as the reaction progresses. Substituting $e = e(p, v, \lambda)$, Eq. (2.7), the Hugoniot curve is now written as $p(\lambda, v)$. For the ideal gas equation of state, the Hugoniot curve for the reactive system is

$$p = \frac{2\lambda q + p_o\left(\frac{\gamma+1}{\gamma-1}v_o - v\right)}{\left(\frac{\gamma+1}{\gamma-1}v - v_o\right)}, \tag{6.1}$$

and for the van der Waals equation of state, the Hugoniot equation becomes

$$p = \frac{p_o\left(\frac{c_v}{R}\left(v_o - b\right) + \frac{v_o - v}{2}\right) - a\frac{c_v}{R}\left(\frac{b}{v_o^2} - \frac{b}{v^2} - \frac{1}{v_o} + \frac{1}{v}\right) - a\left(\frac{1}{v_o} + \frac{1}{v}\right) + \lambda q}{\frac{c_v}{R}\left(v - b\right) - \frac{1}{2}\left(v_o - v\right)}. \tag{6.2}$$

6.1.1 Classical Domain

The van der Waals model is first exercised in the classical domain with parameters in Table 6.1, enabling comparison of CJ theory with the ideal gas and van der Waals gas models. A set of Hugoniot curves and Rayleigh lines are shown in Fig. 6.1 for the ideal gas and van der Waals equations of state, 6.1(a) and 6.1(b), respectively. Hugoniot curves have been plotted with $\lambda = [0, 0.5, 1]$, and two possible Rayleigh lines are shown, the first with $D = 2800$ m/s. The second Rayleigh line shown is given with the respective speeds at which the Rayleigh line is tangent to the $\lambda = 1$ Hugoniot curve for one-step irreversible kinetics, denoted with the point "CJ". This speed, denoted by D_{CJ}, is called the CJ speed, named for the independent work of Chapman [20] and Jouguet [72]. For the ideal gas, the CJ speed can be found with

$$\frac{D_{CJ}^2}{p_o v_o} = \frac{1 + 4\frac{\gamma-1}{\gamma+1}\frac{q}{p_o v_o} - \left(\frac{\gamma-1}{\gamma+1}\right)^2 \pm 2\sqrt{\frac{2q}{p_o v_o}\frac{\gamma-1}{\gamma+1}\left(1 + 2\frac{\gamma-1}{\gamma+1} - \left(\frac{\gamma-1}{\gamma+1}\right)^2\right)}}{\left(\frac{\gamma-1}{\gamma+1} - 1\right)^2}, \tag{6.3}$$

derived in [95]. There are two possible values of D_{CJ} from this equation. The larger value is associated with the detonation branch, on which pressure increases and specific volume decreases. The smaller value is associated with the deflagration branch, for which pressure decreases and specific volume increases. We will not be concerned with the deflagration branch, as additional non-equilibrium processes, such as diffusion, are important there. For this case, differences between the ideal gas and van der Waals models are minimal, and the value of D_{CJ} is slightly higher for the van der Waals gas. This indicates that in order for the reaction to complete, the

minimum velocity of the wave is faster for the van der Waals gas.

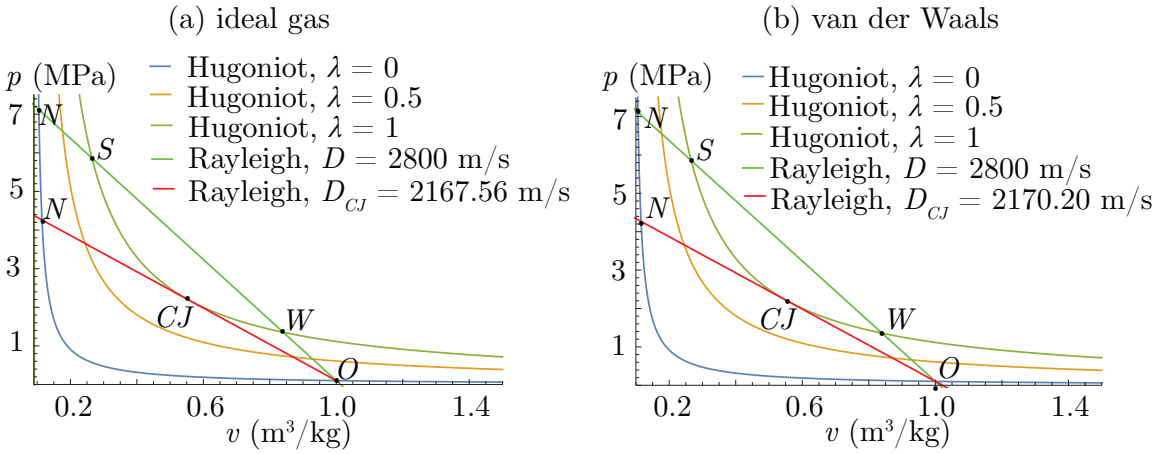

Figure 6.1. Rayleigh lines and Hugoniot curves for a) the ideal gas and b) the van der Waals equations of state. Hugoniot curves are shown at $\lambda = [0, 0.5, 1]$ and Rayleigh lines are given at $D = 2800$ m/s and the corresponding CJ speeds for each case.

As in the inert case, the Mach number calculated in the wave frame $M^2 = \hat{u}^2/c^2$ is a useful quantity to track for consistency with compressible flow theory. A standing normal shock must bring a flow from a supersonic state to a subsonic state. Throughout the reaction, the Mach number will then relax to the equilibrium state, which for the CJ state is $M = 1$. The relaxation to a sonic point is part of what defines the CJ state. For the current cases, the Mach number at all points obeys these rules, being supersonic at the initial state O and subsonic at the shocked state N; the Chapman-Jouguet point CJ is a sonic point with $M = 1$. For the strong solutions, the Mach number values at points O, N, and S are: $(M_O, M_N, M_S) = (8.030, 0.310, 0.542)$ for the ideal gas model, and $(M_O, M_N, M_S) = (8.026, 0.310, 0.543)$ for the van der

Waals model.

This work will focus on piston-driven waves, and a relation between the wave speed and the supporting piston velocity will be useful. The Rankine-Hugoniot jump equations can be recast with the final state, given subscript f, taken at $\lambda = 1$ and the initial state at $\lambda = 0$. The shock frame velocity $\hat{u}$ is replaced with $u - D$, resulting in:

$$\rho_f (u_f - D) = -\rho_o D, \tag{6.4}$$

$$p_f + \rho_f (u_f - d)^2 = p_o + \rho_o D^2, \tag{6.5}$$

$$e_f + \frac{1}{2}(u_f - D)^2 + \frac{p_f}{\rho_f} = e_o + \frac{1}{2}D^2 + \frac{p_o}{\rho_o}. \tag{6.6}$$

Replacing e_f and e_o with $e(p, \rho, \lambda)$ for the desired equation of state, this system of equations can be solved for p_f, ρ_f, and D. For the ideal gas, this yields two sets of solutions. The resulting equation for D corresponding to the detonation branch is

$$D = u_f \left(\frac{\gamma+1}{4} + \frac{\gamma-1}{2}\frac{q}{u_f^2} + \sqrt{\gamma \frac{p_o}{\rho_o u_f^2} + \left(\frac{\gamma+1}{4} + \frac{\gamma-1}{2}\frac{q}{u_f^2} \right)^2} \right). \tag{6.7}$$

Using this equation, and the parameters in Table 6.1, the shock speed D versus the final piston velocity u_f are shown in Fig. 6.2(a). The minimum value of D is the CJ speed, $D_{CJ} = 2167.560$ m/s, and corresponds to a piston velocity of $u_f = 959.758$ m/s. If $u_f > 959.758$ m/s, the increase in the wave speed is supported by the piston itself. For piston velocities of $u_f < 959.758$ m/s, this equation predicts an increase in the wave speed with decreasing piston velocity. However, what is actually observed in experiment is a wave traveling at the CJ speed D_{CJ} which is fully supported by the combustion process.

Solving Eqs. (6.4-6.6) with $e(p, \rho, \lambda)$ for the van der Waals model yields four possible solutions. The resulting equations are unwieldy to reproduce but well handled

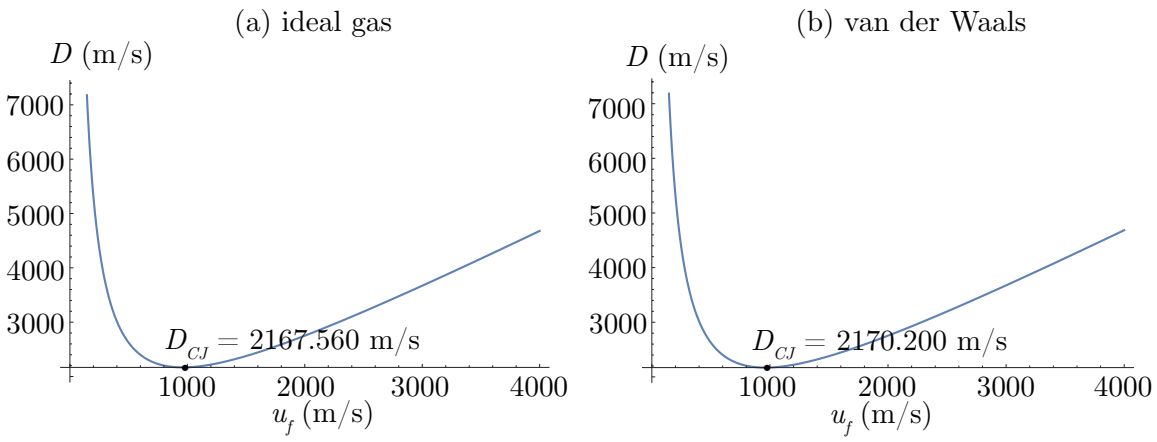

Figure 6.2. Shock speed D versus final piston velocity u_f for (a) an ideal gas and (b) a van der Waals gas with parameters in Table 6.1. The minimum value of D is the CJ value D_{CJ} and the corresponding piston velocity will be called u_{CJ}. If $u_f > u_{CJ}$, the wave speed D increases, and the piston itself is what provides the energy to drive the wave. If $u_f < u_{CJ}$, these plots show an increase in D, but what is actually predicted is a wave propagating at D_{CJ}.

by algebraic manipulation. The plot of D versus u_f for the van der Waals gas parameters in Table 6.1 is shown in Fig. 6.2(b). The CJ speed is higher than for the ideal gas model $D_{CJ} = 2170.200$ m/s at a final piston velocity of 959.772 m/s. The features of this plot are otherwise the same as the ideal gas case.

Three solution categories can be distinguish with the CJ speed: $D < D_{CJ}$, $D = D_{CJ}$, and $D > D_{CJ}$. If $D < D_{CJ}$ the slope of the Rayleigh line is such that it cannot intersect the complete reaction Hugoniot curve, and there are no real solutions that reach steady equilibrium. For the unique speed $D = D_{CJ}$, there is one solution for which the wave propagation is supported by the reaction only for one-step irreversible kinetics. The piston does not support the wave in this case, and downstream acoustic disturbances cannot overtake the reaction zone. For $D > D_{CJ}$ the Rayleigh line crosses the $\lambda = 1$ Hugoniot curve at two points, and there are two real solutions. These are called the weak and strong solutions, and will be denoted with points "W"

and "S", respectively. The solution corresponding to the higher pressure intersection point is the strong solution, and requires piston support to supply the additional energy necessary to drive the wave at this speed. The lower pressure intersection point corresponds to the weak solution, which in many cases is considered nonphysical for one-step irreversible kinetics, although this is not always the case.

6.1.2 Anomalous Domain

As seen in the inert cases in Chapters 4 and 5, for negative fundamental derivative, isentropes are non-convex, and Hugoniot curves also have non-convex regions. This section examines the ways in which non-convexities affect the Rayleigh line and Hugoniot curve analysis for a reactive system. Standard CJ solutions do not account for the additional intersections of the Rayleigh line and Hugoniot curve that may occur if the Hugoniot is non-convex. As a result, the intersection point that is expected to be the shocked state may not be an admissible shock solution. Parameters for this section are those in Table 6.2.

As a baseline for these parameters, the initial state is placed in the convex region at $(p_o,\ \rho_o) = (1.500 \times 10^6$ Pa, $\rho_o = 200$ kg/m$^3)$. Figure 6.3(a) shows the Hugoniot curves at $\lambda = [0,\ 0.5,\ 1]$ and Rayleigh lines at the CJ speed $D_{CJ} = 97.254$ m/s and $D = 110.000$ m/s. The Hugoniot curves remain convex throughout the reaction, and Rayleigh lines have no additional intersections with any of the Hugoniot curves. The Mach numbers at the initial state, shocked state, and CJ point are $(M_O,\ M_N,\ M_{CJ}) = (1.345,\ 0.572,\ 1.000)$. These are in agreement with requirements for compressible flow. The relationship between piston velocity and the shock speed is shown in Fig. 6.3(b). The plot is as expected, with a minimum at the CJ speed and increasing wave speed supported by increasing piston velocity. It is noted that the piston and wave speeds are much slower in this case, as is characteristic of the high densities near the critical point in many fluids satisfying the requirements to exhibit anomalous behavior in the

gas phase.

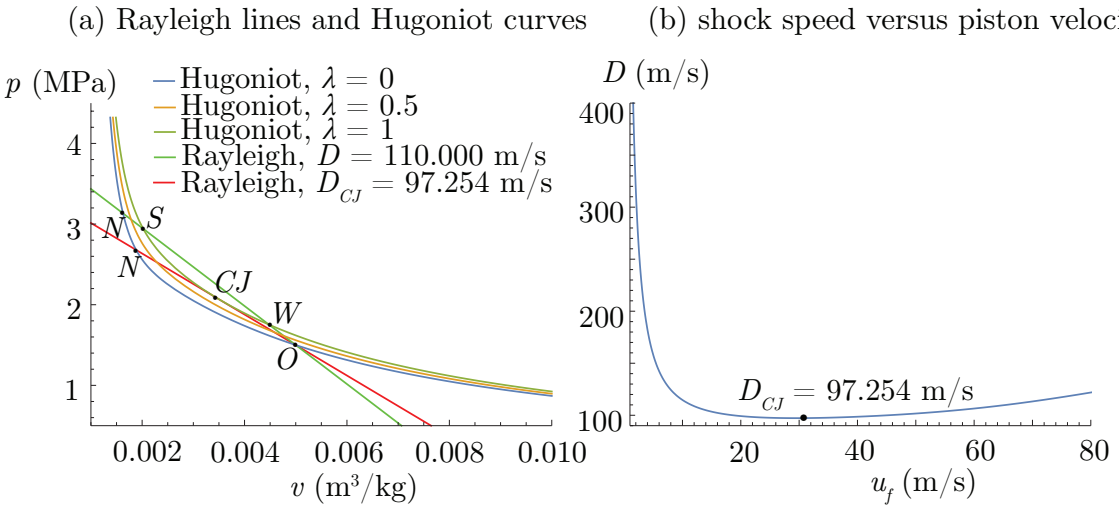

Figure 6.3. (a) Rayleigh lines and Hugoniot curves with initial condition in the classical region where the Hugoniot curves are convex; the heat release is $q = 40000$ J/kg. (b) The shock speed varies with the piston velocity as expected.

If the initial state is in the region of state space where the fundamental derivative is negative, at least some of the Hugoniot curves throughout the reaction will have regions of non-convexity. A large enough value of the heat release pushes the complete reaction Hugoniot curve fully outside of the anomalous region. Intermediate values of the heat release result in a complete reaction Hugoniot curve with mixed convexity, but may not necessarily result in anomalous waves. Figure 6.4(a) shows Rayleigh lines and Hugoniot curves for the initial state $(p_o, \rho_o) = (1.250 \times 10^6 \text{ Pa}, \rho_o = 250 \text{ kg/m}^3)$ and a heat release of $q = 40000$ J/kg. For this case, the features of this figure are largely the same as for the fully convex case. From the initial state O the gas is

shocked to state N. For the CJ speed $D_{CJ} = 59.385$ m/s there is one intersection point tangent to the complete reaction Hugoniot curve at point CJ. The Mach numbers at the initial, shocked and CJ points are (M_O, M_N, M_{CJ}) = (1.358, 0.226, 1.000). The overdriven Rayleigh line, shock speed $D = 70$ m/s, intersects at two points, the strong solution at point S and the weak solution at W. The Mach numbers at the initial, shocked and strong solution points are (M_O, M_N, M_S) = (1.601, 0.227, 0.411). In this case, although the $\lambda = 1$ Hugoniot curve is mixed convexity, there is no orientation of the Rayleigh line which intersects more than twice. The CJ speed is greater than the frozen sound speed at the initial state, thus the Mach number will be supersonic for all values of $D \geq D_{CJ}$. Figure 6.4(b) shows the shock speed as a function of piston velocity.

Decreasing the heat release to $q = 10000$ J/kg, the non-convex region of the complete reaction Hugoniot becomes larger, as shown in Fig. 6.5(a); numerical values of points of interest are given in Table 6.3. The Rayleigh line for the CJ speed now intersects the unreacted Hugoniot curve at a point intermediate to the shocked state at N. As discussed in the inert case, shock discontinuities for which there are intermediate intersection points of the Rayleigh line and Hugoniot curve between the initial and final states are inadmissible. Thus, the shock discontinuity from O to N at the CJ speed is not an admissible shock solution. This additional intersection point is also present in the $D = 33$ m/s Rayleigh line. There is an additional intersection of the Rayleigh line for D_{CJ} with the complete reaction Hugoniot curve at point A to the right of the initial state. The Rayleigh line for $D = 45$ m/s results in a shock of sufficient strength to reach state N without crossing the unreacted Hugoniot curve at an intermediate point. This shock is expected to behave as in the classical convex case, taking the flow from O to N on the inert Hugoniot curve, and ending at S as the reaction is completed.

Considering the Mach number, it is expected that admissible discontinuities are

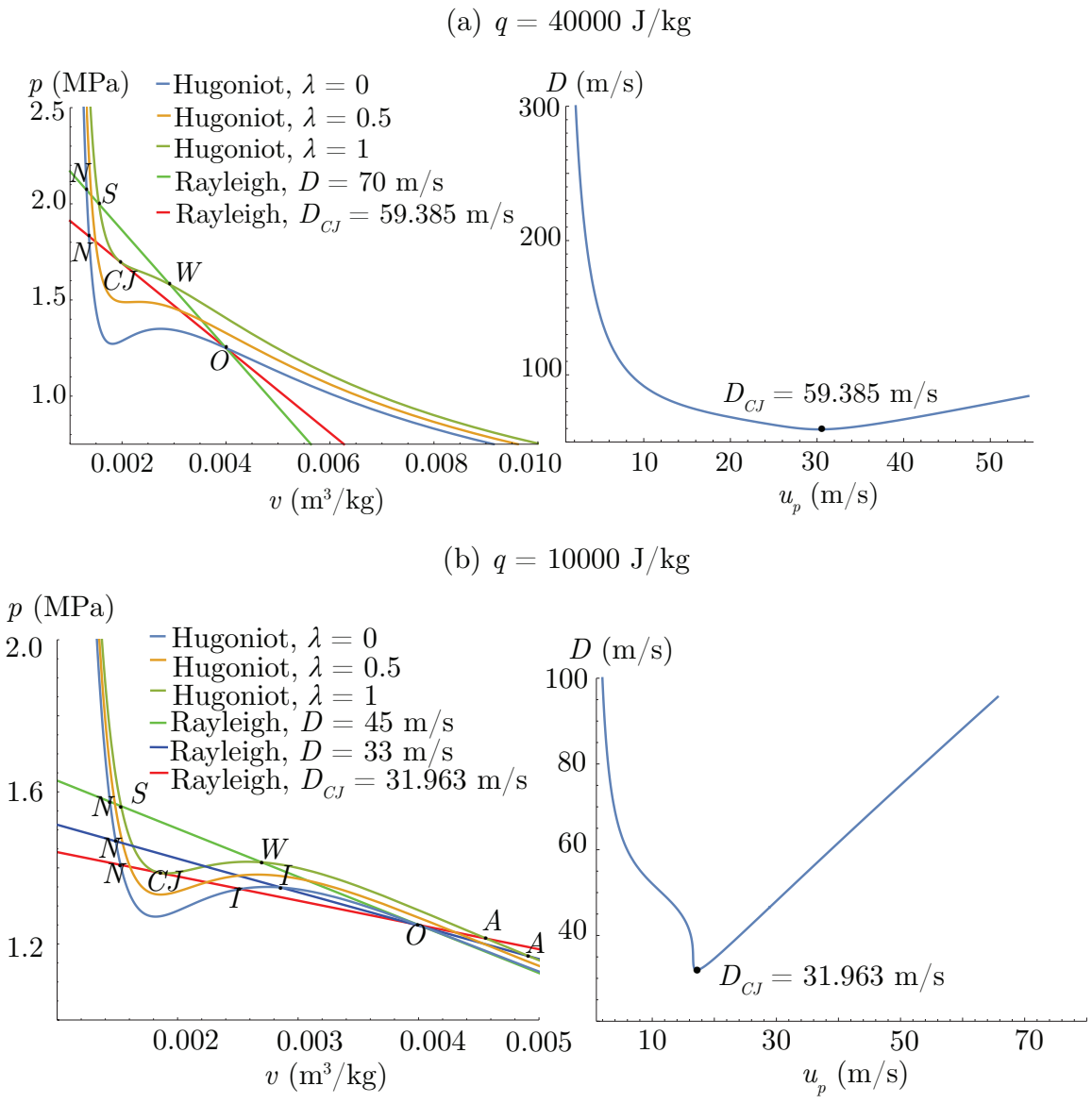

Figure 6.4. Plots with initial conditions $(p_o,\ \rho_o) = (1.500 \times 10^6$ Pa, $\rho_o = 200$ kg/m$^3)$ and heat release $q = 40000$ J/kg. (a) Rayleigh lines and Hugoniot curves with initial condition in the anomalous region. (b) Shock speed versus piston velocity.

taken from supersonic to subsonic across a shock discontinuity. However, for both $D = 33$ m/s and $D_{CJ} = 31.962$ m/s, the Mach number in the shock frame at the initial state is subsonic, 0.731 and 0.755, respectively. For shock speed $D = 45$ m/s,

(a) Rayleigh lines and Hugoniot curves (b) shock speed versus piston velocity

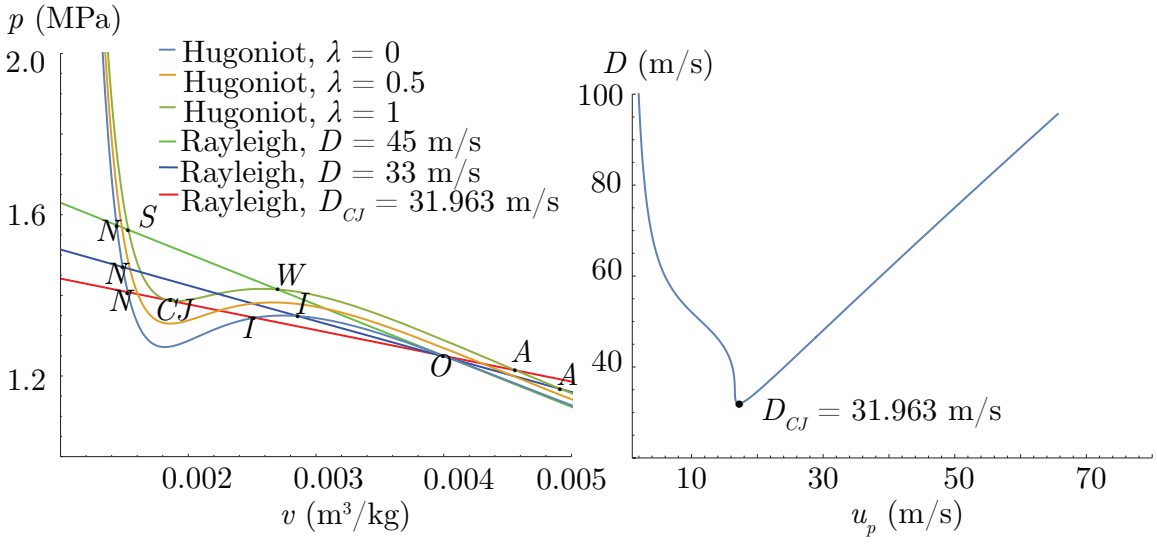

Figure 6.5. Plots with initial conditions $(p_o,\ \rho_o) = (1.500 \times 10^6$ Pa, $\rho_o = 200$ kg/m$^3)$ and heat release $q = 10000$ J/kg. (a) Rayleigh lines and Hugoniot curves with initial condition in the anomalous region. (b) Shock speed versus piston velocity.

the Mach number at the initial state is 1.029, and is supersonic. The sound speed at the initial state is $c = 43.720$ m/s, and any wave speeds less than this value would have initial state Mach numbers in the subsonic regime. It is due to the mixed convexity of the Hugoniot curve that it is possible for the CJ speed to be less than the ambient sound speed, resulting in a subsonic Mach number in the ambient state.

TABLE 6.3

NUMERICAL VALUES OF POINTS OF INTEREST FOR FIG. 6.5

	$D_{CJ} = 31.963$ m/s			$D = 33$ m/s			$D = 45$ m/s		
	ρ, kg/m^3	p, MPa	M	ρ, kg/m^3	p, MPa	M	ρ, kg/m^3	p, MPa	M
O	250.000	1.250	0.731	250.000	1.250	0.755	250.000	1.250	1.029
Q	393.634	1.344	—	388.131	1.347	—	—	—	—
CJ	540.944	1.387	1.000	—	—	—	—	—	—
N	655.214	1.408	0.220	658.614	1.419	0.220	694.908	1.574	0.224
S	—	—	—	573.667	1.404	0.506	653.018	1.562	0.293
W	—	—	—	504.667	1.387	—	370.473	1.387	2.275
A	219.146	1.214	0.694	217.392	1.209	0.717	—	—	—

6.2 The Reaction Zone

6.2.1 Pressure Evolution

This section discusses the structure of the reaction zone for steady detonations. The evolution of p as λ changes across the reaction zone is first considered. Beginning from the Rankine-Hugoniot jump equations in Eqs. (2.23-2.26) and substituting $e = e(p, \rho, \lambda)$, the system can be solved for (p, ρ, λ) as functions of the reaction progress λ. For the ideal gas, the solution for $p(\lambda)$ is

$$p(\lambda) = \frac{1}{\gamma + 1}\left(p_o + \rho_o D^2\left(1 \pm \sqrt{\left(1 - \frac{\gamma p_o}{\rho_o D^2}\right)^2 - \frac{2\left(\gamma^2 - 1\right)}{D^2}}\right)\right). \tag{6.8}$$

By prescribing the shock speed D, the positive and negative roots can be plotted together to show the possible paths from the initial condition to complete reaction for the pressure. A similar, but cumbersome, equation is found algebraically for the van der Waals gas; it is not practical to present here.

Starting with the solution parameters of Fig. 6.1, plots for the evolution of pressure versus reaction progress are shown for the ideal gas in Fig. 6.6(a), and for the van der Waals gas in Fig. 6.6(b). Each curve corresponds to a different shock speed, $D < D_{CJ}$, $D = D_{CJ}$, and $D > D_{CJ}$. If the shock speed is less than the CJ speed, the reaction is never completed, consistent with the Rayleigh line having no intersection point with the complete reaction Hugoniot curve. The first of these curves to reach $\lambda = 1$ is for $D = D_{CJ}$, and approaches the same final state from the initial and shocked state. For $D > D_{CJ}$, the strong and weak branches are evident. The strong solution starts at the shocked state with $\lambda = 0$ and pressure decreases as the reaction proceeds to the equilibrium state at $\lambda = 1$. The weak solution starts at the initial state and the pressure increases as it reaches $\lambda = 1$.

The next case corresponds to Fig. 6.4, the initial condition is in the anomalous

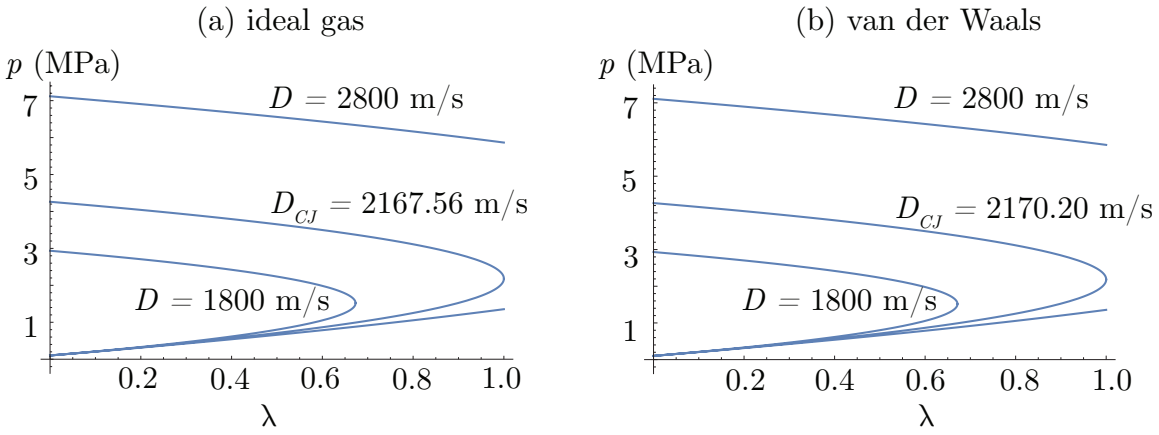

Figure 6.6. Pressure versus reaction progress for: (a) ideal gas, and (b) van der Waals gas, with parameters given in Table 6.1. For $D < D_{CJ}$ there is no solution that reaches the complete reaction state. For $D = D_{CJ}$ the pressure approaches one equilibrium state. For $D > D_{CJ}$ the strong solution starts at the shocked state, and pressure decreases to the complete reaction point. The weak solution starts at the initial state, and pressure increases to the complete reaction point.

region, but the heat release is large enough that analysis matches the convex region case. If $D < D_{CJ}$, the reaction has no completion point. At the CJ speed, the reaction reaches completion at the same point from both the initial state and the shocked state. For the overdriven wave, $D > D_{CJ}$, the strong and weak solutions have a decrease and increase in pressure, respectively, as the reaction progresses.

With additional intersection points of the Rayleigh lines with the complete reaction Hugoniot curves, the p versus λ plots are increasingly complicated. Corresponding to Fig. 6.5, Figure 6.8 shows the pressure evolution for each Rayleigh line in Fig. 6.5. At the CJ speed, Fig. 6.8(a), the top curve corresponds to the Rayleigh line tangent to the complete reaction Hugoniot curve. As discussed, the shock discontinuity from the initial state to the shocked state is not an admissible shock, although there is nothing in this plot to suggest that this is the case. The middle curve corresponds to the transition from the initial state to the point A. The lower

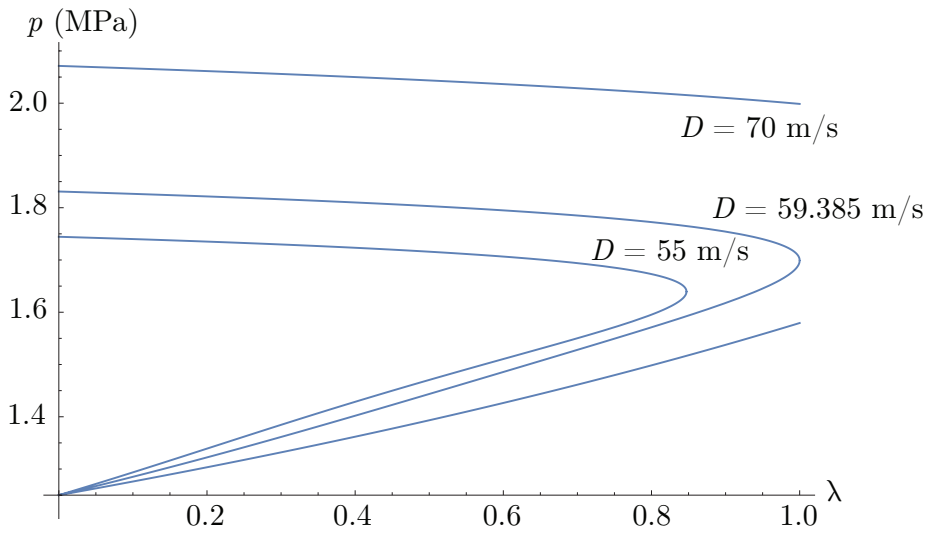

Figure 6.7. Pressure versus reaction progress for initial condition $(p_o, \rho_o) = (1.250 \times 10^6 \text{ Pa}, \rho_o = 250 \text{ kg/m}^3)$ and $q = 40000$ J/kg.

curve corresponds to an intersection point much farther down the Hugoniot curve and beyond of our domain of interest. For the overdriven wave, Fig. 6.8(b), there are just two curves, the shocked state N to the strong solution S and the initial condition O to the weak solution W. Although the weak solution is not in general of interest here, the curve for the weak solution is noted, as it is non-convex, whereas in all previous cases it has been convex. Returning to Fig. 6.5, the corresponding Rayleigh line passes through each successive Hugoniot curve at points where they are non-convex. For the underdriven wave, Fig. 6.8(c), the first curve does not reach completion, as expected.

Continuing analysis of the effects of anomalies in the Hugoniot curve on the relationship between p and λ, the solutions that lie well outside of our domain of interest are excluded in Fig. 6.9. Doing so clarifies what has really been captured by these solutions; all labels correspond to those in Fig. 6.5. From the initial state at O, there are three curves that reach completed reactions: the weak solution for an overdriven wave, the intersection point A of the D_{CJ} Rayleigh line, and the intersection A of

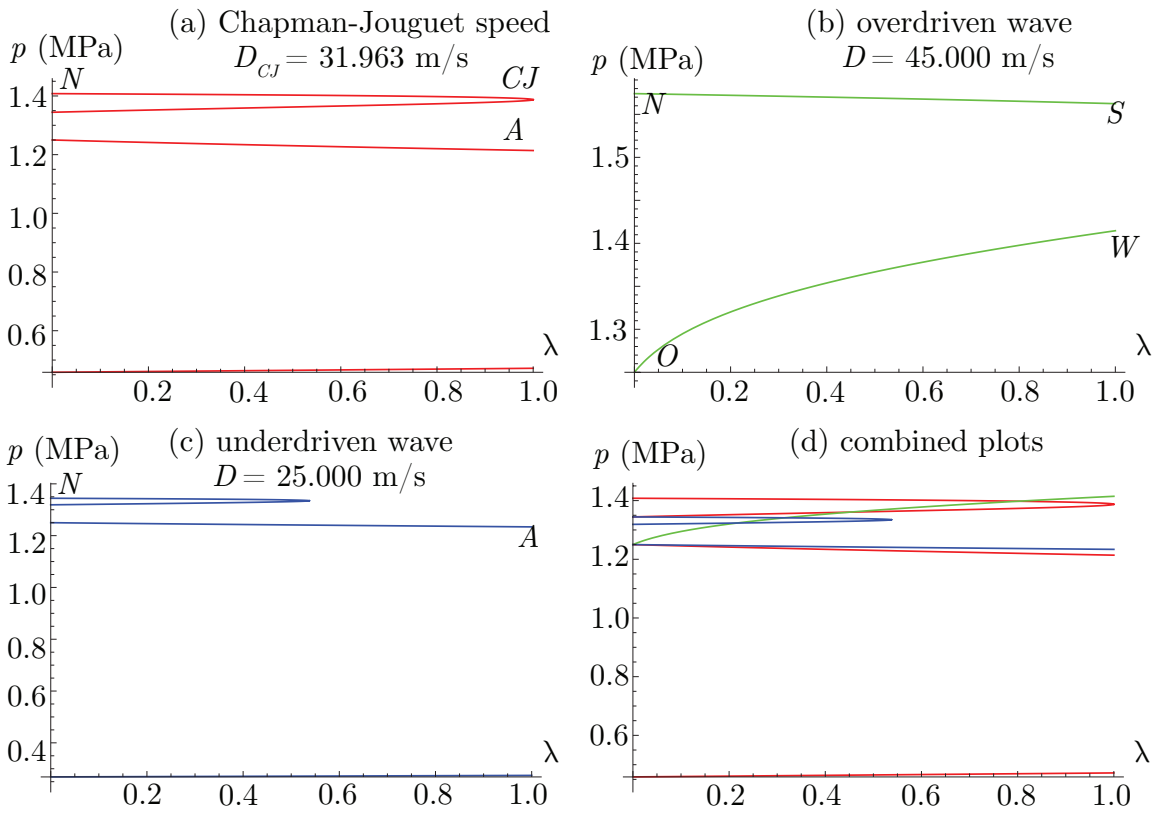

Figure 6.8. Pressure versus reaction progress for initial condition (p_o, ρ_o) = (1.250×10^6 Pa, $\rho_o = 250$ kg/m^3) and $q = 10000$ J/kg. Shock speeds are: (a) CJ speed (b) overdriven wave (c) underdriven wave (d) CJ, overdriven, and underdriven together.

the underdriven Rayleigh line. The weak solution crosses the other curves, which is consistent with the fact that the Hugoniot curves cross the same pressure values for multiple specific volumes. A curve from the initial state to the Chapman-Jouguet point CJ is not found. The CJ solution instead suggests that the starting points for the reaction are at the shocked state N and the intermediate crossing of the unshocked Hugoniot curve. Recalling Fig. 6.5, the D_{CJ} Rayleigh line remains under the $\lambda = 0$ Hugoniot curve until reaching this intermediate point. From inert analysis it is already known that the shock between O and N predicted by the D_{CJ} Rayleigh line is inadmissible. Allowing λ to become negative (although this has no physical mean-

ing) reveals a path from the initial state O to the intermediate intersection point, which then continues to the CJ point. This is taken as another indication that the standard CJ analysis has trouble in and around the anomalous region.

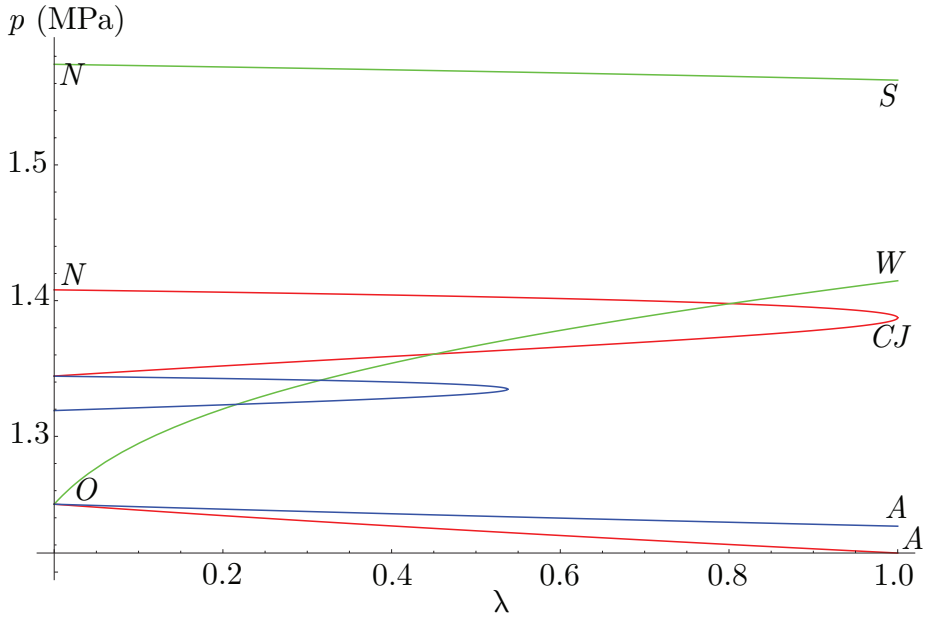

Figure 6.9. Pressure versus reaction progress for initial condition $(p_o, \rho_o) = (1.250 \times 10^6$ Pa, $\rho_o = 250$ kg/m$^3)$ and $q = 10000$ J/kg.

6.2.2 ZND Solutions

Steady wave analysis is concluded with consideration of the structure of the reaction zone for one-step irreversible kinetics, first studied by Zel'dovich [128], von Neumann [122], and Döring [40]. Following their work, the governing equations are written as a system of differential-algebraic equations for a steady one dimensional

detonation structure with one-step irreversible Arrhenius kinetics:

$$\begin{aligned}
\rho\hat{u} &= -\rho_o D, && (6.9)\\
\rho\hat{u^2} + p &= \rho_o D^2 + p_o, && (6.10)\\
e + \frac{1}{2}\hat{u^2} + \frac{p}{\rho} &= e_o + \frac{1}{2}D^2 + \frac{p_o}{\rho_o}, && (6.11)\\
p(T,v) &= \frac{RT}{v-b} - \frac{a}{v^2}, && (6.12)\\
e(T,v,\lambda) &= c_v T - \frac{a}{v} - \lambda q, && (6.13)\\
\frac{d\lambda}{dx} &= \frac{1-\lambda}{\hat{u}} a \exp\left(\frac{-\Theta}{RT}\right). && (6.14)
\end{aligned}$$

This system of equations can be simplified to one ordinary differential equation by solving for $\hat{u}(\lambda)$ and $T(\lambda)$. Fixing the shock speed, this system can be solved to find the ZND solution of a detonation.

The ZND solution procedure was originally formulated with the ideal gas equation of state, but substitution of the van der Waals equation of state is straightforward. Care must be taken though, as the jump equations have four roots with the van der Waals equation of state which may be imaginary or real. Figure 6.10 shows the ZND solution at the CJ speed with the van der Waals gas given in Table 6.1. The shock is located at $x = 0$ and values at $x > 0$ are in the ambient state. The reaction progress does not change across the shock; immediately after the shock it begins to increase, as the reaction is initiated by the temperature increase caused by the jump. The density, pressure, and particle velocity increase across the shock, followed by a decrease throughout the reaction zone to the equilibrium state. The temperature increases across the shock, then continues to rise throughout most of the reaction zone until a small decrease leads to the equilibrium temperature. These structures match the traditional ideal gas ZND solutions. The Mach number is supersonic downstream of the shock, subsonic immediately upstream of the shock, and as the reaction reaches

equilibrium the Mach number relaxes to 1 and the flow is sonic.

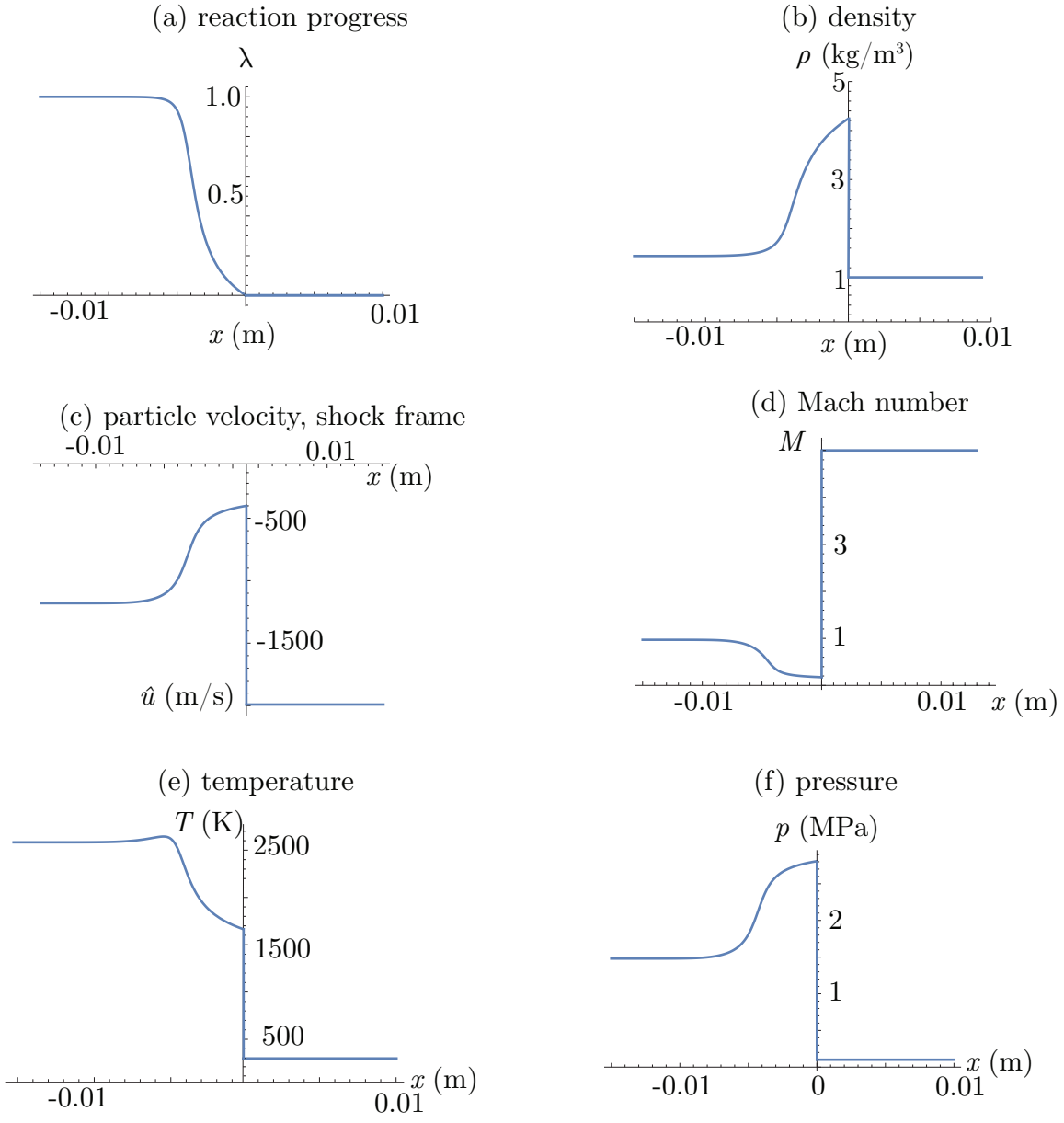

Figure 6.10. ZND solution for a van der Waals gas at the CJ speed with parameters based on those in Romick, et al. [105] given in Table 6.1.

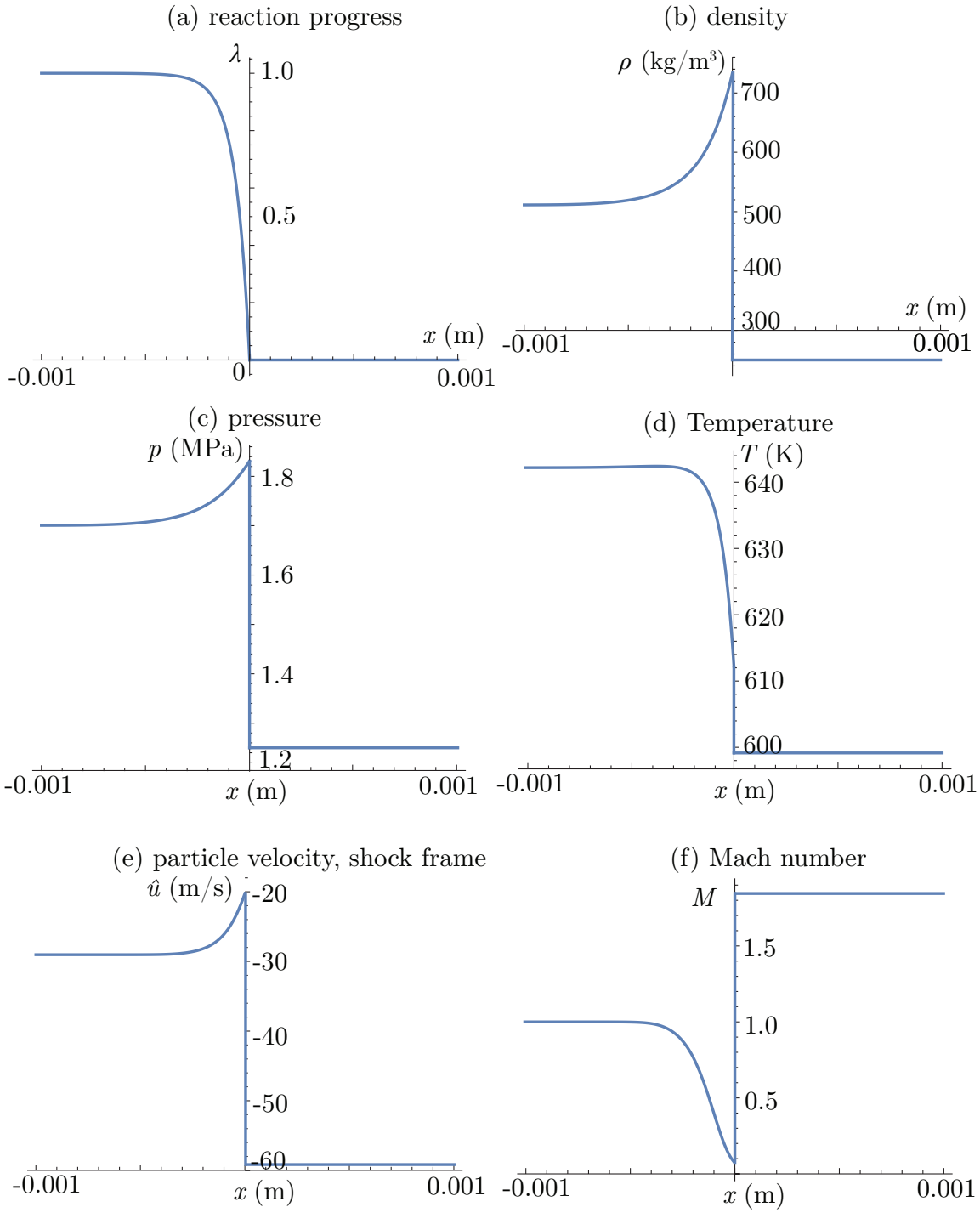

Figure 6.11. ZND solution for a wave traveling at the CJ speed in a van der Waals gas with an anomalous region near the critical point, parameters given in Table 6.2, and initial conditions in the anomalous region. The heat release is $q = 40000$ J/kg, large enough that the complete reaction Hugoniot curve is outside the anomalous region.

Figure 6.11 shows the ZND solution for a CJ speed wave in a van der Waals gas with parameters given in Table 6.2, the activation energy and heat release are $\Theta = 25000$ J/kg and $q = 40000$ J/kg, respectively. Although the initial condition in this case is in the anomalous region, the shock is of sufficient strength to form a discontinuous compression shock. The ZND analysis is therefore valid, and the shock structure behaves as expected. The shock induces a transition from supersonic to subsonic regimes, and the Mach number relaxes to $M = 1$ as the the reaction completes, characteristic of CJ detonations.

The ZND solution procedure assumes that the reaction occurs behind a discontinuous compression shock represented by the solution of the Rankine-Hugoniot jump conditions. Returning to the case presented in Fig. 6.5, ZND solutions are first calculated for the overdriven wave speed $D = 45$ m/s; the activation energy is still $\Theta = 25000$ J/kg. The density profile for the strong solution is shown in Fig. 6.12(a). The shock drives the density from the ambient state to the shocked state on the inert Hugoniot curve, and the reaction lowers the density to the equilibrium state on the complete reaction Hugoniot curve. At this speed, the initial shock drives the gas out of the anomalous region, and classical behavior of a reaction behind a compression shock is predicted. The shock induces a transition from supersonic to subsonic regimes, remaining in the subsonic regime as the equilibrium state is reached, represented by the Mach number in Fig. 6.12(b).

It has been shown that the mixed convexity of this case challenges standard steady CJ detonation analysis if the shock speed is lowered to a point where there are additional intermediate crossings of the unreacted Hugoniot curve. Shock speeds for which there are intermediate crossings of the unreacted Hugoniot curve do not have physically realizable compression shock solutions. However, the Rankine-Hugoniot jump conditions provide solutions connecting non-adjacent intersection points. The ZND solution procedure uses these shock jump solutions to solve for the structure of

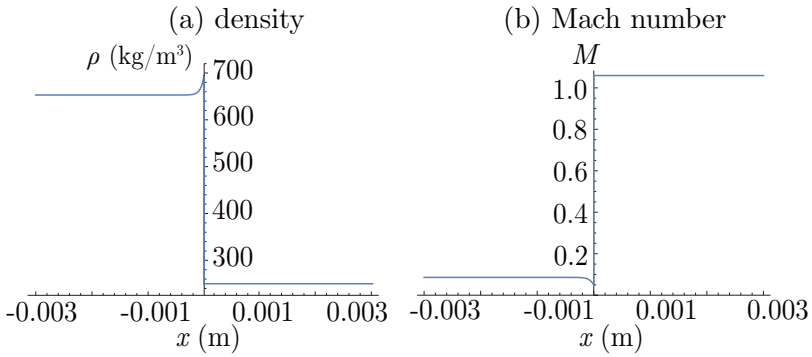

Figure 6.12. Overdriven ZND solutions corresponding to the $D = 45$ m/s Rayleigh line shown in Fig. 6.5.

the reaction zone, which if not paired with the Rayleigh line and Hugoniot curve analysis may appear as reasonable reaction zones behind discontinuous shocks. Analysis of the Mach number provides additional insight into why leading shock discontinuities are inadmissible, as some cases do not have shock jumps that induce a transition from the supersonic to subsonic regimes.

The next case reduces the heat release to $q = 10000$ J/kg, corresponding to the case in Fig. 6.5 with mixed convexity of the complete reaction Hugoniot curve. For the shock speed at which the Rayleigh line is tangent to the complete reaction Hugoniot curve, $D_{CJ} = 31.963$ m/s, the unreacted Hugoniot curve's mixed convexity results in additional intersections with the Rayleigh line. It has been shown that for this case the sound speed at the ambient state is greater than the CJ speed, resulting in the ambient state being subsonic in the shock frame. However, it is useful to discuss the results of ZND analysis to understand how the anomalous region affects steady detonation dynamics.

The ZND analysis yields four solutions, the density profiles of which are given in Fig. 6.13. The first solution, Fig. 6.13(a), corresponds with an intersection with the inert Hugoniot curve outside the bounds of Fig. 6.5; the entropy jump for this rarefaction shock is negative, and the solution is inadmissible. Fig. 6.13(b) is the

solution associated with the path from the initial state O to A. These is no shock in this case, although the structure of the reaction zone is reasonable, as the density decreases throughout the reaction before reaching an equilibrium state. This case will not be considered further here, but it is unlikely that it is a physically realizable solution.

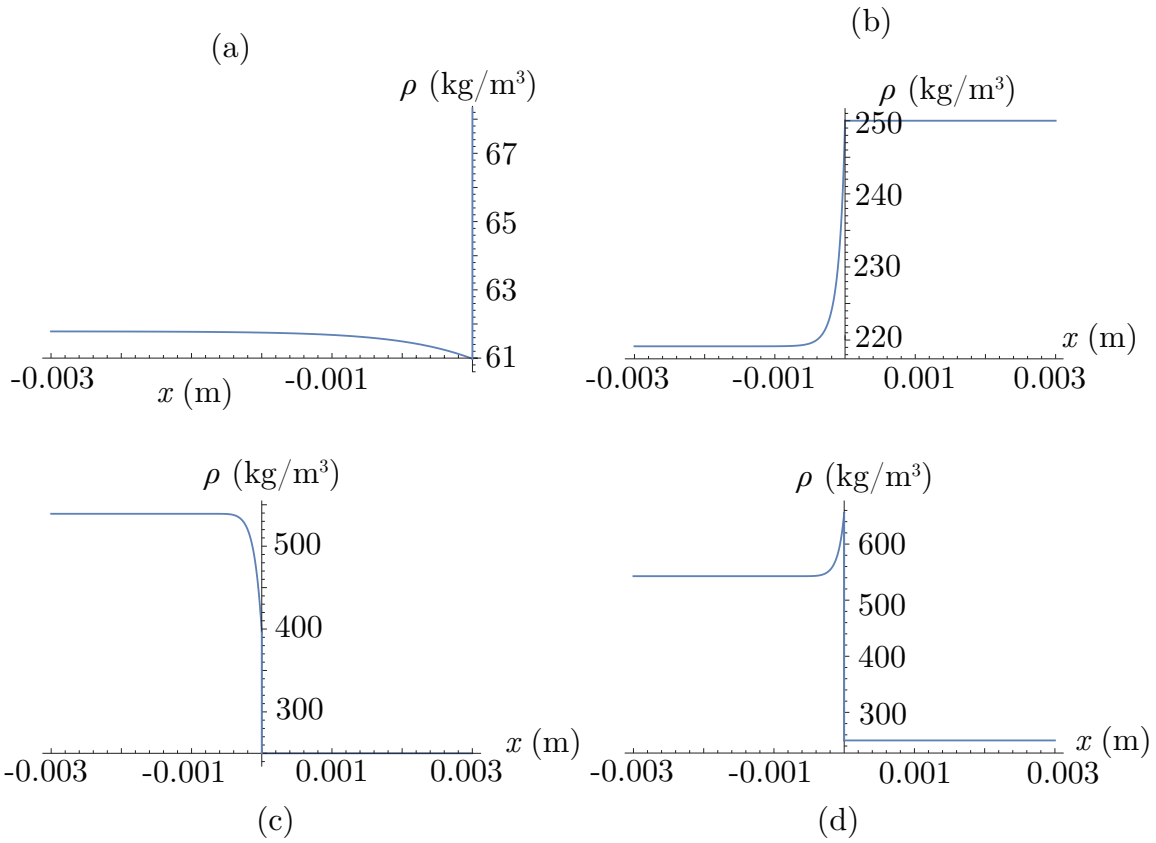

Figure 6.13. CJ speed ZND solutions if the Rayleigh line has more than two crossings with the complete reaction Hugoniot curve.

Fig. 6.13(c) and (d) both relax to the CJ state, but the ZND solution suggests that

both do so behind a shock jump. Although (c) is analogous to a path from the initial state directly to the CJ state, something that is not observed in nature, it is addressed briefly here so as to examine all potential complications of using the ZND model in regions of non-convexity. The jump presented in (c) is from the initial state O to the point Q. For this jump, the Rayleigh line passes through the anomalous region, where the relation of density and pressure with sound speed is inverted; therefore, as the density (and pressure) increase, the sound speed is decreasing, and the wave that would actually form in this case is a continuous homeoentropic compression fan. Thus, although the initial and end states would be the same, a different type of wave is expected to form. The solution that matches what is typically expected is (d), as the ZND solution corresponds to a shock jump from the initial state O to a shocked state N followed by a reaction to the equilibrium point CJ. However, even though the entropy change is positive, the jump from O to N is inadmissible as it crosses the inert Hugoniot at an intermediate point Q. The ZND solution procedure does not account for this, and if the intermediate crossing point was not accounted for, the solution presented in (d) would seem reasonable.

It is possible for wave speeds higher than the CJ speed to have intermediate crossings of the Rayleigh line with the unreacted Hugoniot curve. Increasing the wave speed to $D = 33$ m/s, the resulting ZND solutions are qualitatively similar to those at the CJ speed, as shown in Fig. 6.14. For this case, the Mach number in the shock frame at the ambient state is also subsonic, and these potential shock jumps are considered inadmissible.

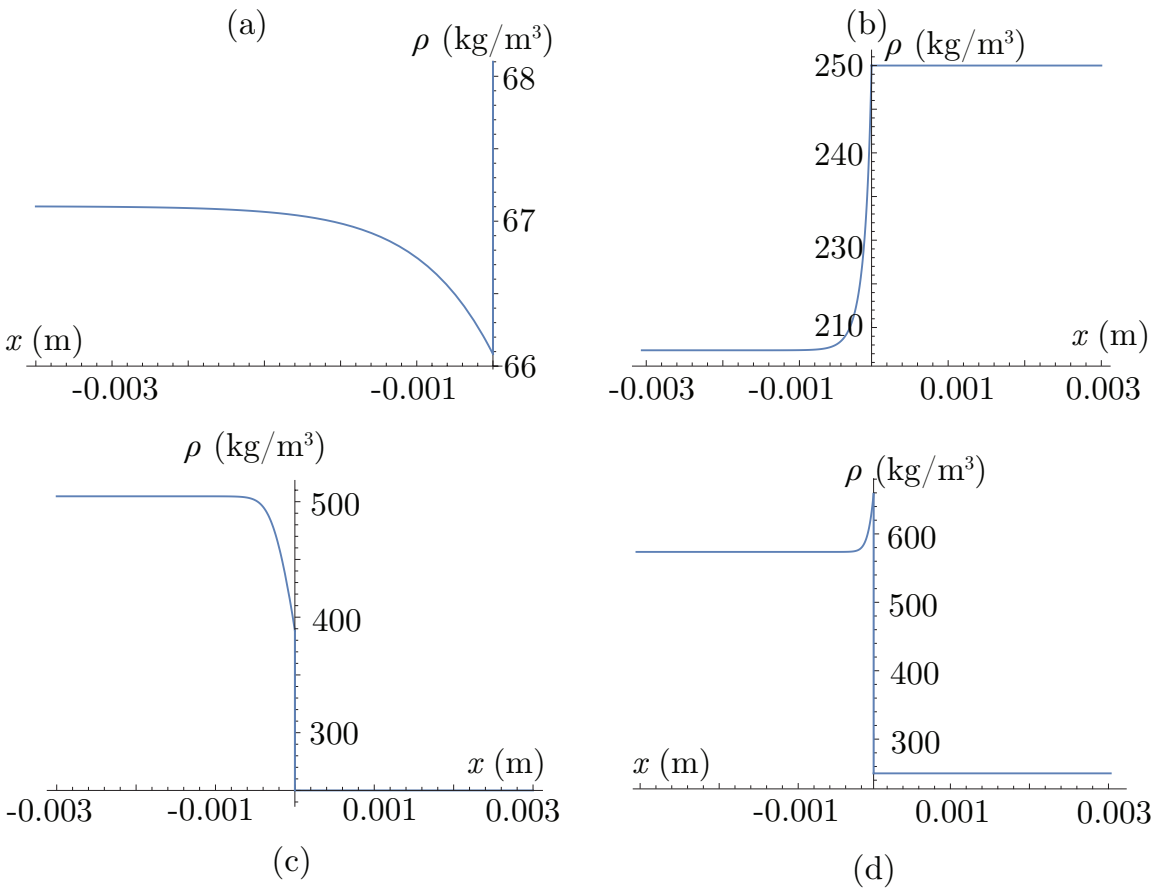

Figure 6.14. ZND solutions if the Rayleigh line has more than two crossings with the complete reaction Hugoniot curve, but the shock speed $D = 33$ m/s is greater than the CJ speed.

CHAPTER 7

UNSTEADY DETONATION DYNAMICS

In this chapter, unsteady detonations in the inviscid limit are presented. First, time-dependent detonations are studied, including with anomalous waves. It is shown that a detonation driven by an anomalous composite wave has the expected dynamics of a detonation driven wave. Then, unstable detonations solutions are compared with both the ideal gas and van der Waals equations of state. The goal is to understand the effects of including non-idealities on pulsating detonations, utilizing analysis of pressure in the temporal and frequency domains to describe the detonation instabilities. DFTs for various grid sizes are compared for verification of unsteady dynamics. It is shown that the length scales of the limit cycles in an unsteady detonation may be smaller than the length scale of the reaction zone, requiring a finer grid to capture the oscillatory behavior. The transition to instability with increasing activation energy for the ideal gas and van der Waals gas is compared. It is shown that the van der Waals model delays the transition to instability relative to the ideal gas. Limit cycles in the peak pressure are analyzed for detonations with the same activation energy for each case.

The numerical method used is the WENO5M method described in Section 3.4, and the governing equations are transformed into the piston-attached coordinate system. The domain is discretized into a uniform grid with nodes at positions $\xi_i = (i-1)\Delta\xi$ where $(i = 1, 2, \cdots, N)$, where $\Delta\xi = \xi_N/(N-1)$. The domain is initialized everywhere at the ambient state with zero velocity. The piston begins at rest and is accelerated to a constant velocity v_{pf} by a set time t_{pf}; the piston velocity is thus

given by

$$v_p(t) = \begin{cases} v_{pf} \sin\left[\frac{\pi}{2}\left(\frac{t}{t_{pf}}\right)\right] & \text{for } 0 < t < t_{pf} \\ v_{pf} \text{ for } t > t_{pf}. \end{cases} \tag{7.1}$$

An example of this with $v_{pf} = 1410$ m/s and $t_{pf} = 2$ μs is shown in Fig. 7.1. The value of v_{pf} can be varied to achieve the desired wave speed. The value of t_{pf} is the time at which the piston reaches its maximum velocity, and is chosen such that it is short relative to the time it takes for the detonation wave initiated by the piston to fully develop. Results in this chapter are presented in the piston frame; conversion to the lab frame simply shifts the domain the distance the piston has traveled.

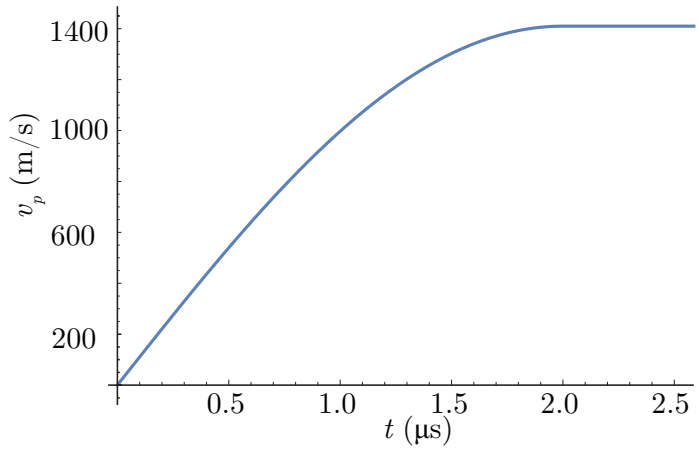

Figure 7.1. Profile of the piston acceleration for $v_{pf} = 1410$ m/s and $t_{pf} = 2$ μs.

7.1 Transient Relaxation to Steady Non-Oscillatory Detonations

Under certain conditions, typically large piston velocity, the piston will drive a non-oscillatory detonation wave that persists with time. The objective of this section is to determine what such detonations may look like if the initial ambient state is in the anomalous region. Parameters for this section are those in Table 6.2. A piston is driven into first an inert gas and then into a reactive gas so as to compare the resulting shock structures. The initial state for all cases in this section is in the anomalous region at $(p_o,\, \rho_o) = (1.250 \times 10^6 \text{ Pa},\, \rho_o = 250 \text{ kg/m}^3)$ and the heat release is $q = 10000$ J/kg. For the first case the activation energy is $\Theta = 25000$ J/kg, and the density profiles for the inert and reactive systems are shown in Fig. 7.2. The piston has been set such that the resulting wave is a classical compression shock traveling at 45 m/s. The detonation structure is as expected, with the reaction beginning behind the shock and relaxing to the equilibrium state.

Reducing the speed of the driving piston, the resulting wave becomes a composite compression wave. As discussed in Section 5.3, composite shocks develop if the wave speed is such that there are intermediate intersection points of the Rayleigh line and Hugoniot curve. Such intermediate intersections were shown to occur for the reactive system in Fig. 6.5. It is expected then that the leading shock for these cases would be a composite compression shock with a leading compression fan and trailing shock discontinuity.

Using a Heaviside function, the reaction may be allowed to advance in the continuous compression fan, or may be held until the shock discontinuity has passed. The reaction is first allowed to occur in the compression fan, and the resulting shock structures in the inert and reactive system are shown in Fig. 7.3. The parameters match those for Fig. 6.5, the activation energy is $\Theta = 25000$ J/kg; the final piston velocity is $u_{pf} = 22$ m/s. The reaction occurs fully in the continuous fan, driving the fan faster than the trailing shock and separating the composite wave. The discontin-

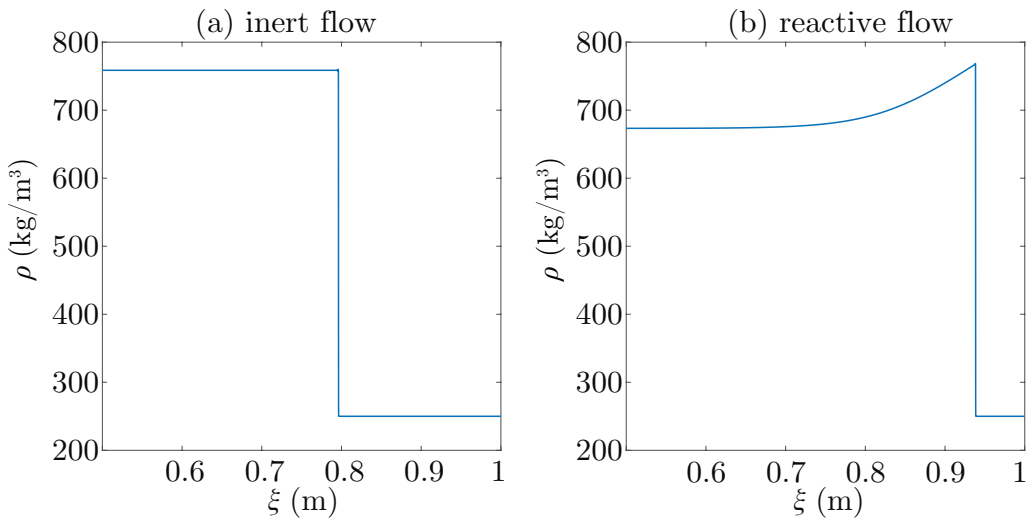

Figure 7.2. An inert and reactive shock from an initial condition in the anomalous region, $p_o = 1.250 \times 10^6$ Pa, $\rho_o = 250$ kg/m^3. The shock speed is large enough to push the gas out of the anomalous region, resulting in (a) a classical compression shock in the inert system, and (b) a typical overdriven detonation in the reactive system.

uous shock is weaker as a result, and the final state of the flow is at a lower density than for the inert composite shock. The reaction has steepened the compression fan, but it remains a continuous compression fan as the reaction occurs fully within the anomalous region. It is difficult to discern much from this case, as it is unclear how best to analyze features such as the Mach number, which is typically assessed in the frame of the shock. However, if the reaction occurs in the continuous compression and separates from the shock, no part of the wave is steady and transformation into the wave frame is more complex. The dynamics in this case are more complex, and will be left as an exercise for future work.

If the reaction does not begin until after the entire composite wave has passed, the structure of the reaction zone is the more familiar von Neumann spike, as seen in Fig. 7.4. The piston velocity has been increased to $u_{pf} = 25$ m/s, and the activation energy has been lowered to $\Theta = 20000$ J/kg to maintain a domain length of 1 m. In

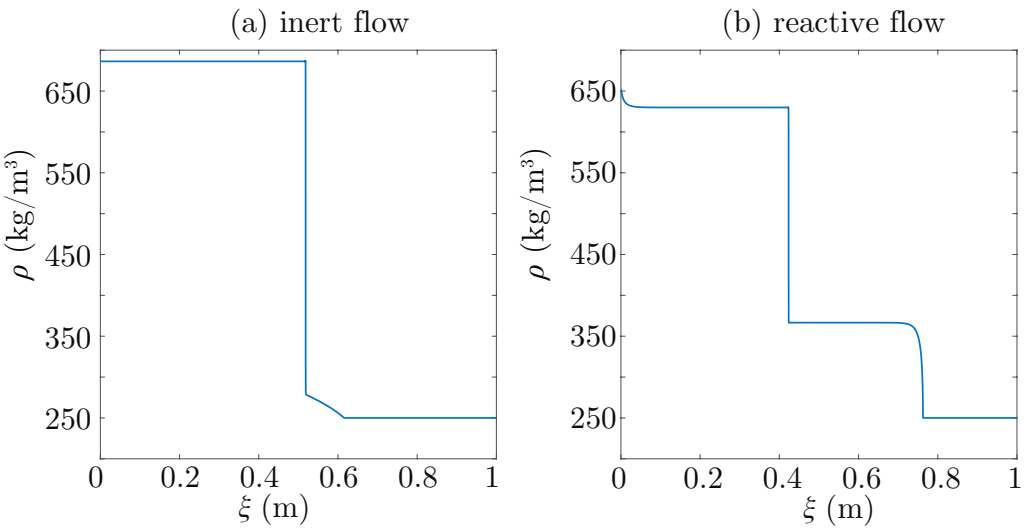

Figure 7.3. An inert and reactive shock from an initial condition in the anomalous region, $p_o = 1.250 \times 10^6$ Pa, $\rho_o = 250$ kg/m^3. The shock speed is not large enough to push the gas out of the anomalous region, resulting in (a) an anomalous composite compression in the inert system, and (b) a separated shock structure in the reactive system.

this case, although the reaction is now driving the entire wave forward, it does not drive the discontinuity fast enough to fully overtake the continuous fan at the head of the composite wave. Instead, the fan continues to spread as in the inert case, and the discontinuity travels at the speed of the tail end of the fan. Although the leading continuous fan is not steady, spreading as the wave travels over time, the final state of the shock is steady. As a result, it would be possible to use this final state as the starting point for ZND analysis in the steady frame for this case.

Although the compression fan at the head of the wave is not steady, the trailing shock travels at a constant speed, allowing for an assessment of the Mach number in the shock frame throughout the flow; the square of the Mach number is shown in Fig. 7.5. In the classical case, the downstream Mach number is supersonic and the upstream Mach number is subsonic. This was shown to be true in the inert case for both the compression and rarefaction shocks. In this case, throughout much

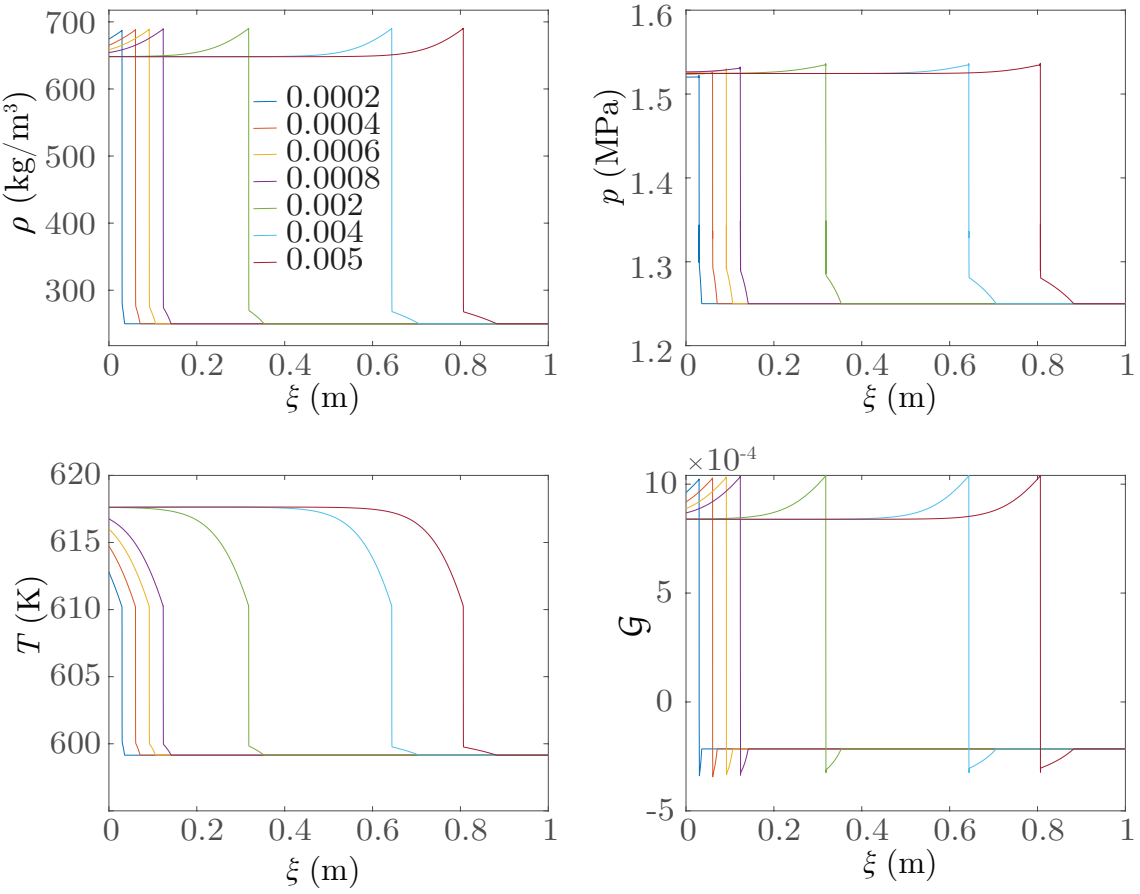

Figure 7.4. Evolution of a detonation wave behind an anomalous composite compression if the reaction does not begin until after the discontinuous shock. The final piston velocity is $u_{pf} = 25$ m/s, the heat release is $q = 10000$ J/kg, and the activation energy is $\Theta = 20000$ J/kg. In this case, the reaction does not drive the shock fast enough to overcome the speed of the compression fan.

of the compression fan the Mach number is subsonic and becomes supersonic just before the transition from continuous to discontinuous; this is expected behavior for a composite wave [32]. Downstream of the shock, the Mach number is subsonic and increases slightly as the reaction progresses to its equilibrium state.

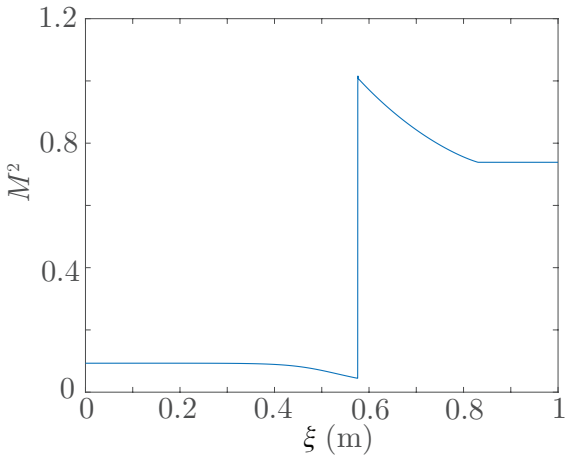

Figure 7.5. The square of the Mach number M^2 throughout the flow for a detonation behind an anomalous composite compression wave. The compression shock travels at a constant speed, and the particle velocity was put in the shock's frame of reference to calculate the Mach number.

The evolution of the composite wave and detonation can also be seen in ξ-t diagrams of density and temperature in Figs. 7.6 and 7.7, respectively. The spatial coordinate is in the piston frame, and the piston is at $\xi = 0$ for all time. As the composite wave forms, the compression fan spreads as time progresses, and the constant velocity of the discontinuous shock can be seen. After an ignition period, the reaction occurs behind the shock, decreasing the density and increasing the temperature as it progresses. Although the leading shock is anomalous, the evolution of the reaction behind the discontinuity is consistent with classical predictions.

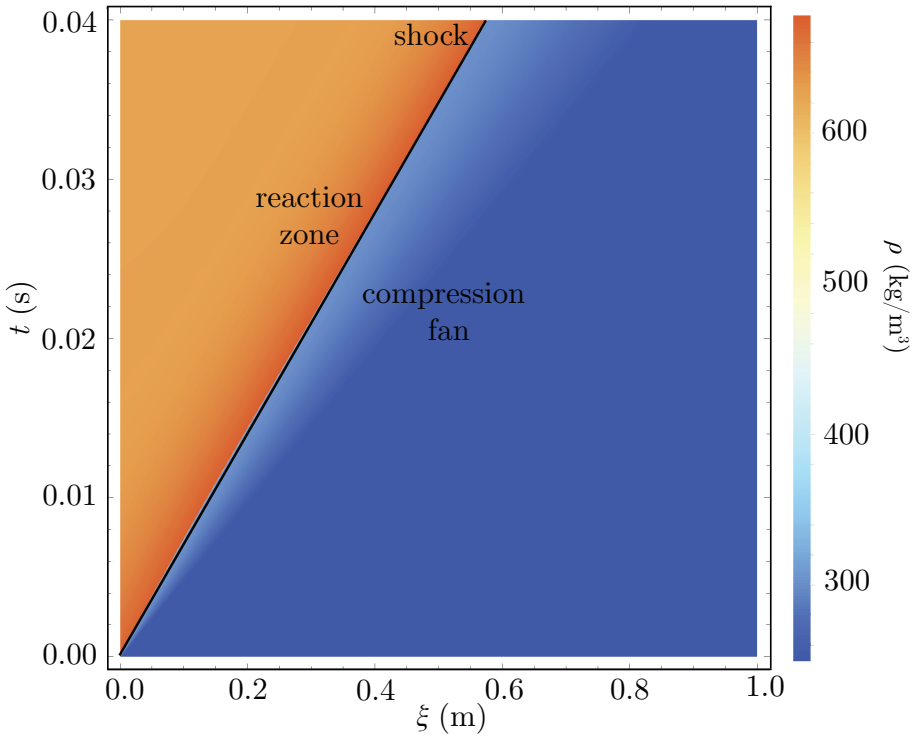

Figure 7.6. ξ-t diagram of density for a reaction behind an anomalous composite compression wave. Features include the leading compression fan continuing to spread, followed by the discontinuous shock. Behind the shock, the reaction progresses, and the density decreases.

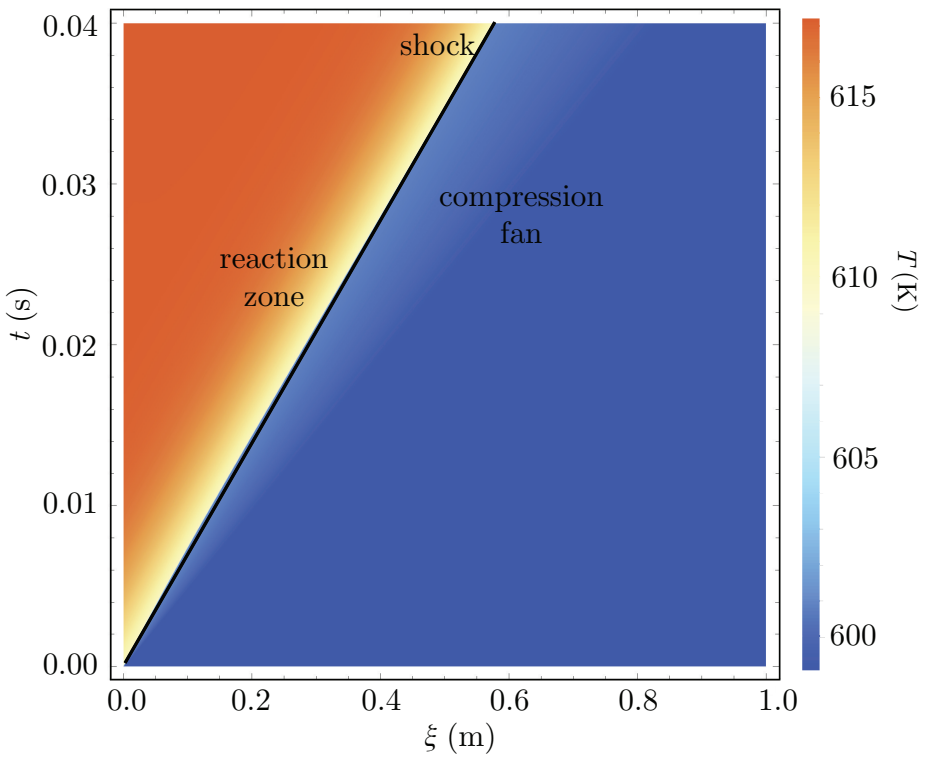

Figure 7.7. ξ-t diagram of temperature for a reaction behind an anomalous composite compression wave. Features include the leading compression fan continuing to spread, followed by the discontinuous shock. Behind the shock, the reaction progresses, and the temperature decreases.

7.2 Transient Relaxation to Oscillatory Limit Cycle Detonations

This section analyzes the effect of the van der Waals model on detonation stability in the classical regime. Figure 7.8 shows the maximum pressure versus time for an unstable piston-driven detonation. The full temporal domain is shown to illustrate the initial transients due to the piston acceleration and the detonation. At a later time the detonation settles into a limit cycle; it is this limit cycle that is of interest. The wave speed increases and decreases periodically, resulting in oscillations in the peak pressure. The parameters in this section are those in Table 6.1, which are based on those in Henrick, et al. [66] and Romick, et al. [105].

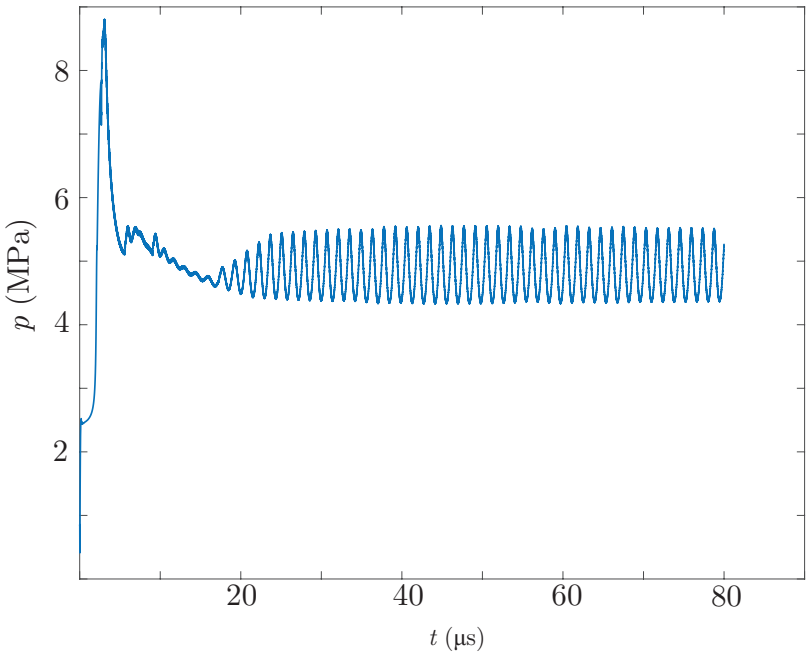

Figure 7.8. Maximum pressure over time for an unstable piston-driven detonation in a van der Waals gas. The full time domain is given to show the initial transients due to the piston acceleration and the detonation. At later time the detonation relaxes to a limit cycle.

The transition to instability is first considered in the ideal gas limit. The activation energy plays a significant role in the stability of a detonation, as discussed by Henrick, et al. [66]. Lee and Stewart's [76] linear stability analysis determined that the steady ZND wave is linearly stable for dimensionless activation energy $\bar{\Theta} < 25.26$, and linearly unstable otherwise. Setting the driving piston to a final velocity of 950 m/s, the resulting detonation wave travels at the CJ speed. Based on the work presented by He and Lee [64], results for two activation energies, $\bar{\Theta} = 25$ and $\bar{\Theta} = 26$, are shown in Fig. 7.9. The detonation is stable for $\bar{\Theta} = 25$, and has a period-1 instability for $\bar{\Theta} = 26$. In the nondimensionalized time, the period of the unstable detonation is approximately 13, which compares favorably to the results presented in Fig. 4 of Henrick et al. [66].

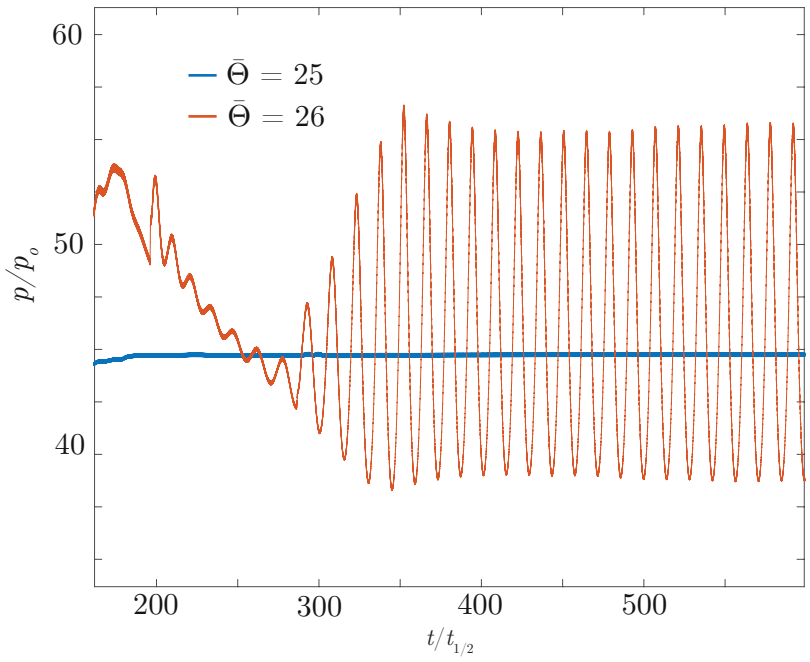

Figure 7.9. CJ detonations in an ideal gas, $\bar{q} = 50$. The detonation is stable for activation energy $\bar{\Theta} = 25$, and unstable for $\bar{\Theta} = 26$.

Two activation energies are examined to discern the effects of the van der Waals equation of state on pulsating detonation instabilities. The parameters are those in Table 6.1. By tracking the peak pressure at each time step, a DFT can be done for each case. See Appendix C for additional details on DFTs. The DFT decomposes the signal into its Fourier modes, the amplitudes of which provide a useful description of the signal. The amplitude of a frequency is proportional to the energy contained in that frequency. Additional details about DFTs can be found in [98].

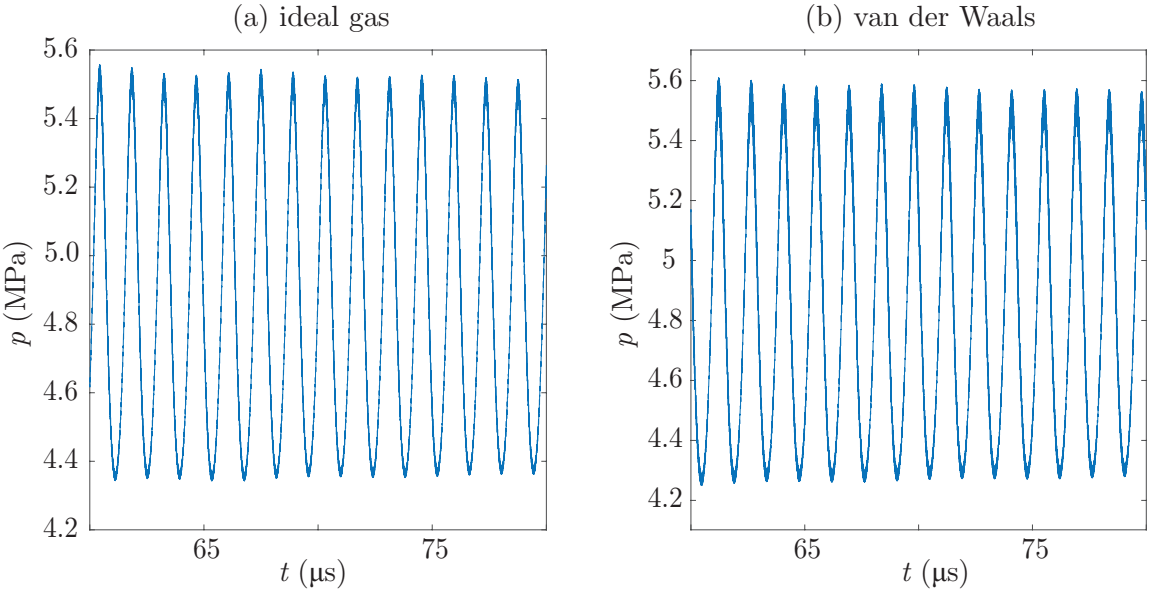

Figure 7.10. Pressure versus time for a single-mode detonation instability in an (a) ideal gas and (b) van der Waals gas. The piston velocity is $u_p = 1410$ m/s, and the dimensionless activation energy is $\bar{\Theta} = 29.5$.

For the first case, the final piston velocity is set to $u_p = 1410$ m/s and the dimensionless activation energy is $\bar{\Theta} = 29.5$. Plots of the pressure versus time are shown in

Fig. 7.10 for the (a) ideal gas and (b) van der Waals gas. The maximum and minimum pressure values are slightly lower for the van der Waals gas, an expected effect of the correction for inter-molecular attraction in the van der Waals model. The DFT for the ideal gas and van der Waals gas, respectively, are shown in Fig. 7.11. Plotted on a log-log scale, the DFT provides a clearer picture of the dominant frequencies in the signal. For this case, the signals are very similar, with the first harmonic at the same frequency of 1.499 MHz. The amplitude at this frequency is 5.237 MPa for the ideal gas and 5.536 MPa for the van der Waals gas. The second harmonic is at 2.899 MHz and 0.613 MPa for the ideal gas and 2.799 MHz and 0.803 MPa for the van der Waals gas. Each of these harmonics has a larger amplitude for the van der Waals gas, indicating that there is more energy in these modes. Additionally, the second harmonic for the ideal gas is at a slightly higher frequency. Although this case is very similar for both models, the van der Waals model has diminished the energy in higher frequency modes relative to the ideal gas model. Plotting in the phase plane, the pulsating detonation is evident in the cyclical nature seen in Fig. 7.12. Qualitatively, the behavior in phase space is the same for both cases with primarily single-mode oscillations.

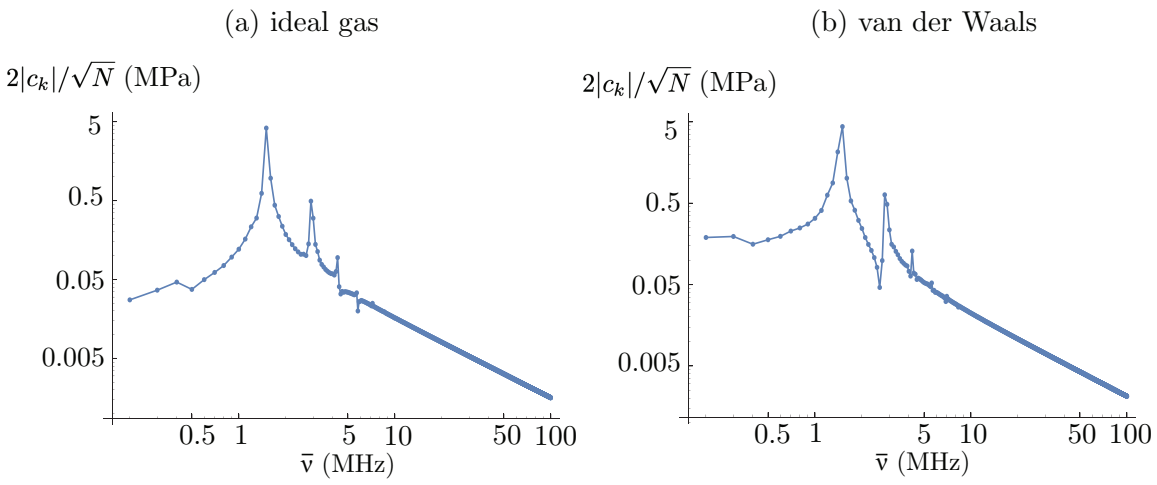

Figure 7.11. DFTs for the detonation instability in an (a) ideal gas and (b) van der Waals gas. The piston velocity is $u_p = 1410$ m/s, and the dimensionless activation energy is $\bar{\Theta} = 29.5$.

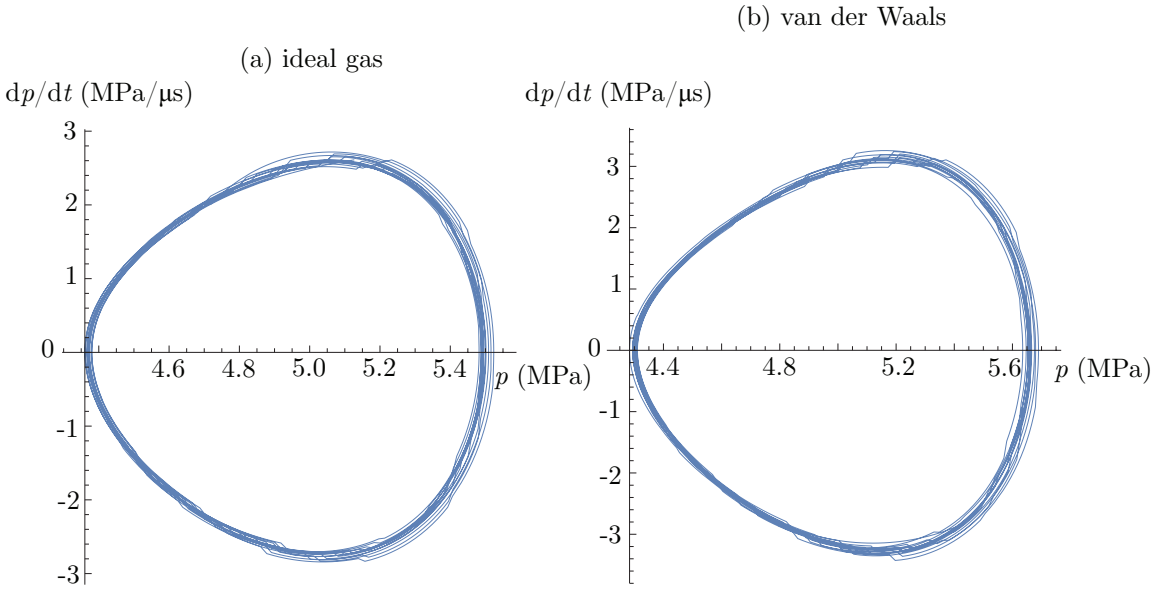

Figure 7.12. Phase plots for the detonation instability in an (a) ideal gas and (b) van der Waals gas. The piston velocity is $u_p = 1410$ m/s, and the dimensionless activation energy is $\bar{\Theta} = 29.5$.

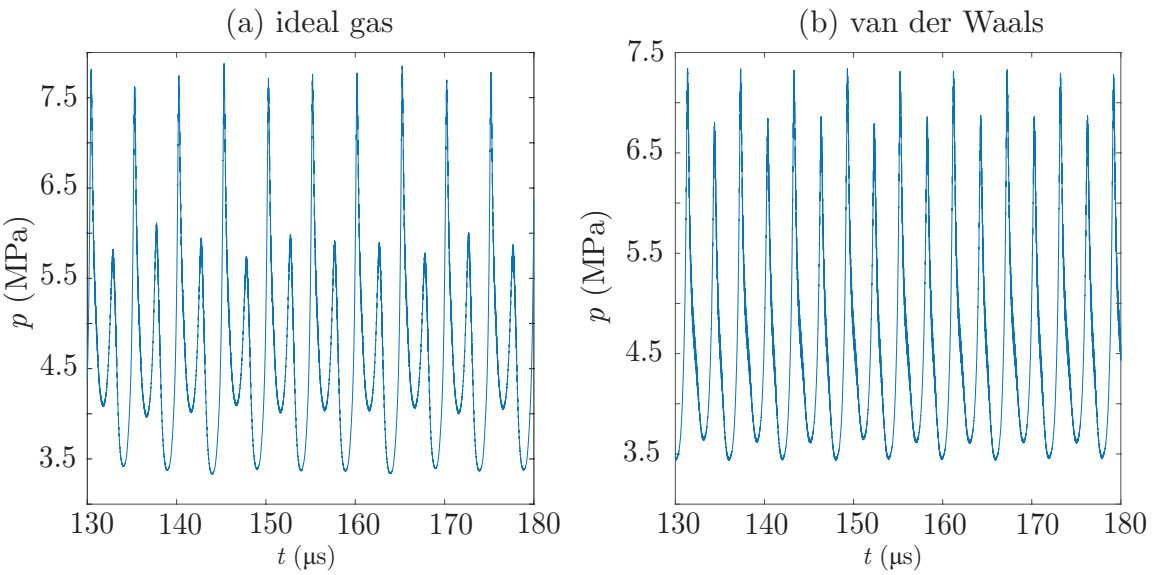

Figure 7.13. Pressure versus time for a two-mode detonation instability in an (a) ideal gas and (b) van der Waals gas. The piston velocity is $u_p = 1250$ m/s, and the dimensionless activation energy is $\bar{\Theta} = 29.5$.

For the second case the piston velocity is decreased to $u_p = 1250$ m/s. The resulting detonation instabilities have additional modes, as seen in Fig. 7.13. For the ideal gas, Fig. 7.13(a), the separation between the harmonic modes with larger and smaller magnitudes is greater, and additional modes are evident in the oscillations of the peaks themselves. This is not the case for the van der Waals gas, Fig. 7.13(b), for which the magnitudes of the peaks remain closer together, and oscillations of the peaks themselves are not as large. This is supported by the DFTs in Fig. 7.14. The ideal gas case, 7.14(a), has active modes at higher frequencies than the van der Waals gas case in 7.14(b). The largest amplitudes are not at the same frequencies, the first significant harmonic for the ideal gas being at 1.299 MHz and 2.013 MPa while for the van der Waals gas this is at 0.899 MHz and 5.739 MPa. Not only is the amplitude

much larger for the van der Waals gas, it is also at a lower frequency mode relative to the ideal gas. The second harmonic, the largest amplitude peak for each case, is at 2.499 MHz and 6.032 MPa for the ideal gas and 1.699 MHz and 6.836 MPa for the van der Waals gas. Again, the van der Waals gas is shown to decrease the energy present in higher frequency modes relative to the ideal gas under otherwise identical conditions. Examining the phase plots in Fig. 7.15, the multiple modes in each case are evident.

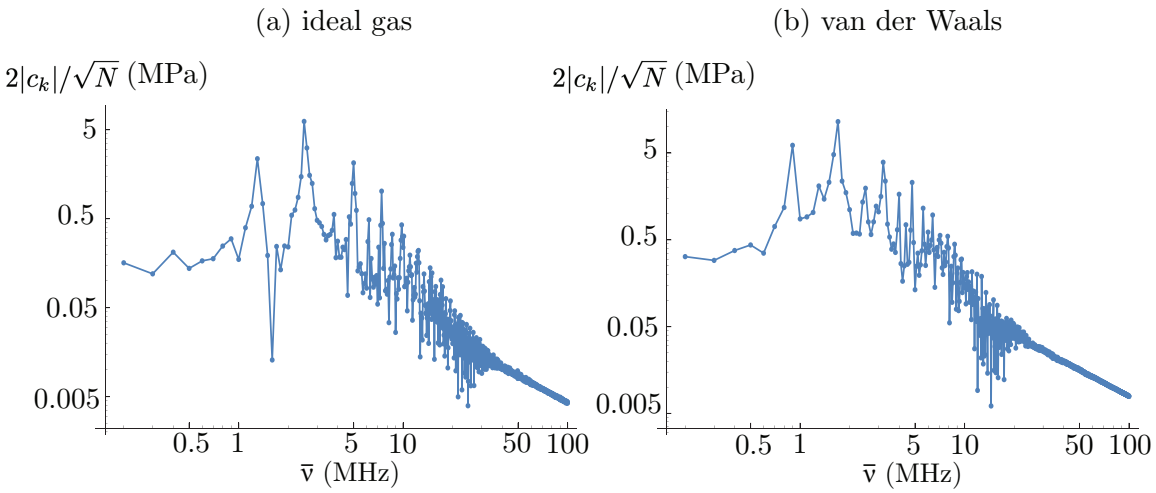

Figure 7.14. DFTs for the detonation instability in an (a) ideal gas and (b) van der Waals gas. The piston velocity is $u_p = 1250$ m/s, and the dimensionless activation energy is $\bar{\Theta} = 29.5$.

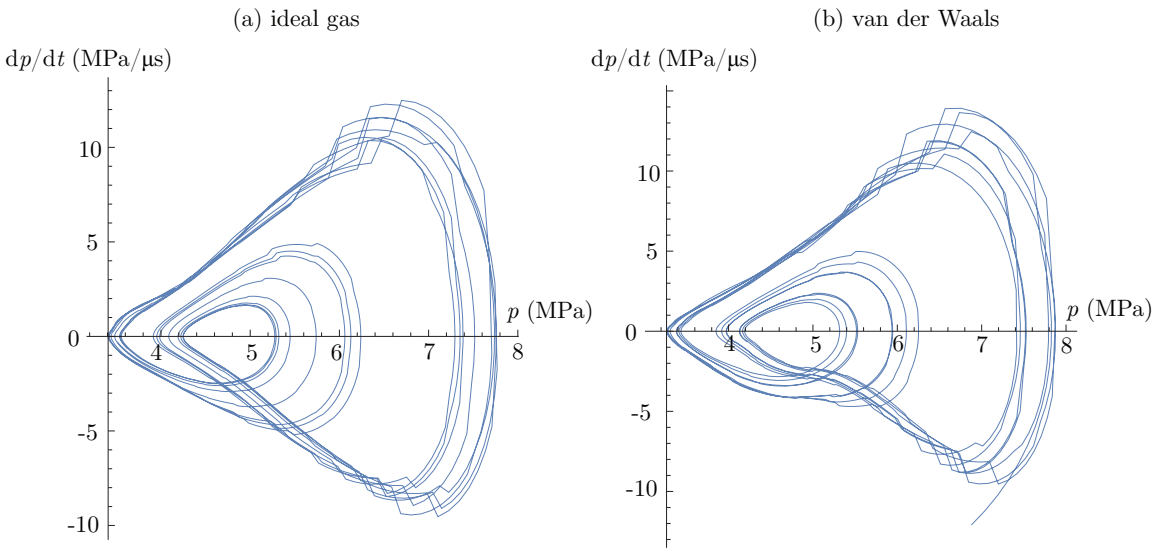

Figure 7.15. Phase plots for the detonation instability in an (a) ideal gas and (b) van der Waals gas. The piston velocity is $u_p = 1250$ m/s, and the dimensionless activation energy is $\bar{\Theta} = 29.5$.

7.3 Verification of Unsteady Dynamics

The DFT will now be used for verification of unsteady detonation dynamics. Setting the activation energy to $\bar{\Theta} = 26$ and the piston velocity to $u_p = 1250$ m/s, the grid size was varied between $\Delta x = [0.1/7000, 0.1/11000]$ m, and the resulting DFTs are given in Fig. 7.16(a)-(e). The magnitudes of the first two harmonics are shown versus the grid size in Fig. 7.16(f). The coarsest grid fails to capture the detonation instability, reflected in the absence of the unstable modes in the DFT. The slightly more fine grid of 7.16(b) captures the first harmonic at roughly the correct frequency, but fails to capture the higher frequency modes. The third grid captures the expected frequencies, along with noticeable numerical noise near the high-frequency modes. This numerical noise is reduced in the two finest grids, which agree well with one another on the dominant frequencies and their magnitudes. A simple convergence study was done, and convergence rates of $r = 1.067$ and $r = 0.947$ were found for the amplitude of the first and second harmonics, respectively.

Figure 7.17(a) shows the frequency values for the first and second harmonics, omitting those for the coarsest grid. The predicted frequencies in each case are near those of the finest grid, although do fluctuate some with increasing grid resolution. Estimates of the wavelength $\bar{\lambda} = (u+c)/\bar{\nu}$ for the frequencies of the first two harmonics are given in Fig. 7.17(b). Figure 7.18(a) and (b) give the dimensionless frequency and wavelength errors, respectively, relative to the finest grid. The relative error has been calculated by

$$\mathcal{E} = \frac{|C_{\Delta x_{min}} - C_{\Delta x_N}|}{C_{\Delta x_{min}}}, \tag{7.2}$$

where C is substituted with the respective quantity for amplitude, frequency, or wavelength, the subscript Δx_{min} indicates the value at the finest grid, and Δx_N the value for a grid with N gridpoints. This simple example illustrates the increasing demand on the grid resolution introduced by oscillatory behavior of unstable detonations.

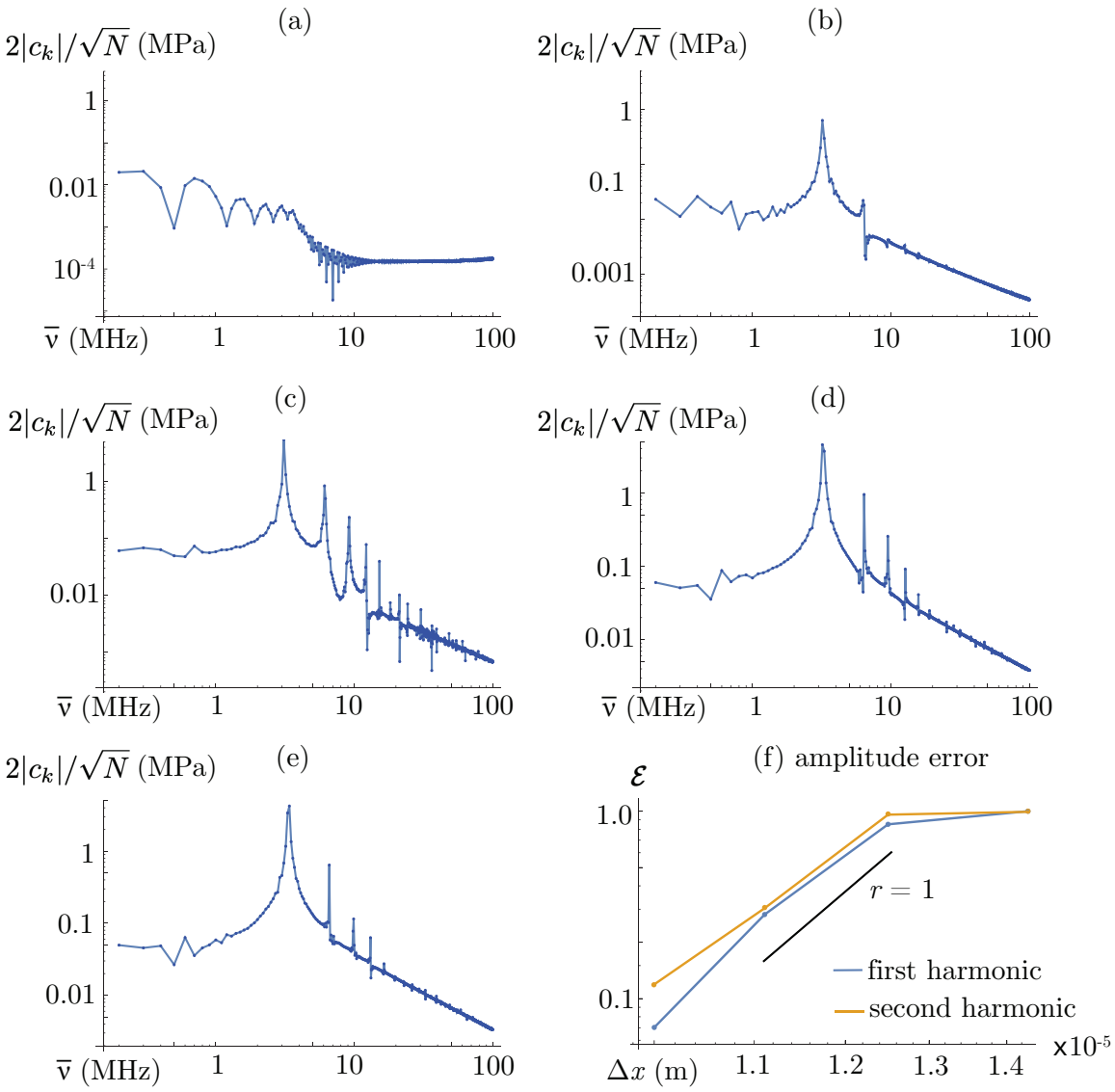

Figure 7.16. DFTs for detonation instability in a van der Waals gas with varying grid resolution: (a) $\Delta x = 0.1/7000$ m, (b) $\Delta x = 0.1/8000$ m, (c) $\Delta x = 0.1/9000$ m, (d) $\Delta x = 0.1/10000$ m, (e) $\Delta x = 0.1/11000$ m. The dimensionless error, relative to the finest grid, in the magnitude of the first and second peaks for each other Δx value are plotted in (f). In the convergent regime, the convergence rates for the first and second peak are $r = 1.067$ and $r = 0.947$, respectively. The piston velocity is $u_p = 1250$ m/s, and the dimensionless activation energy is $\bar{\Theta} = 26$.

Using ZND analysis, the half reaction zone thickness is found to be on the order of 10^{-3} m; however, the lowest frequency oscillations, and thus longest wavelengths, are on the order of 10^{-4} m. It is possible to simultaneously have a fine enough grid to capture the steady reaction zone, but too coarse of a grid to capture the oscillations of an unstable detonation. The half reaction time can be estimated by dividing the half reaction length by the characteristic speed $u+c$, and for this case is on the order of 10^{-7} s; this is consistent with estimates of the half reaction time performed with solving for a spatially homogeneous reaction with the same parameters. For the cases presented, the time step has been fixed at 2×10^{-10} s.

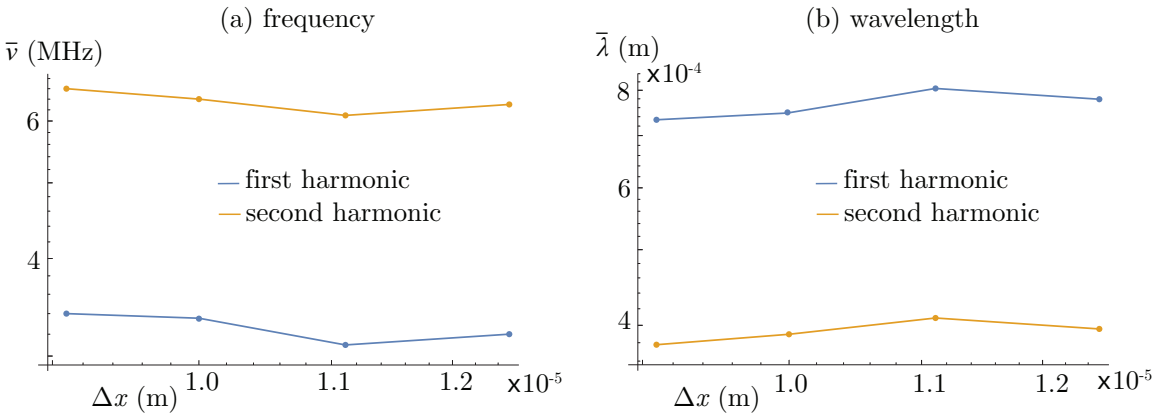

Figure 7.17. (a) Frequency of the first two harmonics for detonation instability in a van der Waals gas with varying grid resolution. The coarsest grid, corresponding to the DFT in Fig. 7.16(a), is omitted, as there are no clear peak amplitudes among the Fourier modes. (b) Estimates of the wavelength of the first two harmonics of the DFT. The piston velocity is $u_p = 1250$ m/s, and the dimensionless activation energy is $\bar{\Theta} = 26$.

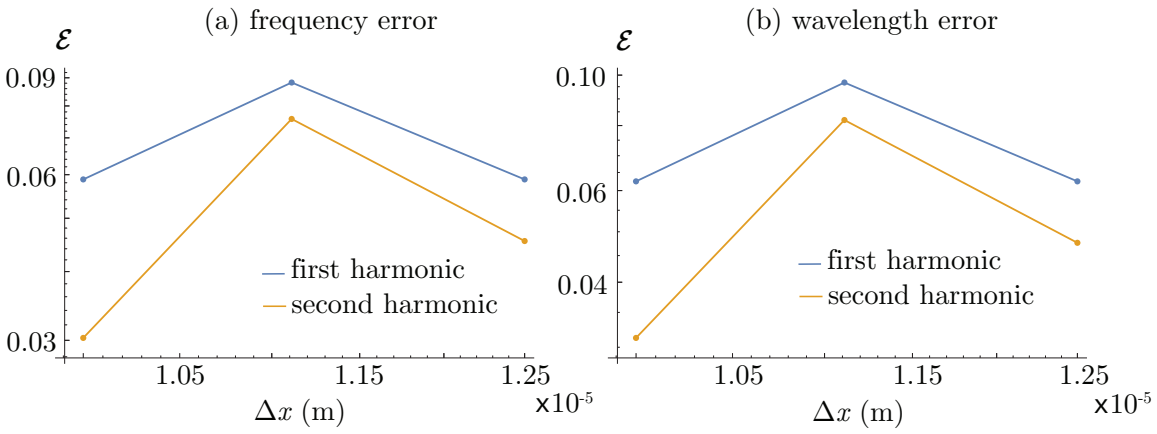

Figure 7.18. (a) Dimensionless frequency error of the first two harmonics for detonation instability in a van der Waals gas with varying grid resolution. The coarsest grid, corresponding to the DFT in Fig. 7.16(a), is omitted, as there are no clear peak amplitudes among the Fourier modes. (b) Dimensionless wavelength error of the first two harmonics of the DFT. The piston velocity is $u_p = 1250$ m/s, and the dimensionless activation energy is $\bar{\Theta} = 26$.

7.4 Stability Limit

Bifurcation diagrams were constructed for a qualitative comparison of the transition to instability as the activation energy is increased. The piston problem was set with the parameters in Table 6.1 and a final piston velocity of $u_p = 1410$ m/s. Bifurcation diagrams are shown in Fig. 7.19(a) and (b) for the ideal gas and van der Waals equations of state, respectively. The first bifurcation point transitions from stable detonation to a single-mode instability. This transition occurs at a higher activation energy for the van der Waals gas. The second transition point occurs when the single-mode instability transitions to a two-mode instability; again this transition occurs at a higher activation energy for the van der Waals gas. This is in agreement with the previous section, where it was shown that for identical piston velocity and activation energy, unstable detonations in the van der Waals gas have higher energy in lower frequency modes relative to the ideal gas. This is consistent with the physical effects that the van der Waals model attempts to capture. Adjustments for attractive forces and excluded volume result in decreased pressure relative to the ideal gas. Additionally, for the same piston velocity the wave speed is slightly slower.

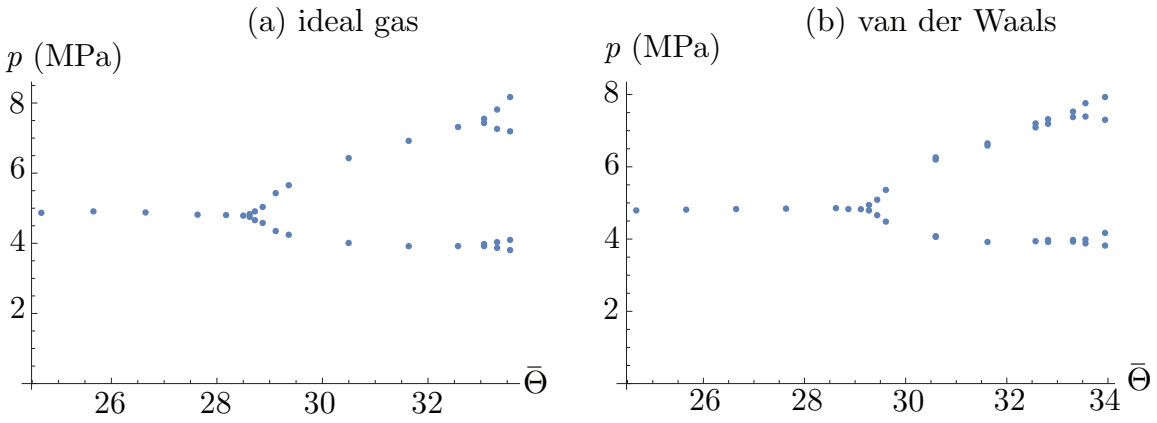

Figure 7.19. Bifurcation diagram of maximum detonation pressure as activation energy is varied for (a) an ideal gas and (b) a van der Waals gas.

CHAPTER 8

DISCUSSION AND CONCLUSIONS

In this work we have performed an extensive analysis of the relationship between inert shock dynamics and detonation dynamics in a van der Waals gas. Anomalous wave dynamics have been explored in inviscid and viscous inert gases, and used to determine the effect of anomalous waves on the understanding of classical detonation theory. The inert models present a comprehensive solution verification of anomalous waves for numerical methods with the goal of ensuring that anomalous behavior is predicted correctly. This becomes increasingly important if reaction is included, as much of the fundamental analysis of steady detonations relies on jump analysis, which becomes complicated in the presence of anomalous waves. Verification of limit cycles in unsteady detonations has also been done with the use of DFTs, demonstrating the demands on grid resolution imposed by the wavelengths associated with the active frequencies.

First, analysis of classical and anomalous steady wave dynamics was performed for the inert van der Waals gas. Solutions for inviscid compression and rarefaction shock discontinuities required a straightforward application of the Rankine-Hugoniot jump conditions with the van der Waals equation of state. It is shown that the jump analysis may admit multiple solutions that satisfy the second law of thermodynamics, including solutions for both a rarefaction and compression shock. As a consequence of the second law, examination of the Mach number shows that the expected transition from supersonic to subsonic is achieved by both possible solutions. Conventional thermodynamics may tell us to take the compression shock as the physical solution.

However, this particular region highlights the importance of the viscous predictions, as the addition of physical viscosity allows for a relaxation to one of multiple viable weak solutions predicted by the Rankine-Hugoniot jump equations. Initialization of unsteady numerical codes with the potential compression shock solution reveals it to be unstable, disintegrating into a smooth compression fan. Care must be taken when solving for shock solutions near or in the predicted anomalous, or BZT, region, to be certain of what type of discontinuity, compression or rarefaction, is expected.

Analysis of the inert system continued with unsteady wave dynamics, including continuous waves and shock tube solutions. An exact solution for conventional and anomalous waves in compressible inviscid non-ideal gas flows modeled with the van der Waals equation of state has been presented, adapted from existing analytical solutions. Homeoentropic wave solutions with a van der Waals equation of state require an adjustment to the solution procedure for an ideal gas. The more complex van der Waals equation requires a numerical quadrature to achieve an analytical solution for the change in density with respect to the particle velocity across a homeoentropic wave. The solution procedure presented here is valid for both continuous compressions and continuous rarefactions, as well as forward and backward facing waves.

Analytical solutions of shock tube flows in inviscid van der Waals gases operated in both the classical and anomalous regions of state space were produced using the individual exact solutions for shock jumps and homeoentropic waves. For the viscous case, numerical simulations were performed with the same three sets of initial conditions, one each in the classical, anomalous, and mixed regions. In the convex region, classical behavior characterized the propagation of each wave structure. In the non-convex region, anomalous behavior was demonstrated. This region admitted the existence of rarefaction shock waves and compression fans as a result of reversals in the speed of sound's relation to the state variables. These anomalous wave structures satisfy the second law of thermodynamics. The mixed convexity regime

demonstrated a combination of the two regions. For the result presented, a composite wave containing a shock discontinuity and continuous compression were present as a result of the non-monotonicity of the sound speed across the shock. Analysis of the composite shock structure determines that for a shock connecting the initial and final states, the Mach number at the initial state would be subsonic. This indicates that a single shock discontinuity between the two points cannot induce a transition from supersonic to subsonic as required by compressible fluid dynamics.

In the mixed convexity case, the WENO5M method must be supplemented with a global flux-splitting scheme, as the local scheme fails for the stencils where the sound speed is non-monotonic. A convergence study was performed for the WENO5M method to the exact Sod shock tube solution for an inviscid van der Waals gas. The method successfully predicts the shock tube operated in the anomalous region, and converges at a rate slightly less than one, behavior expected of a shock-capturing method with a system containing discontinuities.

Expanding the inviscid model to include reaction, fundamental aspects of detonation dynamics were explored with a van der Waals gas. Rayleigh line and Hugoniot curve analysis was performed first with a simple addition of van der Waals parameters to a classical ideal gas problem. The van der Waals corrections induce small changes, including decreasing the equilibrium pressure and a corresponding increase in the CJ speed. The decreased pressure relative to the ideal gas is an expected consequence of the van der Waals model's consideration of attractive forces between molecules. The attractive forces cause molecules to coalesce, and if the volume is fixed, this translates to a decrease in the pressure. The decreased pressure corresponds to a decreased temperature, decreasing the reaction rate for the one-step model used. As a consequence, the minimum wave speed for a detonation is increased relative to the ideal gas for the van der Waals model in order to provide the required energy for the reaction to complete.

The problem parameters used in the inert case were adjusted to create a model fluid with reaction in the anomalous region. Analysis remained the same as expected for the initial condition placed in the convex region as in the classical case. Moving the initial conditions into the anomalous region it was shown that for a high enough value of the heat release the Rayleigh line and Hugoniot curve analysis remains the same as in the classical case. The heat release shifts the Hugoniot curve far enough that the CJ speed Rayleigh line has no additional intersections with the inert Hugoniot curve. The behavior of the Mach number is consistent with the classical case, inducing a transition from supersonic to subsonic across the shock before settling to the equilibrium state; the Mach number at the CJ point is one.

Decreasing the heat release decreases the shift in the Hugoniot curves throughout the reaction, and the Rayleigh line at the CJ speed intersects the inert Hugoniot at an intermediate point. Such an inert intersection point renders the initial shock solution inadmissible as there is no dissipative shock structure. Additionally, the Mach number at the initial state with the CJ speed is subsonic, indicating that a shock solution does not exist to connect the initial state and the CJ point. This is the first indication that traditional steady detonation dynamics analysis may fail in the presence of anomalous regions.

The analysis of steady reaction dynamics was continued with examination of the pressure evolution through a reaction. Intermediate crossings of the Hugoniot curve introduced unusual behavior in the relation between pressure and reaction progress. If the CJ speed Rayleigh line remained under the inert Hugoniot curve, no path existed between the initial state and the CJ point without going into negative values of the reaction progress. Such negative values have no physical meaning. Additionally, the path from the initial state to the weak solution is non-convex, which while not explored further here, is a potential avenue for future work. Standard ZND solutions rely on the validity of the Rankine-Hugoniot jump equations; however, it was shown

that in the anomalous region such solutions may be rendered invalid by intermediate crossings of the Hugoniot curve. For large enough shock speeds, an initial condition in the anomalous region may have a valid discontinuous shock solution and ZND structure.

Finally, unsteady detonation dynamics with the van der Waals equation of state were studied. The dynamics of unsteady transition to a long time stable steady detonation behind anomalous waves were explored. For initial conditions in the anomalous region with sufficiently large shock speeds, a classical compression shock forms, and classical detonation dynamics are predicted. If the driving shock is an anomalous composite compression, the structure of the resulting detonation depends upon where in the composite wave the reaction occurs. For reaction occurring in the smooth compression, the composite wave is split by the increase in velocity in the compression fan induced by the reaction. If reaction does not occur until the entire composite wave has passed, a traditional von Neumann spike is predicted behind the discontinuous shock. The leading compression fan remains, and is unsteady as it continues to spread as the wave travels, while the trailing discontinuous shock is steady, allowing for a pseudo-steady analysis. Transforming the wave to the frame where the discontinuity is steady, the Mach number begins in the subsonic regime, undergoes a transition to supersonic just before the shock, and is then shocked into the subsonic regime. This is consistent with the expected behavior of the Mach number throughout a composite wave.

Effects on unstable detonation dynamics of the van der Waals equation of state were examined when compared to the ideal gas solutions. Examples of unstable detonations were shown at two different activation energies. Phase plots illustrated the limit cycle behavior of the peak pressure over time, and DFTs highlighted the dominant frequencies in the signals. A simple verification study of unsteady detonation dynamics in a van der Waals gas was done using DFTs for various spatial grids. It

was shown that as the grid spacing is decreased, higher frequency harmonic modes are resolved by the DFT. Analysis revealed that the longest wavelengths were smaller than the half reaction zone length. As a result, it is possible to have a grid size that captures the reaction zone, but is not fine enough to capture the oscillations that may be associated with an unsteady detonation. A bifurcation study showed that for a set piston velocity the transition to instability and the split from one to two modes occurred at a higher activation energy for the van der Waals gas. This can be contributed to the decreased pressures in a van der Waals gas as a result of the attractive forces between molecules. For a set volume, the resulting effect of the "clumping" is to decrease the pressure, resulting in decreased pressure jumps across a shock. Additionally, the shock speed corresponding to the same piston velocity is decreased for a van der Waals gas.

This work has brought together the study of non-ideal gases, anomalous waves, and detonation dynamics by considering how the fundamental physics of each build upon one another. Anomalous wave dynamics have seen careful study by many authors, including Cramer's detailed analysis of shock splitting and composite waves [32], the comprehensive analysis of shock formation in real gases by Menikoff and Plohr [83], and detailed molecular analysis of anomalous gas dynamics by Colonna and Guardone [25]. However, none of these works considered how anomalous wave dynamics would affect, and be affected by, the presence of reaction. To do so required understanding of fundamental detonation dynamics. The foundation of detonation dynamics is formed by the CJ and ZND theories, both of which are based upon shock dynamics. Detonation dynamics in an ideal gas have been presented in detail by authors such as Fickett and Davis [52] and Lee [77]. Although some authors have considered detonation properties of non-ideal gases, such as Schmitt and Butler [107] and Dumazer, et al. [42], none have considered detonation dynamics when anomalous waves are expected. This work has taken the initial steps to bridge that gap,

evaluating CJ and ZND theories in the anomalous region, and exploring predictions of detonations driven by anomalous waves.

There are several areas of interest for future extension of this work. One area is a more robust verification of unsteady detonation dynamics in a van der Waals gas. The simple verification study done here illustrates that as the grid size is varied, the numerical solution may capture only some, or none, of the limit cycle behavior that may be associated with an unsteady detonation. Resolution of higher frequency modes will require a finer grid, based on the wavelengths associated with those frequencies. Another area of interest is detonation instabilities behind anomalous waves. For detonations behind anomalous waves, the unsteady nature of the leading part of the composite wave introduces additional complications to the potential interaction of a detonation instability and an anomalous composite shock structure. Care must be taken to distinguish affects from the detonation instability and the anomalous wave itself, as it is uncertain what effect the cyclical increase and decrease of the shock speed may have on the transition point between the continuous and discontinuous compressions. It is possible that the perturbations of the unstable detonation may affect the leading compression fan. Careful consideration of the shock structure will be necessary to distinguish predictions relating to the detonation instability or anomalous behavior. Finally, the extension to a viscous van der Waals gas would continue to develop the understanding of real gas effects on detonation dynamics, with both classical and anomalous waves considered.

APPENDIX A

VAN DER WAALS EQUATION OF STATE WITH VARIABLE SPECIFIC HEAT

The region of anomalous wave behavior in the gas phase is typically very near the critical point, and it is possible that the specific heat at constant volume c_v may vary significantly in this region. A variable c_v was considered for the inert portions of this work, but it was found for the choice of material parameters used variable c_v did not have a significant effect on key results. The anomalous region encompasses a small range of temperatures, and the corresponding variations in c_v are small. The relevant analysis for the van der Waals model with variable specific heat at constant volume are included here for completeness.

A.1 Mathematical Model

As detailed in [59], in the neighborhood of the critical point c_v can be approximated by the power law

$$c_v(T) = c^c_{v\infty}\left(\frac{T}{T_c}\right)^m. \tag{A.1}$$

The parameters m and $c^c_{v\infty}$ are dependent upon the fluid, and can be found for a number of anomalous fluids in [79]. For a van der Waals gas with variable specific heat at constant volume, the caloric and thermal state equations are

$$e(\rho,T) = \frac{c^c_{v\infty}T}{(m+1)}\left(\frac{T}{T_c}\right)^m - a\rho, \tag{A.2}$$

$$p(\rho,T) = \frac{\rho RT}{1-\rho b} - a\rho^2, \tag{A.3}$$

where R is the particular gas constant. The van der Waals constants a and b are defined by $a = 27R^2T_c^2/64/p_c$ and $b = RT_c/8/p_c$ and constants T_c and p_c are the critical temperature and pressure, respectively. The critical density is then predicted by the van der Waals model using Eq. A.3. The frozen sound speed is

$$c^2 = \left.\frac{\partial p}{\partial \rho}\right|_s = \frac{RT}{(1-b/v)^2}\left(1 + \frac{R}{c_{v\infty}^c}\left(\frac{T_c}{T}\right)^m\right) - \frac{2a}{v}, \tag{A.4}$$

where the specific volume v has been substituted for density with $v = 1/\rho$. For the inert case, the specific entropy, given here as a dimensionless difference, is

$$\frac{s - s_o}{c_{v\infty}^c} = \frac{1}{m}\left(\left(\frac{T}{T_c}\right)^m - \left(\frac{T_o}{T_c}\right)^m\right) + \frac{R}{c_{v\infty}^c}\ln\left(\frac{v-b}{v_o-b}\right), \tag{A.5}$$

with reference parameters s_o, T_o, and v_o.

Using Eqs. (4.11, A.3, A.4, A.5), we can write the fundamental derivative for a van der Waals gas as

$$\mathcal{G}(v,s) = \frac{v^3}{2c^2}\left(-\frac{6a}{v^4} + \frac{R}{(v-b)^3}\left(\frac{mT_c^m}{c_{v\infty}^c}\left(s - s_o - R\ln\left(\frac{v-b}{v_o-b}\right)\right)\right)^{\frac{1}{m}}\right. \tag{A.6}$$
$$\left.\left(2 + \frac{R\left(R - mR + 3m(s-s_o) - 3mR\ln\left(\frac{b-v}{b-v_o}\right)\right)}{m^2\left(s_o - s + R\ln\left(\frac{b-v}{b-v_o}\right)\right)^2}\right)\right).$$

A.2 Continuous Wave Solutions

The analytical solution procedure for continuous homeoentropic waves is applicable for variable $c_v(T)$, requiring only the appropriate adjustments to the equation for $c(\rho)$ and the isentropic relations. For the van der Waals equation of state with

variable $c_v(T)$, the sound speed in a homeoentropic material is given by

$$c(\rho) = \sqrt{\frac{R\left(m\ln\left(\frac{\frac{1}{\rho}-b}{\frac{1}{\rho_o}-b}\right)-\kappa m-1\right)\left(\frac{mRT_c^m}{c_{v\infty}^c}\left(\kappa-\ln\left(\frac{\frac{1}{\rho}-b}{\frac{1}{\rho_o}-b}\right)\right)\right)^{1/m}}{m(b\rho-1)^2\left(\ln\left(\frac{\frac{1}{\rho}-b}{\frac{1}{\rho_o}-b}\right)-\kappa\right)}} - 2a\rho, \quad \text{(A.7)}$$

where the constant $\kappa = (c_{v\infty}^c/R/m)(T_o/T_c)^m$ is dimensionless.

Homeoentropic relations for the van der Waals equation of state can be used to find the solutions for other quantities, including the temperature

$$\frac{T_2}{T_1} = \left(1-\left(\frac{T_c}{T_1}\right)^m \frac{Rm}{c_{v\infty}^c}\ln\left(\frac{v_2-b}{v_1-b}\right)\right)^{1/m}, \quad \text{(A.8)}$$

and pressure

$$p_2 = \left(p_1+\frac{a}{v_1^2}\right)\left(\frac{v_2-b}{v_1-b}\right)\left(1-\left(\frac{T_c}{T_1}\right)^m \frac{Rm}{c_{v\infty}^c}\ln\left(\frac{v_2-b}{v_1-b}\right)\right)^{1/m} - \frac{a}{v_2^2}. \quad \text{(A.9)}$$

APPENDIX B

ANALYTICAL SOLUTION OF VISCOUS SHOCKS

A detailed derivation is presented here of the analytical solution for a steady viscous shock in a calorically perfect ideal gas with constant viscosity and thermal conductivity. The Prandtl number $Pr = 3/4$ is constant, and the derivation follows closely that given by Ghia, et al. [56] and Powers [96]. The inclusion of viscous terms allows us to write the governing equations in a combination of conservative and non-conservative form, which will prove to be convenient. It will also be convenient to rewrite Eqs (2.1) and (2.3) in the steady state limit, and take the steady state limit of the non-conservative linear momentum equation. A Galilean transformation is used to cast the system in the wave's reference frame, for which $x \to \hat{x}(x,t)$ and $t \to \hat{t}(x,t)$ with $\hat{x} = x - Ut$, $\hat{t} = t$, and the speed of the shock wave U. The transformed system of equations is now

$$\frac{d}{d\hat{x}}(\rho\hat{u}) = 0, \tag{B.1}$$

$$\rho\hat{u}\frac{d\hat{u}}{d\hat{x}} + \frac{dp}{d\hat{x}} - \frac{d\tau}{d\hat{x}} = 0, \tag{B.2}$$

$$\frac{d}{d\hat{x}}\left(\rho\hat{u}\left(h + \frac{\hat{u}^2}{2}\right)\right) - \frac{d}{d\hat{x}}(\tau\hat{u} - q) = 0, \tag{B.3}$$

$$p = \rho RT, \quad h = c_p T, \quad e = h - \frac{p}{\rho}, \tag{B.4a-c}$$

$$q = -k\frac{\partial T}{\partial \hat{x}}, \quad \tau = \frac{4}{3}\mu\frac{\partial \hat{u}}{\partial \hat{x}}. \tag{B.4d,e}$$

Variables and parameters are as previously introduced, with the addition of the specific enthalpy h. Along the domain, as $\hat{x} \to -\infty$, a number of quantities approach

positive constant values: $p \to p_1$, $T \to T_1$, $\hat{u} \to \hat{u}_1$, $q \to 0$, $\tau \to 0$, $\rho_1 = p_1/R/T_1$, and $h_1 = c_p T_1$. Additionally, all variables are required to be bounded for $\hat{x} \in (-\infty, \infty)$.

Our first step will be to put together an expression for the shocked particle velocity, $\hat{u}_2$. We start by simplifying the energy equation using Eqs. (B.4d,e) and the Prandtl number by

$$\frac{d}{d\hat{x}}\left(\rho\hat{u}\left(h+\frac{\hat{u}^2}{2}\right)\right) - \frac{d}{d\hat{x}}\left(\underbrace{\frac{4}{3}\mu\frac{d\hat{u}}{d\hat{x}}}_{\tau}\hat{u} + \underbrace{k\frac{dT}{d\hat{x}}}_{-q}\right) = 0, \tag{B.5}$$

$$\frac{d}{d\hat{x}}\left(\rho\hat{u}\left(h+\frac{\hat{u}^2}{2}\right)\right) - \frac{d}{d\hat{x}}\left(\frac{4}{3}\mu\frac{d\hat{u}}{d\hat{x}}\hat{u} + \frac{\mu c_p}{Pr}\frac{dT}{d\hat{x}}\right) = 0, \tag{B.6}$$

then with Eq. (B.4b), taking $Pr = 3/4$, and absorbing $\hat{u}$ in the derivative operator to reach

$$\frac{d}{d\hat{x}}\left(\rho\hat{u}\left(h+\frac{\hat{u}^2}{2}\right)\right) - \frac{d}{d\hat{x}}\left(\frac{4}{3}\mu\frac{d}{d\hat{x}}\left(\frac{\hat{u}^2}{2}\right) + \frac{4}{3}\mu\frac{dh}{d\hat{x}}\right) = 0. \tag{B.7}$$

Integrating the mass equation, Eq. (B.1), and applying the boundary conditions as $\hat{x} \to -\infty$ of $\rho = \rho_1$ and $\hat{u} = \hat{u}_1$ gives

$$\rho\hat{u} = \rho_1\hat{u}_1. \tag{B.8}$$

This, along with assuming constant μ, can be used to simplify Eq. (B.7) to

$$\rho_1\hat{u}_1\frac{d}{d\hat{x}}\left(h+\frac{\hat{u}^2}{2}\right) - \frac{4}{3}\mu\frac{d^2}{d\hat{x}^2}\left(h+\frac{\hat{u}^2}{2}\right) = 0. \tag{B.9}$$

Integrating once and rearranging gives

$$\frac{d}{d\hat{x}}\left(h+\frac{\hat{u}^2}{2}\right) = -\frac{3C_1}{4\mu} + \frac{3\rho_1\hat{u}_1}{4\mu}\left(h+\frac{\hat{u}^2}{2}\right), \tag{B.10}$$

where C_1 is a constant of integration. Solving the linear, first-order differential equa-

tion yields

$$h + \frac{\hat{u}^2}{2} = \frac{C_1}{\rho_1 \hat{u}_1} + C_2 \exp\left(\frac{3\rho_1 \hat{u}_1 \hat{x}}{4\mu}\right), \tag{B.11}$$

introducing another constant C_2. To prevent unbounded growth as $\hat{x} \to \infty$, C_2 must be zero. In order to satisfy the boundary condition as $\hat{x} \to -\infty$, C_1 must be $C_1 = \rho_1 \hat{u}_1 (h + \hat{u}_1^2/2)$, and we reach

$$h + \frac{\hat{u}^2}{2} = h_1 + \frac{\hat{u}_1^2}{2}. \tag{B.12}$$

Applying Eq. (B.4b) to Eq. (B.12) gives

$$T = T_1 + \frac{\hat{u}_1^2 - \hat{u}^2}{2c_p}. \tag{B.13}$$

This gives us one of the equations we require for our expression for the shocked particle velocity $\hat{u}_2$.

Recalling and rearranging the integrated mass equation, Eq. (B.8) to $\rho = \rho_1 \hat{u}_1 / \hat{u}$, along with the momentum equation, Eq. (B.2) can be rewritten as

$$\frac{d}{d\hat{x}}\left(\rho_1 \hat{u}_1 \hat{u} + p - \frac{4}{3}\mu \frac{d\hat{u}}{d\hat{x}}\right) = 0. \tag{B.14}$$

Integrating and applying the boundary conditions as $\hat{x} \to -\infty$ yields

$$\rho_1 \hat{u}_1 \hat{u} + p - \frac{4}{3}\mu \frac{d\hat{u}}{d\hat{x}} = \rho_1 \hat{u}_1^2 + p_1. \tag{B.15}$$

Substituting for ρ with the ideal gas law in Eq. (B.4a), along with Eqs. B.8) and

(B.13 gives

$$\rho_1\hat{u}_1\hat{u} + \underbrace{\left(\underbrace{\frac{\rho_1\hat{u}_1}{\hat{u}}}_{\rho}\right) R \left(\underbrace{T_1 + \frac{\hat{u}_1^2 - \hat{u}^2}{2c_p}}_{T}\right)}_{p} - \frac{4}{3}\mu\frac{d\hat{u}}{d\hat{x}} = \rho_1\hat{u}_1^2 + p_1. \tag{B.16}$$

Solving for $d\hat{u}/d\hat{x}$, the linear momentum equation may be rewritten as

$$\frac{d\hat{u}}{d\hat{x}} = -\frac{3(\gamma+1)\rho_1\hat{u}_1}{8\gamma\mu}\frac{(\hat{u}_1 - \hat{u})(\hat{u} - \hat{u}_2)}{\hat{u}}. \tag{B.17}$$

We can now express the shocked value for the velocity, given by $\hat{u}_2$ as

$$\hat{u}_2 = \hat{u}_1\frac{\gamma-1}{\gamma+1}\left(1 + \frac{2}{(\gamma-1)M_1^2}\right), \tag{B.18}$$

where the freestream Mach number M_1 is defined as $M_1^2 = \hat{u}_1^2/(\gamma R T_1)$.

The expression for $\hat{u}_2$ is identical to the shocked particle velocity obtained by solving the inviscid Rankine-Hugoniot jump conditions. Because $\gamma > 1$ for the ideal gas, $\hat{u}_1 > \hat{u}_2$. Within the shock it is expected that $\hat{u}_1 > \hat{u}(\hat{x}) > \hat{u}_2 > 0$, $\rho_1 > 0$, and $\mu > 0$. Because of these inequalities, one can expect from Eq. (B.17) that $d\hat{u}/d\hat{x} < 0$. Equation (B.17) can be rearranged to produce

$$\frac{\mu\hat{u}\,d\hat{u}}{(\hat{u}_1 - \hat{u})(\hat{u} - \hat{u}_2)} = -\frac{3(\gamma+1)\rho_1\hat{u}_1}{8\gamma}d\hat{x}. \tag{B.19}$$

Integrating, one finds

$$\int \frac{\mu\hat{u}\,d\hat{u}}{(\hat{u}_1 - \hat{u})(\hat{u} - \hat{u}_2)} = -\frac{3(\gamma+1)\rho_1\hat{u}_1}{8\gamma}(\hat{x} + C), \tag{B.20}$$

where C is the constant of integration. Note, this solution is invariant under translation. While one could formally apply boundary conditions at infinity, this poses

numerical issues when attempting to plot $\hat{u}(\hat{x})$. To alleviate these, we can select the initial condition as $\hat{u}(\hat{x}_{in}) = \hat{u}_{in}$. The choice of $\hat{x}_{in}$ is arbitrary, but it will be useful to choose $\hat{u}_{in}$ to be close to the unshocked value $\hat{u}_1$. With this in mind, we find after integrating and evaluating C that

$$\frac{\mu\hat{u}_2}{\hat{u}_1-\hat{u}_2}\ln\left(\frac{\hat{u}-\hat{u}_2}{\hat{u}_{in}-\hat{u}_2}\right)-\frac{\mu\hat{u}_1}{\hat{u}_1-\hat{u}_2}\ln\left(\frac{\hat{u}_1-\hat{u}}{\hat{u}_1-\hat{u}_{in}}\right)=-\frac{3(\gamma+1)\rho_1\hat{u}_1}{8\gamma}(\hat{x}-\hat{x}_{in}). \quad \text{(B.21)}$$

This result, when scaled in the same fashion, is identical to [70] in the limit of constant viscosity. One can rearrange Eq. (B.21) to get $\hat{x}(\hat{u})$ as

$$\hat{x}(\hat{u}) = \hat{x}_{in} - \frac{8\gamma\mu}{3(\gamma+1)\rho_1\hat{u}_1}\left(\frac{\hat{u}_2}{\hat{u}_1-\hat{u}_2}\ln\left(\frac{\hat{u}-\hat{u}_2}{\hat{u}_{in}-\hat{u}_2}\right)-\frac{\hat{u}_1}{\hat{u}_1-\hat{u}_2}\ln\left(\frac{\hat{u}_1-\hat{u}}{\hat{u}_1-\hat{u}_{in}}\right)\right), \quad \text{(B.22)}$$

$$= \hat{x}_{in} - \frac{8\gamma\mu}{3(\gamma+1)\rho_1(\hat{u}_1-\hat{u}_2)}\ln\left(\frac{\left(\frac{\hat{u}-\hat{u}_2}{\hat{u}_{in}-\hat{u}_2}\right)^{\frac{\hat{u}_2}{\hat{u}_1}}}{\left(\frac{\hat{u}_1-\hat{u}}{\hat{u}_1-\hat{u}_{in}}\right)}\right).$$

Note, Eq. (B.23a,b) takes on the form $\hat{x}(\hat{u}) = f(\hat{u})$. It is possible to invert f via numerical root-finding to form its inverse, f^{-1}, $\hat{u}(\hat{x}) = f^{-1}(\hat{x})$. Equations for the density, temperature, pressure, and Mach number are recovered as

$$\rho(\hat{x}) = \frac{\rho_1\hat{u}_1}{\hat{u}(\hat{x})}, \quad T(\hat{x}) = T_1 + \frac{\hat{u}_1^2-\hat{u}(\hat{x})^2}{2c_p}, \quad \text{(B.23a,b)}$$

$$p(\hat{x}) = \frac{\rho_1\hat{u}_1}{\hat{u}(\hat{x})}R\left(\underbrace{T_1+\frac{\hat{u}_1^2-\hat{u}(\hat{x})^2}{2c_p}}_{T(\hat{x})}\right), \quad M(\hat{x}) = \frac{\hat{u}(\hat{x})}{\sqrt{\gamma RT(\hat{x})}}. \quad \text{(B.23c,d)}$$

APPENDIX C

DISCRETE FOURIER TRANSFORMATIONS

Decomposing a function or signal into its Fourier modes is a useful exercise that allows description of a signal in terms of frequencies and their corresponding amplitudes. In this work, Discrete Fourier Transformations (DFTs) are used in order to decompose the discrete maximum pressure data associated with an oscillating detonation. The DFT is described in detail in Powers and Sen [98] and is summarized here.

Consider a function $y(x)$, $x \in [x_{min},\, x_{max}]$, $x \in \mathbb{R}^1$, $y \in \mathbb{R}^1$, discretized into N uniformly distributed x_j values for $j = 0,\, \ldots,\, N-1$, and their corresponding y_j values. The discrete analog of the continuous Fourier transformation can be written as

$$y_j = \frac{1}{\sqrt{N}} \sum_{k=0}^{N-1} c_k \exp\left((2\pi i)k\left(\frac{N-1}{N}\right)\left(\frac{x_j - x_{min}}{x_{max} - x_{min}}\right)\right), \qquad j = 0, \ldots, N-1. \tag{C.1}$$

The wavenumber of the individual Fourier modes is k, and c_k relates to their magnitudes. This can be simplified if the values of x_j are uniformly spaced by substituting

$$j = (N-1)\left(\frac{x_j - x_{min}}{x_{max} - x_{min}}\right), \tag{C.2}$$

resulting in

$$y_j = \frac{1}{\sqrt{N}} \sum_{k=0}^{N-1} c_k \exp\left((2\pi i)\frac{kj}{N}\right), \qquad j = 0, \ldots, N-1. \tag{C.3}$$

With some work, the DFT can be defined as the following mapping

$$\mathbf{c} = \mathbf{F}^H \cdot \mathbf{y}, \tag{C.4}$$

where $\mathbf{c}$ is the transformed vector, $\mathbf{y}$ is the original vector, and $\mathbf{F}^H$ is the Hermitian transpose of the matrix $\mathbf{F}$. The matrix $\mathbf{F}$ is defined by

$$\mathbf{F} = \frac{1}{\sqrt{N}} \begin{pmatrix} 1 & 1 & 1 & \cdots & 1 \\ 1 & w & w^2 & \cdots & w^{N-1} \\ 1 & w^2 & w^4 & \cdots & w^{2(N-1)} \\ \vdots & \vdots & \vdots & \vdots & \vdots \\ 1 & w^{N-1} & w^{2(N-1)} & \cdots & w^{(N-1)^2} \end{pmatrix}. \tag{C.5}$$

where $w = \exp(2\pi i/N)$. With this definition, it is easily shown that $\mathbf{F}$ is unitary, which implies that its columns are orthonormal, and that $\mathbf{F}^H = \mathbf{F}^{-1}$.

As an example to illustrate the DFT, consider the continuous function

$$y(x) = 10\sin\left((2\pi)\frac{2x}{3}\right) + 2\sin\left((2\pi)\frac{10x}{3}\right) + \sin\left((2\pi)\frac{100x}{3}\right), \tag{C.6}$$

on the domain $x \in [0,\ 3]$. A plot of this signal is given in Fig. C.1. Rescaling the domain with the transformation $\tilde{x} = x/3$ to take $x \in [0,\ 3]$ to $\tilde{x} \in [0,\ 1]$, the continuous function is then

$$y(\tilde{x}) = 10\sin((2\pi)2\tilde{x}) + 2\sin((2\pi)10\tilde{x}) + \sin((2\pi)100\tilde{x}). \tag{C.7}$$

We now discretely sample this function, and choose N uniformly spaced points $\tilde{x}_j$ at which to sample it. In order to capture the highest wave number components of this signal, a sufficiently large value of N is required. In the transformed domain, the smallest wavelength is $\lambda = 1/100$, and the required number of points is at minimum

$N = 100$ sampling points. However, we will take many more points than this, and choose $N = 523$; this unusual choice is of no consequence.

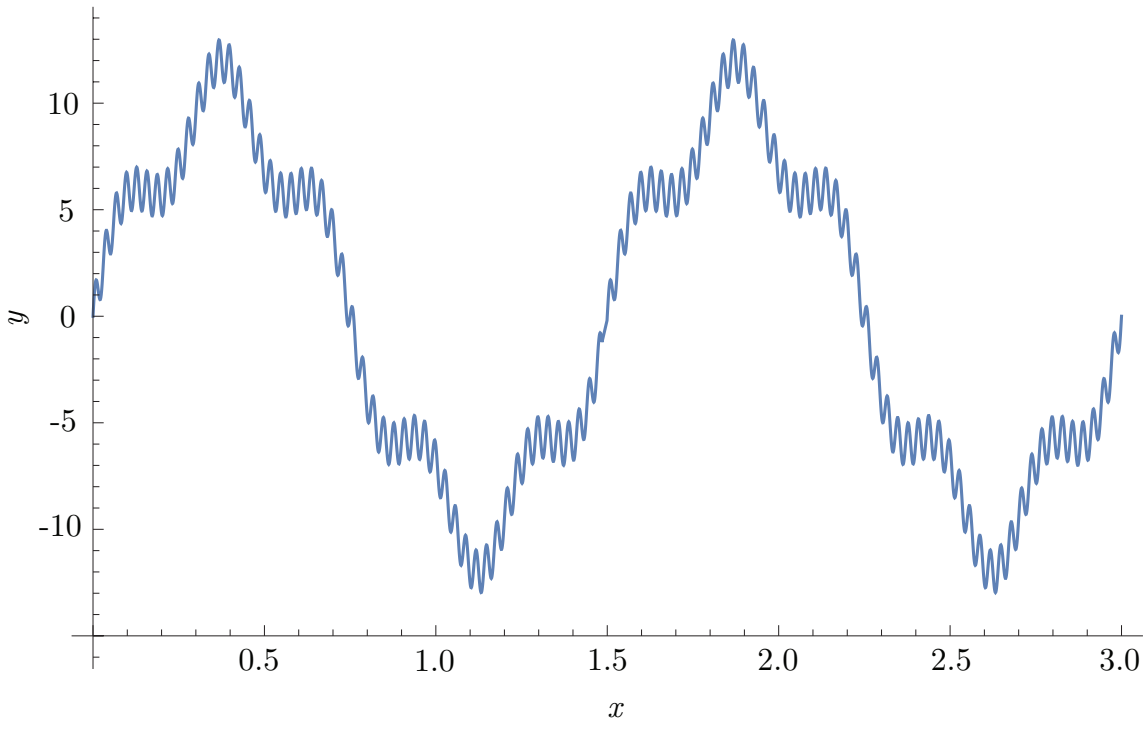

Figure C.1. Plot of the signal function given in Eq. C.6.

The DFT of Eq. (C.6) is given in Fig. C.2(a) as $|c_k|$ vs. k. It is noted that due to aliasing, it is only necessary to plot the first $N/2$ values of $\mathbf{c}$, because the second half is a reflection of the first half of the vector. As it is shown, it is difficult to draw any conclusions from the magnitudes of each value of $\mathbf{c}$, other than to say which wavenumber has the greatest magnitude relative to the others. These wavenumbers can be correlated to the amplitudes associated with them in Eq. C.6, but this is not

particularly useful in cases where the signal being analyzed is data from a numerical simulation rather than from a function. The amplitudes matching each wavenumber in the function can be recovered by scaling the values of $\mathbf{c}$ by a factor of $2/\sqrt{N}$, as shown in Fig. C.2(b). By doing so, the magnitudes of the dominant wavenumbers match exactly those they correspond to in Eq. C.6. This is a more enlightening presentation of the DFT, particularly when there is no function to compare to, but rather a signal represented by a data set.

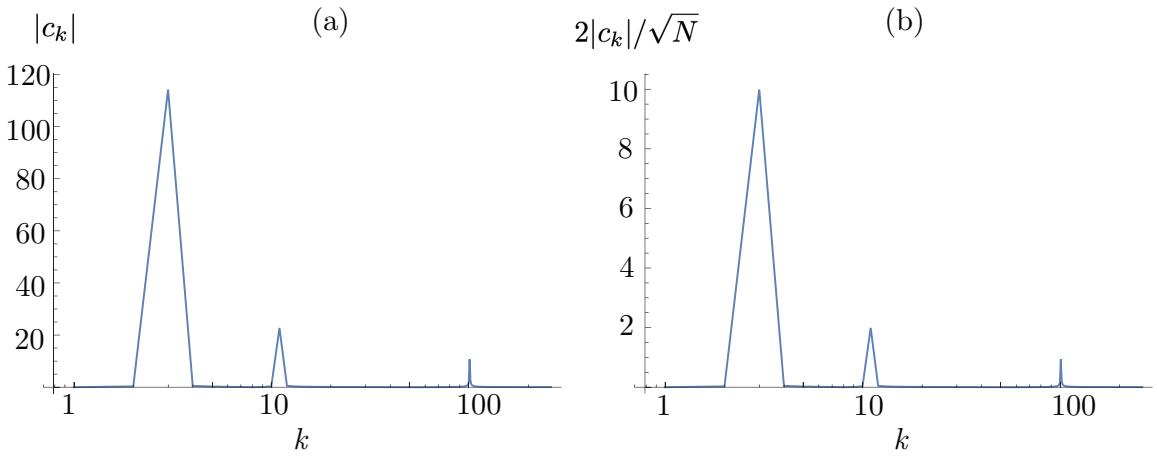

Figure C.2. Plots of the DFT of the signal function given in Eq. C.6. DFT of a discrete set of $N = 523$ points from Eq. (C.6). In (a), the y-axis is given as the magnitudes of each $|c_k|$, and do not match directly with the known magnitudes from the function. In (b), the magnitudes have been scaled by $2/\sqrt{N}$, and now match the corresponding magnitudes of the dominant wavenumbers given in Eq. C.6.

If the value of N is too small, the DFT will not capture the correct amplitudes for all of the wavenumbers present in a signal. Taking $N = 70$, the DFT without

and with scaling are given in Fig. C.3 (a) and (b), respectively. Without the scaling, the amplitudes are smaller than those in Fig. C.2(a), and are primarily useful for analysis of various modes relative to one another. With the scaling, the amplitudes corresponding to the first two terms in Eq. (C.6) are as expected. For the third mode, not only is the amplitude less than the expected value of 1, the wavenumber k is not the correct value of 100. This is because there were not enough points in the discretized domain to fully capture this wavelength. It is also possible to miss a wavelength entirely if there are too few sampling points in a domain.

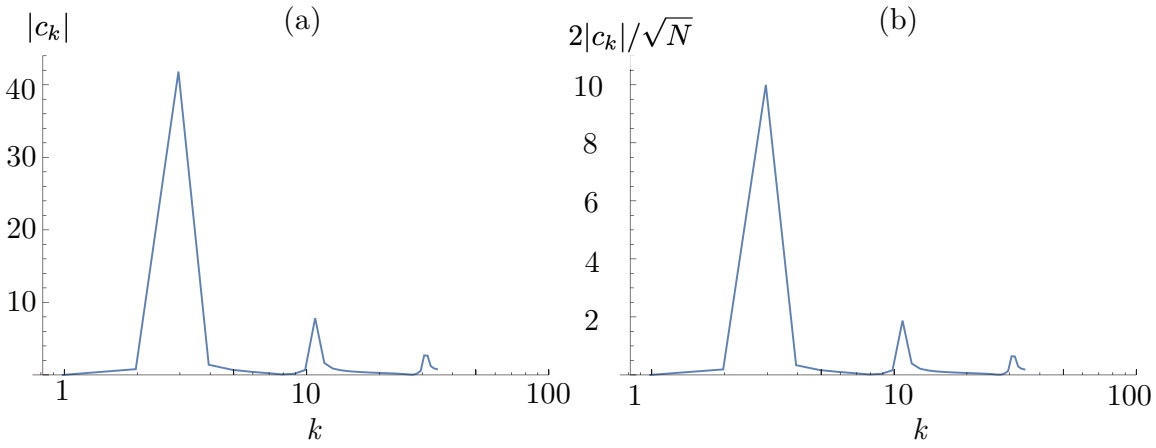

Figure C.3. Plots of the DFT of the signal function given in Eq. C.6. DFT of a discrete set of $N = 70$ points from Eq. (C.6). In (a), the y-axis is given as the magnitudes of each $|c_k|$, and do not match directly with the known magnitudes from the function. In (b), the magnitudes have been scaled by $2/\sqrt{N}$, and now match the corresponding magnitudes of the dominant wavenumbers given in Eq. (C.6).

BIBLIOGRAPHY

1. A. C. Aldo and B. M. Argrow, Dense gas flow in minimum length nozzles, *Journal of Fluids Engineering*, 117(2): 270-276, 1995.

2. J. D. Anderson, Jr., *Modern Compressible Flow with Historical Perspective*, McGraw-Hill, New York, 1982.

3. J. D. Anderson, The governing equations of fluid dynamics: their derivation, a discussion of their physical meaning, and a presentation of the forms particularly suitable for CFD, *Computational Fluids Dynamics: The Basics With Applications*, 37-92, McGraw-Hill, New York, 1995.

4. B. M. Argrow, Computational analysis of dense gas shock tube flow, *Shock Waves*, 6(4): 241-248, 1996.

5. S. A. Arrhenius, Über die Reaktiongeschwindigkeit bei der Inversion von Rohzucker durch Säuren, *Zeitschrift für Physikalische Chemie*, 4:226-248, 1889.

6. J. W. Bates and D. C. Montgomery, Some numerical studies of exotic shock wave behavior, *Physics of Fluids*, 18(28): 462-475, 1999.

7. J. B. Bdzil and D. S. Stewart, The dynamics of detonation in explosive systems, *Annual Review of Fluid Mechanics*, Vol. 39: 263-292, 2007.

8. R. Becker, Stoßwelle und detonation, *Zeitschrift für Physik,* 8: 321-362, 1922.

9. T. L. Bergman and A. S. Lavine, *Fundamentals of Heat and Mass Transfer*, 8th edition, Wiley, Hoboken, 2017.

10. M. Berthelot and P. Veille, Sur la vitesse de propagation des phénomènes explosifs dans les gaz, *Comptes Rendus Hebdomadaires des Séances de l'Académie des Sciences*, 93:18-21, 1881.

11. M. Berthelot and P. Veille, Sur l'onde explosive, *Comptes Rendus Hebdomadaires des Séances de l'Académie des Sciences*, 94:149-152, 1882.

12. H.A. Bethe, The theory of shock waves for an arbitrary equation of state, Technical Report No. 545, Office of Scientific Research and Development, 1942.

13. A. Bourlioux, A. J. Majda, and V. Roytburd, Theoretical and numerical structure for unstable one-dimensional detonations, *SIAM Journal on Applied Mathematics*, 51(2): 303-343, 1991.

14. R. B. Bird, W. E. Stewart, E. N. Lightfoot, *Transport Phenomena*, revised second ed., Wiley, New York, 2007.

15. A. A. Borisov, Al. A. Borisov, S. S. Kutateladze, and V. E. Nakaryakov, Rarefaction shock waves near the critical liquid-vapour point, *Journal of Fluid Mechanics*, 126: 59-73, 1983.

16. J. Borwein and A. S. Lewis, *Convex Analysis and Nonlinear Optimization*, Springer, New York, 2000.

17. B. P. Brown and B. M. Argrow, Two-dimensional shock tube flow for dense gases, *Journal of Fluid Mechanics*, 349: 95-115, 1997.

18. B. P. Brown and B. M. Argrow, Nonclassical dense gas flows for simple geometries, *AIAA Journal*, 36(10): 1824-1847, 1998.

19. B. P. Brown and B. M. Argrow, Application of Bethe-Zel'dovich-Thompson fluids in organic Rankine cycle engines, *Journal of Propulsion and Power*, 16(6): 1118 - 1124, 2000.

20. D. L. Chapman, On the rate of explosion in gases, *Philosophical Magazine*, 47: 90-104, 1899.

21. W. R. Chapman and R. V. Wheeler, The propagation of flame in mixtures of methane and air, Part V, the movement of the medium in which the flame travels, *Journal of the Chemical Society*, 2139: 38-46, 1926.

22. P. Cinnella and P. M. Congedo, Numerical solver for dense gas flows, *AIAA Journal*, 43(11): 2458-2461, 2005.

23. P. Cinnella and P. M. Congedo, Aerodynamic performance of transonic Bethe-Zel'dovich-Thompson flows past an airfoil, *AIAA Journal*, 43(2): 370-378, 2005.

24. P. Cinnella and P. M. Congedo, Optimal airfoil shapes for viscous transonic flows of Bethe-Zel'dovich-Thompson fluids, *Computers and Fluids*, 37(3): 250 - 264, 2008.

25. P. Colonna and A. Guardone, Molecular interpretation of nonclassical gas dynamics of dense vapors under the van der Waals model, *Physics of Fluids*, 18(5): 056101, 2006.

26. P. Colonna and A. Guardone, Siloxanes: A new class of candidate Bethe-Zel'dovich-Thompson fluids, *Physics of Fluids*, 19(8): 086102, 2007.

27. P. Colonna and S. Rebay, Numerical simulation of dense gas flows on unstructured grids with an implicit high resolution upwind Euler solver, *International Journal of Numerical Methods, Fluids*, 46(7): 735, 2004.

28. P. Colonna and P. Silva, Dense gas thermodynamic properties of single and multicomponent fluids for fluid dynamics simulations, *Journal of Fluids Engineering*, 125(3): 414-427, 2003.

29. P. M. Congedo, C. Corre, and P. Cinnella, Airfoil shape optimization for transonic flows of Bethe-Zel'dovich-Thompson fluids, *AIAA Journal*, 45(6): 1303-1316, 2007.

30. R. Courant and K. O. Friedrichs, *Supersonic Flow and Shock Waves*, Interscience Publishers, New York, 1948.

31. M.S. Cramer, Negative nonlinearity in selected fluorocarbons, *Physics of Fluids*, 1(11): 1894-1897, 1989.

32. M. S. Cramer, Shock splitting in single-phase gases, *Journal of Fluid Mechanics*, 199: 281-296, 1989.

33. M. S. Cramer and A. Cluwick, On the propagation of waves exhibiting both positive and negative nonlinearity, *Journal of Fluid Mechanics*, 142: 9-37, 1984.

34. M. S. Cramer and A. B. Crikenberger, The dissipative structure of shock waves in dense gases, *Journal of Fluid Mechanics*, 223: 325-355, 1991.

35. M. S. Cramer and R. Sen, Shock formation in fluids having embedded regions of negative nonlinearity, *Physics of Fluids*, 29(7): 2181-2191, 1986.

36. M. S. Cramer and G. M. Tarkenton, Transonic flows of Bethe-Zel'dovich-Thompson fluids, *Journal of Fluid Mechanics*, 240: 197-228, 1992.

37. Y. Daimon and A. Matsuo, Detailed features of one-dimensional detonations, *Physics of Fluids*, 15(1): 112-122, 2003.

38. W. C. Davis, The detonation of explosives, *Scientific American*, 256(5): 106-113, 1987.

39. C. M. Dafermos, *Hyperbolic Conservation Laws in Continuum Physics*, 3rd edition, Springer, New York, 2010.

40. W. Döring, Über den detonationsvorgang in gasen, *Annalen der Physik*, 435(6-7): 421-436, 1943.

41. P. Duhem, Sur la propagation des ondes de choc au sein des fluides, *Zeitschrift für physikalische chemie*, 69(1): 169 - 186, 1909.

42. G. Dumazer, C. Antoine, A. Lemarchand, and B. Nowakowski, Steady dynamics of exothermic chemical wave fronts in van der Waals fluids, *Physical Review E*, 80(6): 066309, 2009.

43. P. J. Dunlop, Viscosities of a series of gaseous fluorocarbons at 25°C, *Journal of Chemical Physics*, 100(4): 3149 - 3151, 1994.

44. G. Emanuel, *Analytical Fluid Dynamics*, Third ed., CRC Press, Boca Raton, 2015.

45. G. Emanuel, Assessment of the Martin-Hou equation for modeling a nonclassical fluid, *Journal of Fluids Engineering*, 116(4): 883-884, 1994.

46. J. J. Erpenbeck, Stability of steady-state equilibrium detonations, *Physics of Fluids*, 5(5): 604-614, 1962.

47. J. J. Erpenbeck, Stability of idealized one-reaction detonations, *Physics of Fluids*, 7(5): 684-696, 1964.

48. S. H. Fergason and B. M. Argrow, Navier-Stokes analysis of dense gas shock tube flow fields, International Workshop on Dense Gas Dynamics, August 1999.

49. S. H. Fergason and B. M. Argrow, Simulations of nonclassical dense gas dynamics, AIAA-2001-2752, 35th AIAA Thermophysics Conference, Anaheim, CA, June 2001.

50. S. H. Fergason, A. Guardone, B.M. Argrow, Construction and validation of a dense gas shock tube, *Journal of Thermophysics and Heat Transfer*, 17:326-330, 2003.

51. S. H. Fergason, T. L. Ho, B. M. Argrow, G. Emanuel, Theory for producing a single-phase rarefaction shock wave in a shock tube, *Journal of Fluid Mechanics*, 445: 37-54, 2001.

52. W. Fickett and W. C. Davis, *Detonation Theory and Experiment*, University of California Press, Berkeley, CA, 1979.

53. W. Fickett and W. W. Wood, Flow calculations for pulsating one-dimensional detonations, *Physics of Fluids*, 9(5): 903-916, 1966.

54. K. O. Friedrichs, On the mathematical theory of deflagrations and detonations, Technical Report 76-46, NAVORD, 1946.

55. I. Gasser and P. Szmolyan, A geometric singular perturbation analysis of detonation and deflagration waves, *SIAM Journal of Mathematical Analysis*, 24(4): 968-986, 1993.

56. U. Ghia, S. Bayyuk, J. Benek, K. Bryden, R. Bush, T. Conlisk, S. Habchi, A. Hadid, R. Harris, C. Hirsch, M. Jurkovich, H. Lee, E. Lynch, M. Mani, U. Mehta, W. Oberkampf, F. Palacios, D. Pelletier, J. Powers, C. Roy, C. Rumsey, T. Shih, J. Schaefer, and C. Steffen, Recommended practice for code verification in computational fluid dynamics, AIAA R-141-2021, 2021.

57. D. Gilbarg and D. Paolucci, The structure of shock waves in the continuum theory of fluids, *Journal of Rational Mechanics and Analysis*, 2(5): 617-642, 1953.

58. A. Guardone, Three-dimensional shock tube flows for dense gases, *Journal of Fluid Mechanics*, 583: 423-442, 2007.

59. A. Guardone and B. M. Argrow, Nonclassical gasdynamic region of selected fluorocarbons, *Physics of Fluids*, 17(11): 116102, 2005.

60. A. Guardone, L. Vigevano, and B. M. Argrow, Assessment of thermodynamic models for dense gas dynamics, *Physics of Fluids*, 16(11): 3878-3887, 2004.

61. A. Guardone, C. Zamfirescu, and P. Colonna, Maximum intensity of rarefaction shock waves for dense gases, *Journal of Fluid Mechanics*, 642: 127-146, 2007.

62. M. Hanana, M. H. Lefebvre, and P. J. V. Tiggelen, Pressure profiles in detonation cells with rectangular and diagonal structures, *Shock Waves*, 11(2): 77-88, 2001.

63. J. Harinck, A. Guardone, and P. Colonna, The influence of molecular complexity on expanding flows of ideal and dense gases, *Physics of Fluids*, 21(8): 086101, 2009.

64. L. He and J. H. S. Lee, The dynamical limit of one-dimensional detonations, *Physics of Fluids*, 7(5): 1151-1158, 1995.

65. A. K. Henrick, T. D. Aslam, and J. M. Powers, Mapped weighted essentially non-oscillatory schemes: achieving optimal order near critical points, *Journal of Computational Physics*, 207(2): 542-567, 2005.

66. A. K. Henrick, T. D. Aslam, and J. M. Powers, Simulations of pulsating one-dimensional detonations with true fifth order accuracy, *Journal of Computational Physics*, 213(1): 311-329, 2006.

67. V. Hermes, I. Klioutchnikov, and H. Olivier, Linear stability of WENO schemes coupled with explicit Runge-Kutta schemes, *International Journal for Numerical Methods in Fluids*, 69(6): 1065-1095, 2012.

68. J. O. Hirschfelder and C. F. Curtiss, Theory of detonations, I, irreversible unimolecular reaction, *Journal of Chemical Physics*, 28(6): 1130-1147, 1958.

69. P. H. Hugoniot, Memoire sur la propagation des mouvements dans les corps et spécialement dans les gaz parfaits, *Journal de l'École Polytechnique*, 58: 1-125, 1889.

70. J. Ianelli, An exact non-linear Navier-Stokes compressible-flow solution for CFD code verification, *International Journal for Numerical Methods in Fluids*, 72(2): 157-176, 2012.

71. G. S. Jiang and C. W. Shu, Efficient implementation of weighted ENO schemes, *Journal of Computational Physics*, 126(1): 202-228, 1996.

72. E. Jouguet, Sur la propagation des réactions chimiques dans les gaz, *Journal de Mathématiques Pures et Appliquées*, 1: 347-425, 1905.

73. G. D. Kahl and D. C. Mylin, Rarefaction shock possibility in a van der Waals-Maxwell fluid, *Physics of Fluids*, 12(11): 2283-2291, 1969.

74. A. R. Kasimov and D. S. Stewart, On the dynamics of self-sustained one-dimensional detonations: A numerical study in the shock-attached frame, *Physics of Fluids*, 16(10): 3566, 2004.

75. A. Kluwick and G. Meyer, Shock regularization in dense gases by viscous-inviscid interactions, *Journal of Fluid Mechanics*, 644: 473-507, 2010.

76. H. I. Lee and D. S. Stewart, Calculation of linear detonation instability: one-dimensional instability of planar detonations, *Journal of Fluid Mechanics*, 216: 103-132, 1990.

77. J. H. S. Lee, *The Detonation Phenomenon*, Cambridge University Press, Cambridge, UK, 2008.

78. H. F. Lehr, Experiments on shock-induced combustion, *Astronautica Acta*, 17(4-5): 589-597, 1972.

79. K. Lambrakis and P. A. Thompson, Existence of real fluids with a negative fundamental derivative Γ, *Physics of Fluids*, 15(3): 933-935, 1972.

80. R. J. LeVeque, *Numerical Methods for Conservation Laws*, 2nd edition, Birkhäuser, Basel, 1992.

81. H. W. Liepmann and A. Roshko, *Elements of Gasdynamics*, Dover, Mineola, 2001.

82. E. Mallard and H. Le Chantelier, Sur les vitesses de propagation de l'inflammation dans les mélanges gazeux explosifs, *Comptes Rendus Hebdomadaires des Séances de l'Académie des Sciences*, 93: 145-148, 1881.

83. R. Menikoff and B. J. Plohr, The Riemann problem for fluid flow of real materials, *Review of Modern Physics*, 61(1): 75-130, 1989.

84. V. Michelson, The normal velocity of ignition of combustible gaseous mixtures, *Transactions of Moscow University*, 10: 1-92, 1893.

85. M. Morduchow and P. A. Libby, On a complete solution of the one-dimensional flow equations of a viscous, heat conducting, compressible gas, *Journal of the Aeronautical Sciences*, 16(11): 674-684, 1949.

86. M. Motamed, C. B. Macdonald, and S. J. Ruuth, On the linear stability of the fifth-order WENO discretization, *Journal of Scientific Computing*, 47(2): 127-149, 2011.

87. R. S. Myong, Analytical solutions of shock structure thickness and asymmetry in Navier-Stokes/Fourier framework, *AIAA Journal*, 52(5): 1075-1080, 2014.

88. H. D. Ng, A. J. Higgins, C. B. Kiyanda, M. I. Radulescu, J. H. S. Lee, K. R. Bates, and N. Nikiforakis, Nonlinear dynamics and chaos analysis of one-dimensional pulsating detonations. *Combustion Theory and Modeling*, 9(1): 159-170, 2005.

89. W. L. Oberkampf and C. J. Roy, *Verification and Validation in Scientific Computing*, Cambridge University Press, Cambridge, 2010.

90. A. K. Oppenheim, R. A. Stern, and P. A. Urtiew, On the development of detonation with pre-ignition, *Combustion and Flame*, 4(4): 335-341, 1960.

91. A. K. Oppenheim, N. Manson, and H. G. Wagner, Recent progress in detonation research, *AIAA Journal*, 1(10): 2243-2252, 1963.

92. K. R. Pielemeier, A. M. Davies, J. M. Powers, Solution verification of anomalous waves in non-ideal gases, in review, 2023.

93. K. R. Pielemeier and J. M. Powers, Steady detonation dynamics in a van der Waals gas, in preparation, 2023.

94. K. R. Pielemeier and J. M. Powers, Unsteady detonation dynamics in a van der Waals gas, in preparation, 2023.

95. J. M. Powers, *Combustion Thermodynamics and Dynamics*, Cambridge University Press, New York, 2016.

96. J. M. Powers, *Mechanics of Fluids*, Cambridge University Press, Cambridge, UK, 2024.

97. J. M. Powers and T. D. Aslam, Exact solutions for multidimensional compressible reactive flow for verifying numerical algorithms, *AIAA Journal*, 44(2): 337 - 344, 2006.

98. J. M. Powers and M. Sen, *Mathematical Methods in Engineering*, Cambridge University Press, New York, 2015.

99. J. M. Powers and S. Paolucci, Accurate spatial resolution estimates for reactive supersonic flow with detailed chemistry, *AIAA Journal*, 43(5): 1088-1099, 2005.

100. L. Quartapelle, L. Castelletti, A. Guardone, and G. Quaranta, Solution of the Riemann problem of classical gasdynamics, *Journal of Computational Physics*, 190(1): 118-140, 2003.

101. M. I. Radulescu, G. J. Sharpe, C. K. Law, and J. H. S. Lee, The hydrodynamic structure of unstable cellular detonations, *Journal of Fluid Mechanics*, 580: 31-81, 2007.

102. V. Raman, S. Prakash, and M. Gamba, Nonidealities in rotating detonation engines, *Annual Review of Fluid Mechanics*, 55: 639-674, 2023.

103. W. J. M. Rankine, On the thermodynamic theory of waves of finite longitudinal disturbance, *Philosophical Transactions of the Royal Society of London*, 160: 277-288, 1870.

104. W. J. Rider and J. W. Bates, A high-resolution Godunov method for modeling anomalous fluid behavior, *Godunov Methods: Theory and Applications*, edited by E. F. Toro, 717 - 723, Kluwer Academic, New York, 2001.

105. C. M. Romick, T. D. Aslam, J. M. Powers, The effect of diffusion on the dynamics of unsteady detonations, *Journal of Fluid Mechanics*, 699: 453-464, 2012.

106. C. M. Romick, T. D. Aslam, J. M. Powers, Verified and validated calculation of unsteady dynamics of viscous hydrogen-air detonations, *Journal of Fluid Mechanics*, 769: 154-181, 2015.

107. R. G. Schmitt and P. B. Butler, Detonation properties of gases at elevated initial pressures, *Combustion Science and Technology*, 106(1-3): 157-191, 1995.

108. I. R. Seitenzahl, C. A. Meakin, D. M. Townsley, D. Q. Lamb, and J. W. Truran, Spontaneous initiation of detonations in white dwarf environments: Determination of critical sizes, *The Astrophysical Journal*, 696(1): 515-527, 2009.

109. G. J. Sharpe and S. A. E. G. Falle, Numerical simulations of pulsating detonations: I, nonlinear stability of steady detonations, *Combustion Theory and Modeling*, 4(4): 557-574, 2000.

110. M. Short and J. J. Quirk, High explosive detonation-confiner interactions, *Annual Review of Fluid Mechanics*, 50: 215-242, 2018.

111. C. W. Shu and S. Osher, Efficient implementation of essentially non-oscilliatory shock-capturing schemes, *Journal of Computational Physics*, 77(2): 439-471, 1988.

112. C. W. Shu and S. Osher, Efficient implementation of essentially non-oscilliatory shock-capturing schemes II, *Journal of Computational Physics*, 83(1): 32-78, 1989.

113. W. A. Sirignano, Normal shocks with high upstream pressure, *Physical Review Fluids*, 3(9): 093401, 2018.

114. G. A. Sod, A survey of several finite difference methods for systems of nonlinear hyperbolic conservation laws, *Journal of Computational Physics*, 27(1): 1- 31, 1978.

115. J. L. Steger and R. F. Warming, Flux vector splitting and the inviscid gasdynamics equations with applications to finite-difference methods, *Journal of Computational Physics*, 40(2): 263-293.

116. R. A. Strehlow, Gas phase detonations: recent developments, *Combustion and Flame*, 12(2): 81-101, 1968.

117. G. I. Taylor, The conditions necessary for discontinuous motion in gases, *Proceedings of the Royal Society of London, Series A*, 84(571): 371-377, 1910.

118. B. Texier and K. Zumbrun, Transition to longitudinal instability of detonation waves is generally associated with Hopf bifurcation to time-periodic galloping solutions, *Communications in Mathematical Physics*, 302(1): 1-51, 2011.

119. P.A. Thompson, A fundamental derivative in gasdynamics, *Physics of Fluids*, 14(9): 1843-1849, 1971.

120. R. von Mises, On the thickness of a steady shock wave, *Journal of the Aeronautical Sciences*, 17(9): 551-554, 1950.

121. R. von Mises, *Mathematical Theory of Compressible Fluid Flow*, Academic Press, New York, 1958.

122. J. von Neumann, Theory of detonation waves. Progress Report to the National Defense Research Committee Div. B, OSRD-549 (April 1, 1942. PB 31090), in *John von Neumann: Collected Works*, edited by A. H. Taub, Vol. 6, Pergamon, New York, 1963.

123. J. C. H. Wang and J. P. Hickey, Analytical solutions to shock and expansion waves for non-ideal equations of state, *Physics of Fluids*, 32(8): 086105, 2020.

124. S. D. Watt and G. J. Sharpe, Linear and nonlinear dynamics of cylindrically and spherically expanding detonation waves, *Journal of Fluid Mechanics*, 522: 329-356, 2005.

125. Wolfram Research, Inc., *Mathematica*, Version 13.2, Champaign, IL, 2022.

126. C. Zamfirescu, A. Guardone, and P. Colonna, Admissibility region for rarefaction shock waves in dense gases, *Journal of Fluid Mechanics*, 559: 363-381, 2008.

127. Y. B. Zel'dovich, On the possibility of rarefaction shock waves, *Zhurnal Eksperimental'noi i Teoreticheskoi Fiziki*, 16(4): 363-364, 1946 (English translation: Joint Publications Research Service 7320, Arlington, VA., 1960).

128. Y. B. Zel'dovich, On the theory of the propagation of detonation in gaseous systems, *Zhumal Eksperimental'noi i Teoreticheskoi Fiziki*, 10: 542-568, 1940 (English translation: NACA TM 1261, 1960).

129. Y. B. Zel'dovich and Y. P. Raizer, *Physics of Shock Waves and High Temperature Hydrodynamic Phenomena*, edited by W. D. Hayes and R. F. Probstein, Academic Press, New York, 1966.

This document was prepared & typeset with pdfLaTeX*, and formatted with* NDdiss2$_\varepsilon$ *classfile (v3.2017.2[2017/05/09])*